DOKUZ EYLÜL UNIVERSITY
GRADUATE SCHOOL OF NATURAL AND APPLIED SCIENCES

IMPACT LOADING IN LAMINATED COMPOSITES

by
Emre ERBİL

August, 2008
İZMİR

IMPACT LOADING IN LAMINATED COMPOSITES

A Thesis Submitted to the
Graduate School of Natural and Applied Sciences of Dokuz Eylül University
In Partial Fulfillment of the Requirements for the Degrees of Master of Science
in Mechanical Engineering, Mechanical Program

by
Emre ERBİL

August, 2008
İZMİR

M.Sc THESIS EXAMINATION RESULT FORM

We have read the thesis entitled **"IMPACT LOADING IN LAMINATED COMPOSITES"** completed by **EMRE ERBİL** under supervision of **Prof. Dr. RAMAZAN KARAKUZU** and we certify that in our opinion it is fully adequate, in scope and in quality, as a thesis for the degree of Master of Science.

....
Prof. Dr. RAMAZAN KARAKUZU

Supervisor

....

(Jury Member) (Jury Member)

Prof. Dr. Cahit HELVACI
Director
Graduate School of Natural and Applied Sciences

ACKNOWLEDGEMENTS

I would like to offer my thanks and my gratitude to my supervisor, Prof. Dr. Ramazan KARAKUZU, for his excellent guidance, tolerant approach and continuous encouragement throughout the preparation of this study.

I want to express my thanks to Dr. Mehmet AKTAŞ for his great help during my study.

And thanks to the Izoreel Firm and Mr. Rahmi AKIN for their help during production of the composite materials used.

I also would like to thank to my friend Abdullah Kâzım ÖZCAN for his moral support.

Finally, I am deeply indebted to my family members for their patience, support and their tenderness.

Emre ERBİL

IMPACT LOADING IN LAMINATED COMPOSITES

ABSTRACT

The aim of this study is to examine the damage and deformation (prediction, initiation and propagation), to criticize -when and which conditions they can occur- with experimental results and to compare them with finite elements results, and then comment on them. The specimens that used during the experiments are produced at Izoreel Company, and they examined in Fractovis Plus impact tester machine with the different initial impact energy levels, initial velocities, and initial impactor mass. The matrix material of the specimen is made of with the mixture of CY225 Epoxy with HY225 hardener resin. And the unidirectional e-glass fabric having weight of 509 g/m^2 was used as reinforcing material. Specimen geometry is square with 100 mm of per edge. The sequence is in $[0/30/60/90]_s$ form. A ForTran-based 3D impact finite element code had chosen to solve both $[0/30/60/90]_s$ and other fiber orientations.

The specimens tested in ternate groups. It is aimed here to examine the effects of velocity, mass and impact energy. And also, it is examined if the threshold value of the contact force that delamination occur, and if this value could be predicted with the finite element code or not. The delamination areas and the delamination ratios are computed with a pixel-based image processing code, precisely. At last, the composite laminates -that had not been experimented like the twice and third as the laminate thickness- have solved with 3D impact code, and the results have discussed.

The last addition to the impact experiments is about the fiber orientations. The non-experimented specimens as [0/l5/-15/90]s, [0/30/-30/90]s, [0/60/-60/90]s, [0/75/-75/90]s had solved with finite element code, too.

Keywords: low velocity impact, laminated composite materials, delamination

TABAKALI KOMPOZİTLERDE DARBELİ YÜKLEME

ÖZ

Bu çalışmanın amacı, tabakalı kompozitlerde darbe hasarının incelenmesi (öngörme, başlangıç ya da yayılma), ne zaman ve hangi şartlarda ortaya çıktığının deney sonuçlarıyla gözlenmesi ve bu sonuçların sonlu elemanlar çözümleriyle kıyaslanıp, yorumlanmasıdır. Deney esnasında kullanılan numuneler Izoreel Şirketi'nde üretilmiş olup, Fractovis deney cihazında çeşitli enerji, hız ve kütlelerde hasarlı muayeneye tabi tutulmuştur. Numunenin matriksi CY225 Epoxy maddesine HY225 sertleştirici reçine karıştırılarak elde edilmiştir. Yine numunede, ağırlığı 509 gr/m^2 olan tek yönlü E-glass cam elyafı kullanılmıştır. Numuneler karedir ve her bir kenarı 100 mm'dir. Cam elyafların diziliş sırası $[0/30/60/90]_s$ şeklindedir. Sonlu elemanlar yazılımı olarak ForTran tabanlı 3 boyutlu darbe için tasarlanmış sonlu elemanlar kodu tercih edilmiştir.

Deney numuneleri üçerli öbekler halinde muayeneye tabi tutulmuştur. Burada amaçlanan; hız, kütle ve enerji etkisini incelemektir. Delaminasyon olayının başladığı temas kuvveti eşik değeri incelenmiş, bu değerin darbe yazılımı ile öngörülüp öngörülemeyeceği araştırılmıştır. Deney sonucunda hasara uğrayan numuneler, bilgisayar ortamında nokta tabanlı resim işleme kodu ile süzülerek delaminasyon miktarları ve yüzdeleri yüksek hassasiyetle saptanmıştır. Ayrıca, deneylerde bulunmayan, numune kalınlığının iki ve üç katı kalınlıklarda malzemenin nasıl bir tutum sergileyeceği araştırılmış ve yorumlanmıştır.

Bir diğer ilâve ise açılar konusunda yapılmıştır. Deneyleri yapılmayan [0/l5/-15/90]s, [0/30/-30/90]s, [0/60/-60/90]s, [0/75/-75/90]s fiber açılarında da yazılım sonuçları açıklanmıştır.

Anahtar Sözcükler: düşük hızlı darbe, tabakalı kompozit malzemeler, ayrılma

CONTENTS

CHAPTER ONE

INTRODUCTION

Many industries have adopted a virtual design methodology where the majority of design and development is achieved using computer simulations; verification testing being conducted only at the end of the design process. This substantially reduces the design cost by decreasing the need for expensive full scale physical tests.

In service aircraft loads commonly include impact events such as a dropped tool or debris from runways. This may result in a large internal damaged area of the laminate that is not detectable from visible observation. Fluctuating in-service loads, in particular compression, can continuously grow the damage area, possibly resulting in complete structural collapse of the damaged part. The development of the current analytical methods resulting in a viable virtual design capability will significantly reduce the cost and speed up development of damage tolerant composite structures in industry. Both damage mechanics and fracture mechanics methods have been employed in the literature to predict the debilitating effects of inter-ply delamination due to low velocity impacts composite laminates.

Material damage is associated with a stress or strain regime, while fracture is the fragmentation of material by cracking and is determined by energy considerations. Fracture will occur if the growth of a crack results in a lower energy state of the system. That is to say the energy required to overcome the cohesive force of the atoms is equal to the dissipation of the strain energy that is released by the crack.

In homogenous metals, material damage and fracture are generally considered to be independent of each other. Although the formation of fracture may occur in conjunction with plasticity at the crack tip, the energy associated with this plasticity can be included in the energy equations and is considered a part of the fracture process. This is not true for composites where the discrete components of the composite may experience damage and fracture concurrently. Typically a low speed impact will overstress the matrix material, producing local sub-critical cracking (micro- cracking). This does not necessarily produce fracture; however it will result in load redistribution and the concentration of energy and stress at the inter-ply regions where large differences in material stiffness exist. These conditions are ideal for a fracture based inter-ply delamination to initiate and grow. The onset, and rapid propagation of a crack, results in sudden variations in both section properties and load paths within the composite local to the impactor. This requires an adaptive method to track the progression of damage and fracture growth. (Elder , Thomson, Nguyen, Scott, 2004) In this study, the changes in impact parameters are tracked with DAS (Data Acquisition System) that connected to the impact testing machine.

The first attempts to characterize composite materials under dynamic loading were carried out by Rotem (1971) and Lifshitz (1976) and Sierakowski et al. (1971) Sun and Chattopadhyay (1975), Dobyns (1981), and Ramkumar and Chen (1983) employed the first-order shear deformation theory developed by Whitney and Pagano (1970) and used in conjunction with the Hertzian contact law to study the impact of laminated composite plates. Sankar (1992) presented semi-empirical formulae for predicting impact characteristics such as peak force, contact duration, and peak strain on back surface. By solving a one-parameter differential equation, Olsson (1992) obtained an approximate analytical solution to the first phase of impact, or wave propagation dominated, response of composite plates. Various researchers have developed the three dimensional finite element models to investigate impact. Yang and Sun (1982), Tan and Sun (1985) and Sun and Chen (1985) studied impact on laminates under initial stress using the finite element method with a Newmark time integration algorithm. The merit of this three-dimensional numerical model is that it can provide detailed information about the local stresses and strains, which are key factors to produce initial damage in materials. Thereby, it is possible to capture the formation impact-induced damage, if a very fine mesh is used. The disadvantage of this approach is that its computational demands can be exorbitant as pointed out by Davies and Zhang (1995). Some simple, but efficient theoretical and energy-based approximation methods have also been presented to deal with this problem. Choi et. al. (1991) used the dynamic finite element method coupled with failure analysis to predict the threshold of impact damage and initiation of delamination. Numerous researchers have used instrumented impact test apparatus to study the impact characteristics of different laminated composites. Chang and Sun (1989) determined the dynamic impact forces on a composite laminate by using experimentally generated Green's functions and signal deconvolutions. Jih and Sun (1993) studied experimentally prediction of delamination in composite laminates subjected to low-velocity impact. They found that the results of the drop-weight impact tests indicated that low-velocity impact-induced delamination could be predicted by using the static interlaminar fracture toughness in conjunction with the static linear beam model. (Aslan, Karakuzu, Okutan, 2002)

Zhang, Zhu, & Lai (2004) published an approach to predict the initiation and propagation of damage in composite laminated plates, which is based on contact constraint introduced by penalty function method. The numerical analysis computed with ABAQUS, and its user subroutine VUINTER. Another research is performed by Cesari, Re, Minak & Zucchelli (2006) that deals with the characterization of damage in quasi-isotropic carbon fibre reinforced epoxy resin laminate loaded at the centre. They applied the problem into ANSYS software to predict the first ply failure (FPF) and the ultimate ply failure (UPF) of laminate. The one another investigation of the low velocity impact on laminated composite thin disks of epoxy resin reinforced by carbon fiber is presented by Tita, Carvalho, & Vandepitte (2007). They used the Hill's model and material models implemented by UMAT (User Material Subroutine) into ABAQUS FEA software, in order to simulate the failure mechanisms under indention tests.

Zheng & Binienda (2007) had investigated the small mass impacts on composite structures that are common cases caused by hailstones and runway debris. Small mass impactors usually result in a wave controlled local response, which is independent of boundary conditions. This response occurs before the reflection of waves from the boundaries and cannot be modeled by large mass drop weight tests. An elasto-plastic contact law, which accounts for permanent indentation and damage effects, was used here to study small mass impact on laminated composite plates. By comparing with results from the Hertzian contact law, it was found that damage can change the dynamic response of the structure significantly with increasing impact velocity. Due to smaller contact force generated for the case of using elasto-plastic contact, the central displacement of the plate is also less than the one using Hertzian contact law. The linearized version of the contact law was then used to derive the closed-form approximations of the contact force, indentation and plate central displacement for the impact loading of composite laminates. The threshold velocity for delamination onset under small mass impact was predicted analytically based on the obtained peak contact forces by combining with an existing quasi-static delamination threshold load criterion. A good agreement was found between the predicted threshold values and published experimental results. (Zheng & Binienda, 2007)

A methodology aiming at taking into account delaminated composite structures behaviour has been developed by Coutellier, Walrick, & Geoffroy (2005). Their study falls into two parts. The first one tackles the delamination detection within damaged thin laminated structures. In the finite element method (FEM) computational code, those laminated structures have been modelled using multi-layered shell elements. The methodology uses post-process criteria, based on fracture mechanics linked with damage mechanics, of computational code by the effective stres tensor. In the second place, the influence of delamination over the overall behaviour of the structure is taken into account. This influence is introduced by locally changing material characterization, quite progressively during the loading phase. These integrated effects change the numerical behaviour on loading and energy curves. The validation is carried out with experimental low velocity impact tests on the bending tests. A satisfactory coherence is shown for damage mechanisms and delamination shapes, in different examples. The methodology developed is recognized a predictive process for several laminates under study. It can be used as a potential tool to size laminated structures at design stage. They presented the different aspects of this delamination approach in their journal.

Morozov, Sylantiev, & Evseev (2003) had investigated a study of the damage resistance of laminated composite helicopter blades subjected to impact loading. In their study, dynamic stress intensity factors are determined for composite laminate and separate layers using combined theoretical and experimental approach. The effect of the projectile size on the damage tolerance of composite blade is investigated and tolerable sizes of the defects are estimated in their journal.

In this study, the eight layered composite specimens are tested in experimental and numerical platform. The experimental and numerical results are examined with comparing the similarities and differences between them. Three experiments are performed for each case and the mean values are used, to reach an appropriate result and to avoid exorbitant values in graphs. In numerical solutions, a finite element code named 3DIMPACT is chosen to compute the contact force, deflection, and delaminations that uses the Newmark time integration algorithm in computations. With this code, delaminations are examined by scaling them to fit the experimental dimensions to calculate the difference between numerical and experimental results.

CHAPTER TWO

ESSENTIAL BACKGROUND ON COMPOSITE MATERIALS

2.1 Introduction

In this chapter, giving essential information about composite materials is aimed. The types and characteristics of composite materials, and where are they used. There are several comments that define composite materials. Some of them are:

- "A composite material is a macroscopic combination of two or more distinct materials, having a recognizable interface between them." (Miracle & Donaldson , 2001)
- "Generally speaking any material consisting of two or more components with different properties and distinct boundaries between the components can be referred to as a composite material." (Valery V. & Evgeny V, 2007, p. 9).
- "The word composite in the term composite material signifies that two or more materials are combined on a macroscopic scale to form a useful third material." (Jones, 1999, p. 2)
- "A composite more combined constituents that are combined at a macroscopic level and are not soluble in each other. One constituents is called the *reinforcing phase* and the on e in which it is embedded is called the *matrix*." (Kaw, 2006)
- "Fiber-reinforced composite materials consist of high strength and modulus embedded in or bonded to a matrix with distinct interfaces (boundaries) between them." (Mallick, 2007)

- "Engineered materials which consist of more than one material type. Fiberglass is a familiar example, in which glass fibers are embedded within a polymeric (plastic) material. A composite is designed to display a combination of the best characteristics of each of the component materials. Fiberglass acquires strength from the glass and flexibility from the polymer." (Brazil, 2008)
- "A combination of two or more materials (reinforcing elements, fillers, and composite matrix binder), differing in form or composition on a macro scale. The constituents retain their identities; that is, they do not dissolve or merge completely into one another although they act in concert. Normally, the components can be physically identified and exhibit an interface between one another." (Fiberglass Warehouse, 2008)
- "Composite materials (or composites for short) are engineered materials made from two or more constituent materials with significantly different physical or chemical properties and which remain separate and distinct on a macroscopic level within the finished structure." (Wikipedia, 2008)
- "Strong lightweight material developed in the laboratory; fibers of more than one kind are bonded together chemically." (WordNet® 3.0, 2008)

Traditional engineering materials (steel, aluminum, etc.) contain impurities that can represent different phases of the same material and fit the broad definition of a composite, but are not considered composites because the elastic modulus or strength of the impurity phase is nearly identical to that of the pure material. The definition of a composite material is flexible and can be augmented to fit specific requirements. In this text a composite material is considered to be one that contains two or more distinct constituents with significantly different macroscopic behavior and a distinct interface between each constituent (on the microscopic level). This includes the continuous fiber laminated composites of primary concern herein, as well as a variety of composites not specifically addressed.

2.2 Classification of Composite Materials

There are four types of composite materials; polymer (PMC), metal (MMC), ceramic (CMC), and carbon (CAMC) matrix composites. The carbon-carbon matrix composite (CCC) is the most important type of CAMCs. The matrix and fiber materials that can be mixed to compose composite material have shown in Table 2.1.

Table 2.1 Types of composite materials. (Harper, 2004)

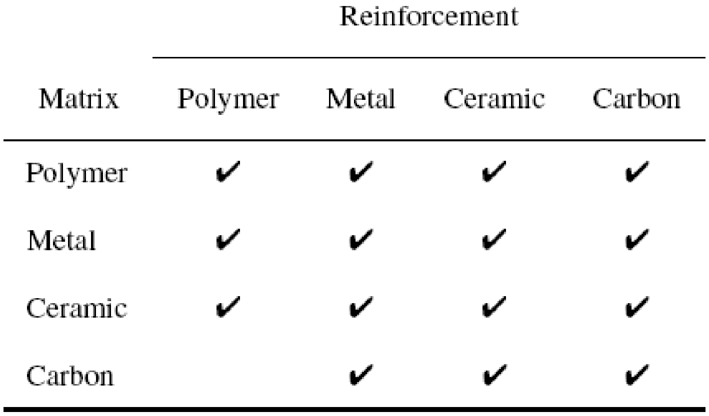

	Reinforcement			
Matrix	Polymer	Metal	Ceramic	Carbon
Polymer	✓	✓	✓	✓
Metal	✓	✓	✓	✓
Ceramic	✓	✓	✓	✓
Carbon		✓	✓	✓

Polymer matrix composites (PCM) include thermoset (epoxy, polyimide, polyester) or thermoplastic (poly-ether-ether-ketone, polysulfone) resins reinforced with glass, carbon (graphite), aramid (Kevlar), or boron fibers. They are used primarily in relatively low temperature applications.

Metal matrix composites (MMC) consist of metals or alloys (aluminum, magnesium, titanium, copper) reinforced with boron, carbon (graphite), or ceramic fibers. Their maximum use temperature is limited by the softening or melting temperature of the metal matrix. The principal motivation was to dramatically extend the structural efficiency of metallic materials while retaining their advantages, including high chemical inertness, high shear strength, and good property retention at high temperatures.

Ceramic matrix composites (CMC) consist of ceramic matrices (silicon carbide, aluminum oxide, glass-ceramic, silicon nitride) reinforced with ceramic fibers. They are best suited for very high temperature applications. Ceramic-matrix composite development has continued to focus on achieving useful structural and environmental properties at the highest operating temperatures.

Carbon/carbon composites (CCC) consist of carbon or graphite matrix reinforced with graphite yarn or fabric. They have unique properties of relatively high strength at high temperatures coupled with low thermal expansion and low density. (Daniel & Ishai, 1994).

In another way, composite materials can be regrouped according to their appearance rather than their matrix. They are:

- Fibrious composites: Obtained by putting long fiber groups or whiskers into a matrix with a predefined angle (Figure 2.1) or in random order, and curing at a specified temperature. The fibers can be straight or woven, and they can be continuous or discontinuous (Figure 2.2).

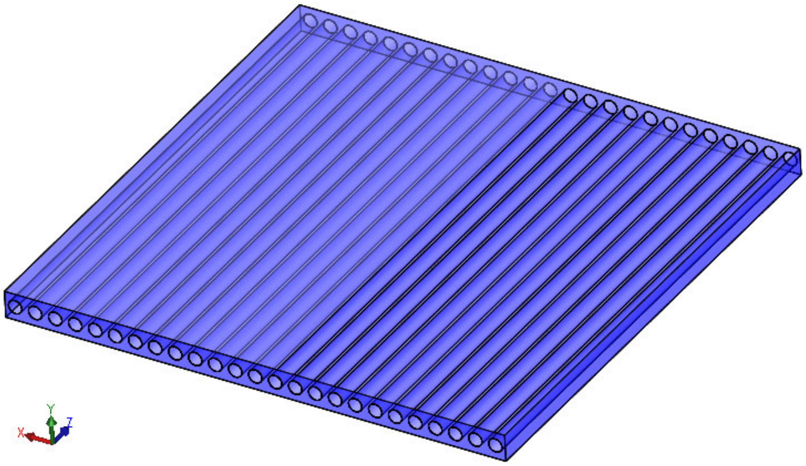

Figure 2.1 A lamina with longitudinal fibers.

There is a difference between fibers and whiskers. Fiber is characterized geometrically not only by its very high length-to-diameter ratio but by its near-crystal-sized diameter. A whisker has essentially the same near-crystal-sized diameter as a fiber, but generally is very short and stubby, although the length-to-diameter ratio can be in the hundreds. Thus, a whisker is an even more obvious example of the crystal-bulk-material-property-difference paradox. That is, a whisker is even more perfect than a fiber and therefore exhibits even higher properties. Whiskers are obtained by crystallization on a very small scale resulting in a nearly perfect alignment of crystals. Materials such as iron have crystalline structures with a theoretical strength of 2900000 psi (20 GPa), yet commercially available structural steels, which are mainly iron, have strengths ranging from 75000 psi to about 100000 psi (570 to 690 MPa). (Jones, 1999)

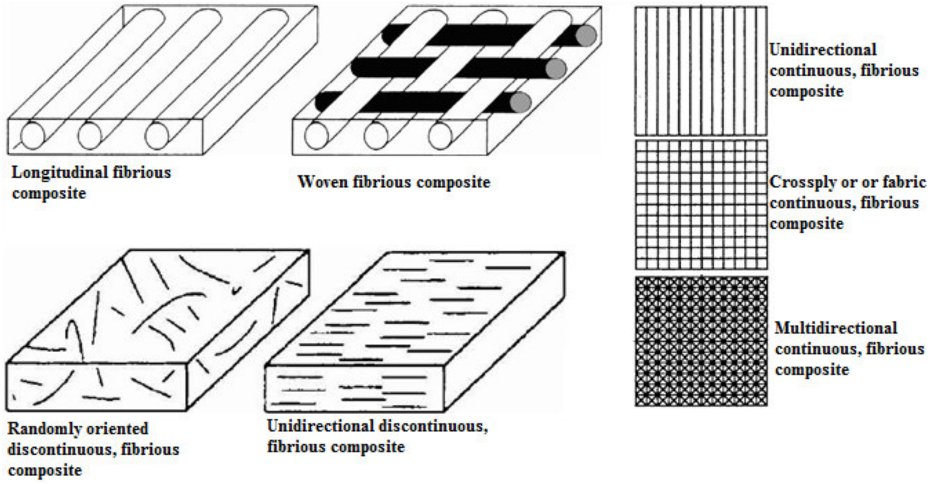

Figure 2.2 Types of fibrious composites.

- ➢ Laminated composites: Two or more composite layers are bonded together. (Figure 2.3) Lamination achieves the mechanical properties in composite. Mechanical properties can be changed with the angle of fibers in laminate.

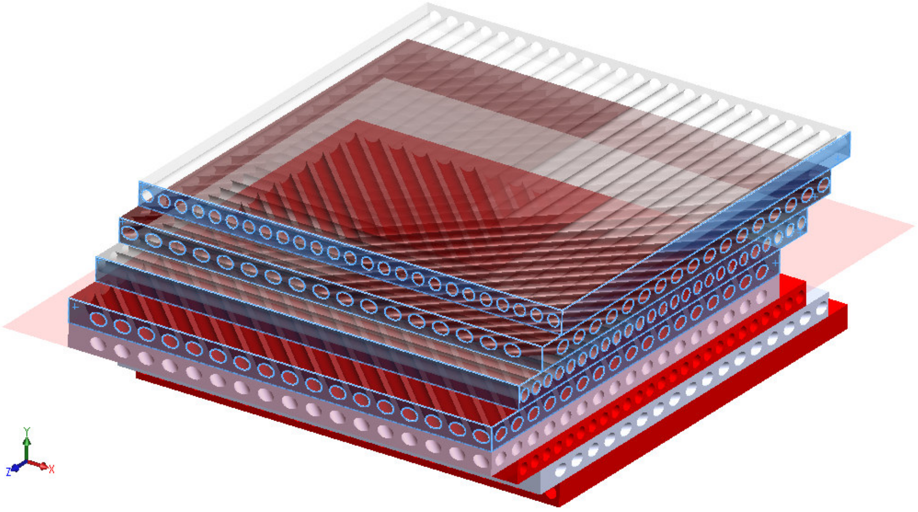

Figure 2.3 A laminated composite with the fiber angle of $[90/+45/0/-45]_s$.

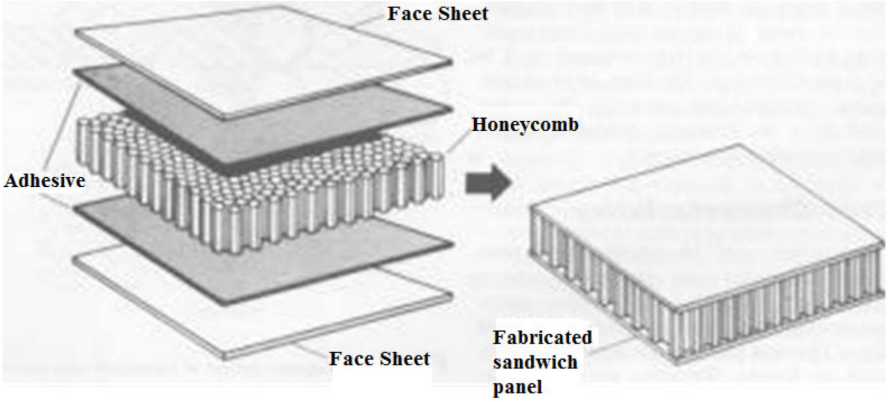

Figure 2.4 Honeycomb sandwich construction. (www.mdacomposites.org, 2008)

Laminated composites can be in the sandwich structural form. Structural sandwich is a layered composite formed by bonding two thin facings to a thick core (Figure 2.4). It is a type of stressed-skin construction in which the facings resist nearly all of the applied edgewise (in-plane) loads and flat wise bending moments. The thin spaced facings provide nearly all of the bending rigidity to the construction. The core spaces the facings and transmits shear between them so that they are effective about a common neutral axis. The core also provides most of the shear rigidity of the sandwich construction. By proper choice of materials for facings and core, constructions with high ratios of stiffness to weight can be achieved.

Laminated composites can be different from fiber-matrix form. For instance, bimetals, clad metals, laminated glass or plastic-based laminates are the laminated composites, too. Bimetals consists of two different types of metals that are bonded together. In this form, the advantage of thermal expansion coefficient differences between the metals that forms the bimetal can be used. An example of bimetals has shown in Figure 2.5.

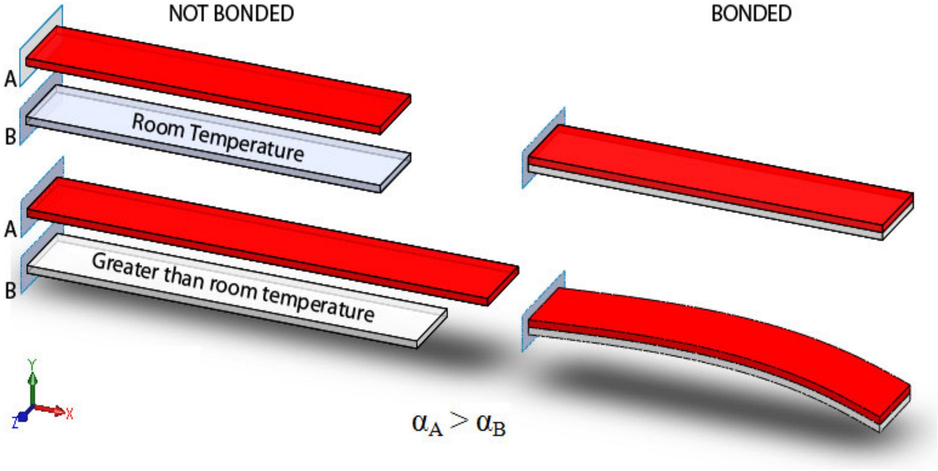

Figure 2.5 A thermostat that is obtained by bonding two different metals.

Clad metals obtained by sheathing a metal with another. For instance, copper wires can be clad with aluminum. So it becomes lighter and durable in fatigue loading. Other example is a laminated glass. Glass is brittle and can break into many sharp pieces. To solve this problem, a thin plastic film can clad with glass. So stiffness and durability in laminated glass can be gained. And a good example of plastic-based laminates is Formica. It is merely layers of heavy kraft paper integrated with a phenolic resin overlaid by a plastic-saturated decorative sheat that, in turn, is overlaid with a plastic-saturated cellulose mat. Heat and pressure are used to bond the layers together. A useful variation on the theme is obtained when an aluminum layer is placed between the decorative layer and the kraft paper layer to quickly dissipate the heat of, for example, a burning cigarette or hot pan on a kitchen counter instead of leaving a burned spot. (Jones, 1999)

➢ Particulate composites: They consist of particles immersed in matrices such as alloys and ceramics. Particular composites can group into nonmetallic particles in nonmetallic matrix composites, metallic particles in nonmetallic matrix composites, metallic particles in metallic matrix composites and nonmetallic particles in metallic matrix composites. They are usually isotropic because the particles are added randomly. Particulate composites have advantages such as improved strength, increased operating temperature, oxidation resistance, etc. Typical examples include use of aluminum particles in rubber; silicon carbide particles in aluminum; and gravel, sand, and cement to make concrete. (Kaw, 2006) There are three types of particulate composites as shown in Figure 2.6.

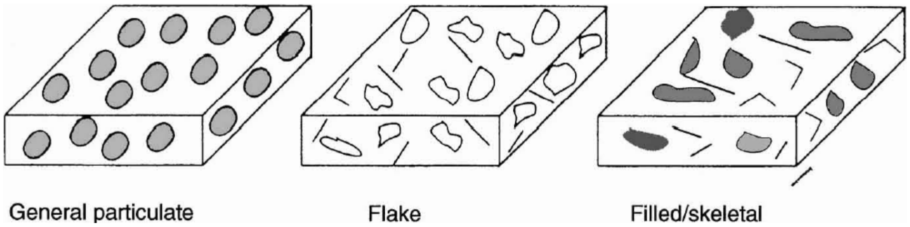

Figure 2.6 Types of particulate composites. (Staab, 1999)

Flake: A flake composite is generally composed of flakes with large ratios of platform area to thickness, suspended in a matrix material (particle board, for example).

Filled/Skeletal: A filled/skeletal composite is composed of a continuous skeletal matrix filled by a second material: for example, a honeycomb core filled with an insulating material. (Staab, 1999)

➢ Combinations of composite materials: They are the mixture of fibrious, laminated, or particulate composites. In this classification method, this type can conflict with the two or three other types of composite classes. For instance, fiber-reinforced concrete is both particulate (the composite is composed of gravel in a cement-paste binder) and fibrious (due to the steel reinforcement). And also, laminated fiber-reinforced composite materials are obviously both laminated and fibrious composite materials. Thus, any classification system is arbitrary and imperfect.

2.3 Manufacturing Process of Composite Materials

The mixture of reinforcement/resin does not really become a composite material until the last phase of the fabrication, that is, when the matrix is hardened. After this phase, it would be impossible to modify the material, as in the way one would like to modify the structure of a metal alloy using heat treatment, for example. In the case of polymer matrix composites, this has to be polymerized, for example, polyester resin. During the solidification process, it passes from the liquid state to the solid state by copolymerization with a monomer that is mixed with the resin. The phenomenon leads to hardening. This can be done using either a chemical (accelerator) or heat. (Daniel & friends, 2003) The discussion of manufacturing of laminated fiber-reinforced composite materials is restricted in this section to how the fibers and the matrix materials are assembled to make a lamina and how, subsequently lamina are assembled and cured to make a laminate.

Fibers are available individually or as roving which is a continuous, bundled, but not twisted, group of fibers. The fibers can be unidirectional or interwoven. A fabricated carbon fiber has shown in Figure 2.7.

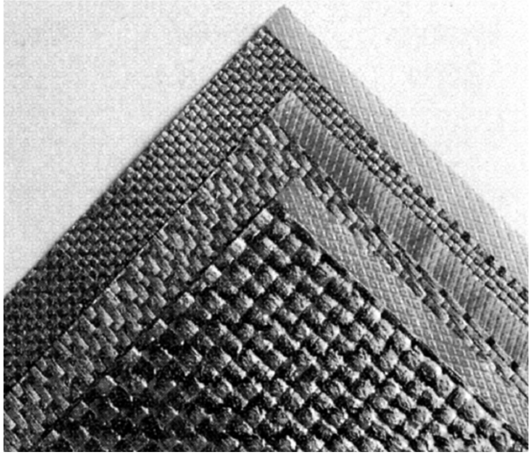

Figure 2.7 Carbon fiber fabrics. (Mazumdar, 2002)

Fibers are often saturated or coated with resin material such as epoxy which is subsequently used as a matrix material. The process is referred to as preimpregnation, and such forms of preimpregnated fibers are called 'prepregs'. For example, unidirectional fibers in an epoxy matrix are available in a tape form (prepreg tape) where the fibers run in the lengthwise direction of the tape (shown in Figure 2.8). The fibers are held in position not only by the matrix but by a removable backing that also prevents the tape from sticking together in the roll. The tape is very similar to the widely used glass-reinforced, heavy-duty package strapping tape.

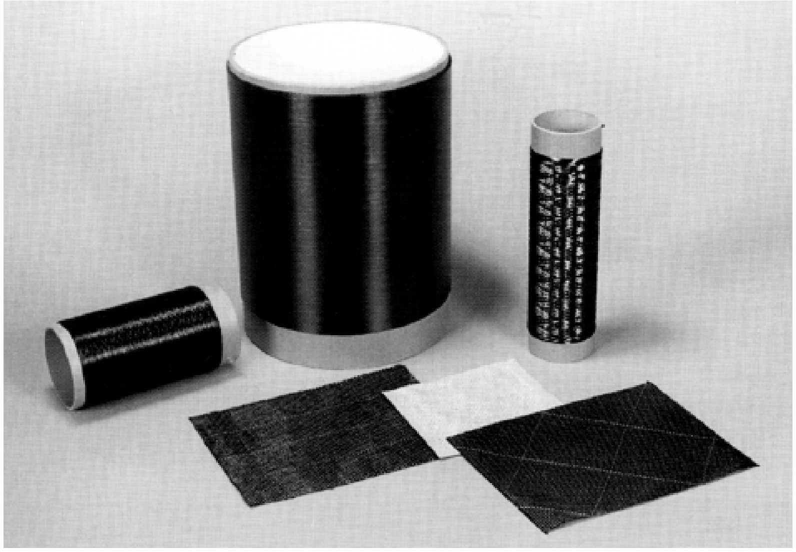

Figure 2.8 Prepreg types: unidirectional tape, woven fabric prepregs, and rovings. (Mazumdar, 2002)

Similarly, prepreg cloth or mats are available in which the fibers are interwoven and then preimpregnated with resin. Other variations on these principal forms of fibers and matrix exist. (Jones, 1999)

2.3.1 Layups

There are three layup processes for fiber-reinforced composites. They are winding, laying and molding. Winding and laying operations include filament winding, tape laying or wrapping, and cloth winding or wrapping. (Jones, 1999)

Filament winding: Filament winding is a process for fabricating a composite structure in which continuous reinforcements (filament, wire, yarn, tape, or other), either previously impregnated with a matrix material or impregnated during winding, are placed over a rotating form or mandrel in a prescribed way to meet certain stress conditions. When the required number of layers is applied, the wound form is cured and the mandrel can be removed or left as part of the structure.

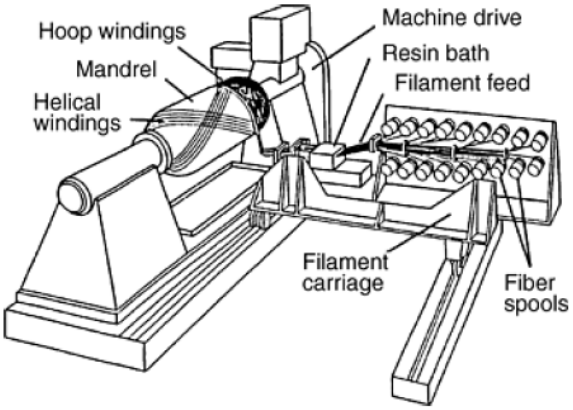

Figure 2.9 Filament winding machine. (Miracle & Donaldson, 2001)

The filament-winding machine (Figure 2.9) traverses the wind eye at speeds that are synchronized with the mandrel rotation, controlling the winding angle of the reinforcement and the fiber lay-down rate. (Miracle & Donaldson, 2001)

Filament winding consists of passing a fiber through a liquid resin and then winding it on, a mandrel. The fibers are wrapped at different orientations on the mandrel to yield strength and stiffness in many directions. Subsequently, the entire assembly, including the mandrel, is cured, after which the mandrel is removed. If the mandrel is a sand casting, then using a water hose to clean out the new pressure vessel dissolves the sand casting. Some mandrels are barrel-stave-like assemblies that must be disassembled through an opening in the new pressure vessel. (Jones, 1999)

Laying: Originally performed by hand, the lay-up process was labor intensive, and inconsistency with hand lay- up caused quality problems with the cured laminates. After 1980s, automated computer numeric control tape-laying machines developed and decrease the production costs and time. Tape laying starts with a tape consisting of fibers in a preimpregnated form held together by a removable backing material. The tape is unwound and laid down to form the desired shape in the desired orientations of tape layers. In the late 1980s, the use of automated tape laying began to focus on commercial aircraft applications. Throughout the 1990s, the equipment, programming, lay-up techniques, and ATL-grade composite materials were further developed to make the tape-laying process more productive, reliable, and user friendly. As of 2001, there are approximately 40 to 45 commercially produced tape-laying machines in the field. (Figure 2.10)

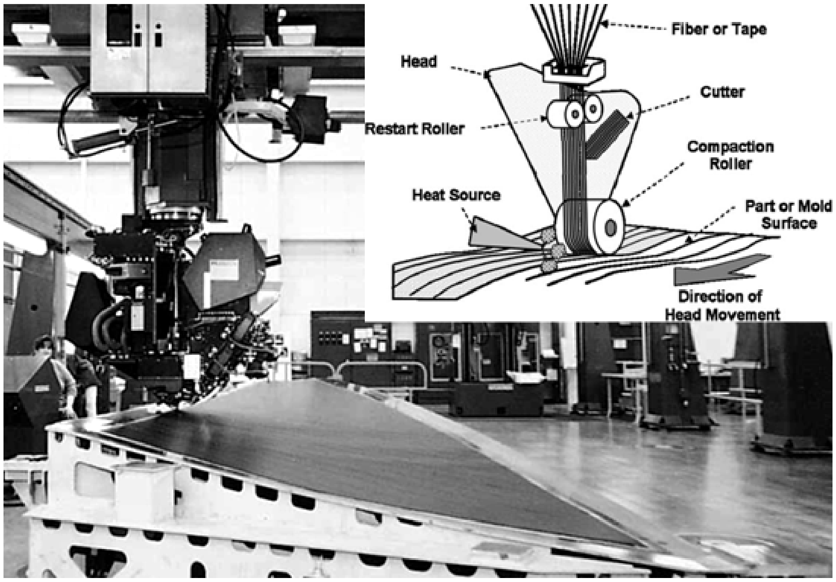

Figure 2.10 Automated tape lay-up of a contour skin. (Miracle & Donaldson, 2001)

Molding: There are many types of molding. They are compression molding, vacuum molding, contact molding, resin-transfer molding (RTM), structural reaction injection molding (SRIM), sheet molding compound (SMC), thick molding compound (TMC), bulk molding compound (BMC), injection molding. Molding operations can begin with hand or automated deposition of preimpregnated fibers in layers. Often, the prepreg layers are also precut. Subsequently, the layers are compressed under elevated temperature to form the final laminate in a press as shown in Figure 2.11. Radar antenna houses or radomes are obtained by molding method to close thickness tolerances.

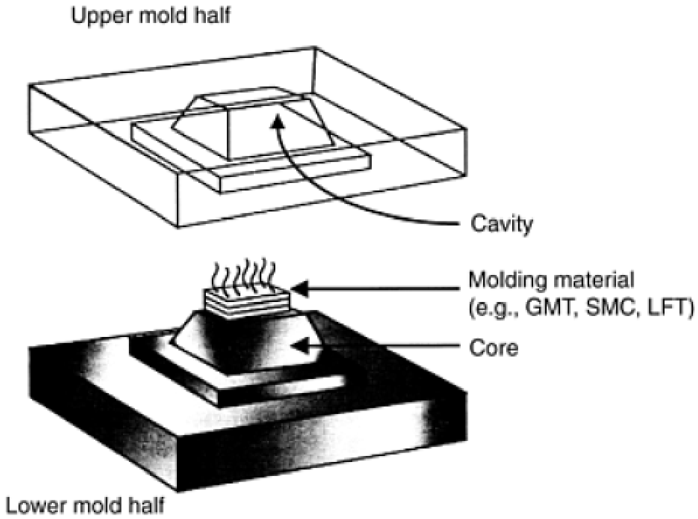

Figure 2.11 Compression molding. (Miracle & Donaldson, 2001)

Resin transfer molding and structural reaction injection molding: Resin transfer molding (RTM) and structural reaction injection molding (SRIM) belong to a family, sometimes denoted liquid composite molding. The common feature is the injection of a liquid polymer through a stationary fiber bed. Resin Transfer Molding (RTM) is a closed mold process in which matched male and female molds, preplaced with fiber preform, are clamped to form composite components (Figure 2.12). Resin mix is transferred into the cavity through injection ports at a relatively low pressure. Injection pressure is normally less than 690 kPa (or 100 psi). The displaced air is allowed to escape through vents to avoid dry spots. Cure cycle is dependent on part thickness, type of resin system and the temperature of the mold and resin system. The part cures in the mold, normally heated by controller, and is ready for its removal from the mold when sufficient green strength is attained. (Peters, 1998)

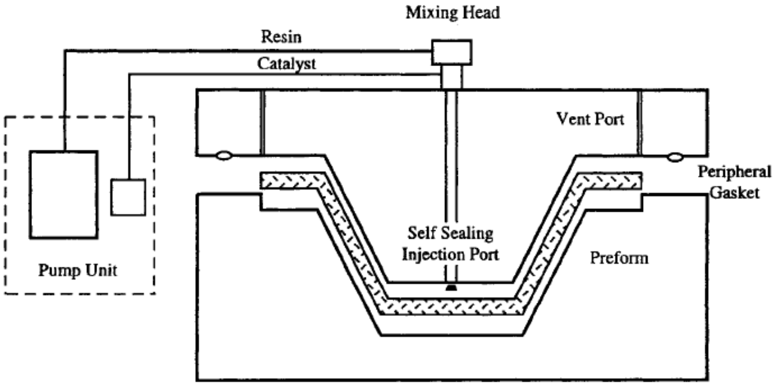

Figure 2.12 RTM process schema. (Peters, 1998)

Contact molding and vacuum molding: Contact molding (Figure 2.13) is open molding (there is only one mold, either male or female). The layers of fibers impregnated with resin (and accelerator) are placed on the mold. Compaction is done using a roller to squeeze out the air pockets. The duration for resin setting varies, depending on the amount of accelerator, from a few minutes to a few hours. One can also obtain parts of large dimensions at the rate of about 2 to 4 parts per day per mold. Vacuum molding is still called depression molding or bag molding.

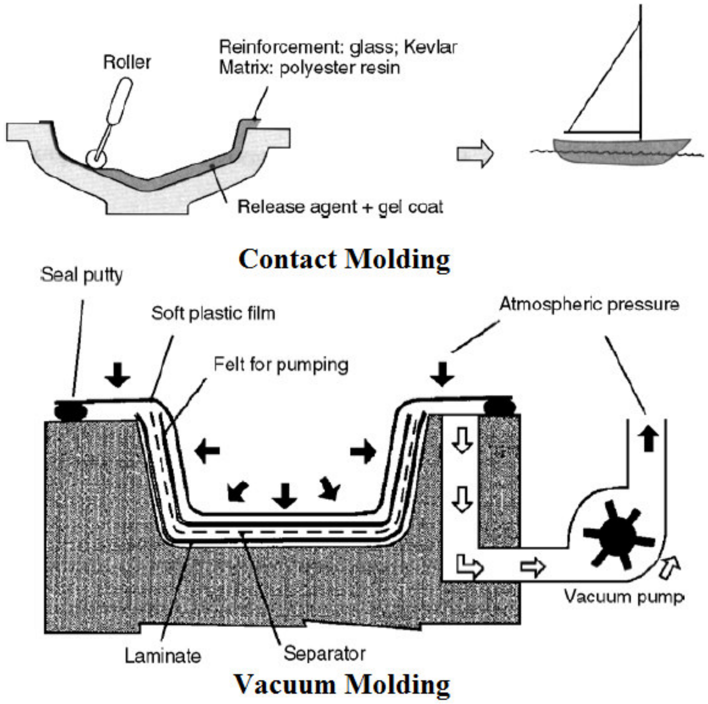

Figure 2.13 Contact and vacuum molding processes. (Daniel & friends, 2003)

As in the case of contact molding described previously, one uses an open mold on top of which the impregnated reinforcements are placed.

Sheet molding compound: SMC (sheet molding compound) is a sheet of ready-to-mold composites containing uncured thermosetting resins and uniformly distributed short fibers and fillers. It primarily consists of polyester or vinylester resin, chopped glass fibers, inorganic fillers, additives, and other materials. A production schema has shown in Figure 2.14. The carrier film is made of polyethylene that protects the roller system from getting gummed up with the resin.

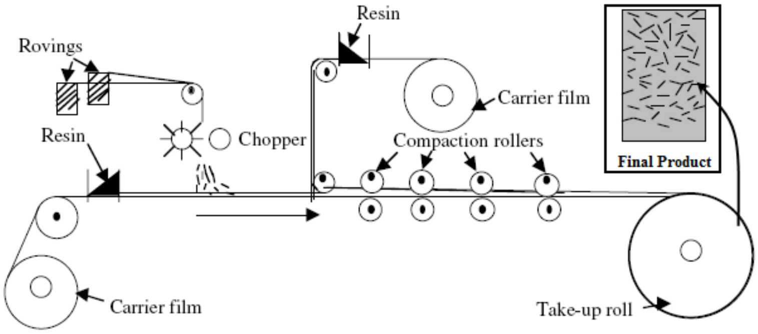

Figure 2.14 SMC manufacturing schema. (Mazumdar, 2002)

Thick molding compound (TMC) is a thicker form of SMC. The thickness of TMC goes up to 50 mm whereas the maximum thickness of SMC is 6 mm. Bulk molding compound (BMC) is a compound that is in log or rope form. It is also known as dough molding compound (DMC). BMC is obtained by mixing the resin paste with fibers and then extruding the compound in log or rope form. (Mazumdar, 2002)

Roll-forming process: The ability of long structural shape production in large quantities is the advantage of this process. Rolls of variously oriented fiber-reinforced tape are the entering material form. .The layers are consolidated and then formed into a hat-shaped stiffener (Figure 2.15)

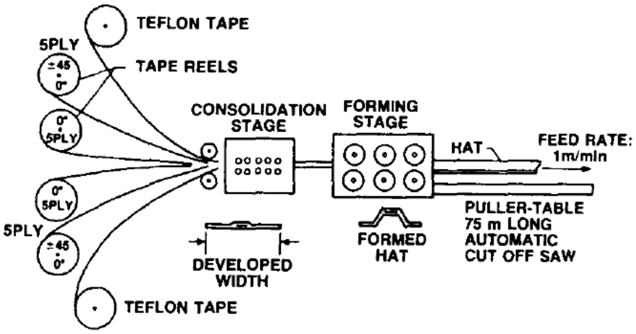

Figure 2.15 Roll-forming production schema. (Jones, 1999)

Pultrusion: This is a cost-effective automated process for manufacturing continuous, constant cross-section composite profiles. Pultrusion refers to both the final product and the process. Most simply, it refers to a method of manufacture wherein a collection of reinforcements saturated with reactive resin is pulled through a heated die that imparts the final geometry to the composite profile (Figure 2.16).

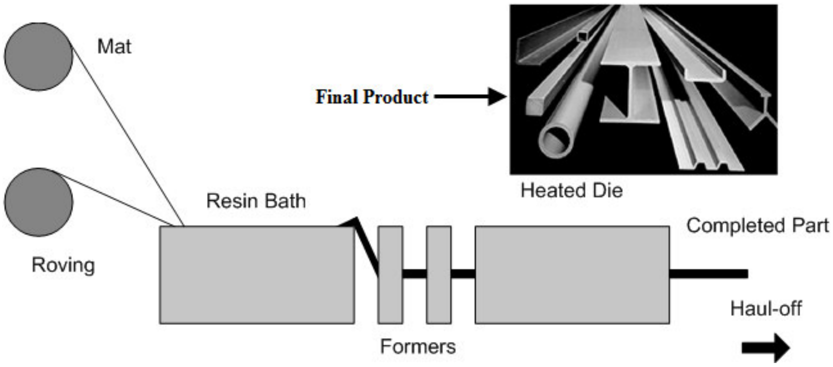

Figure 2.16 Pultrated standard and structural shapes. (Miracle & Donaldson, 2001)

Most of the composite constructions are assembled from the materials that made from combination of many production methods. For instance, a plane wing consists of different composites, and these are produced in different ways (see Figure 2.17)

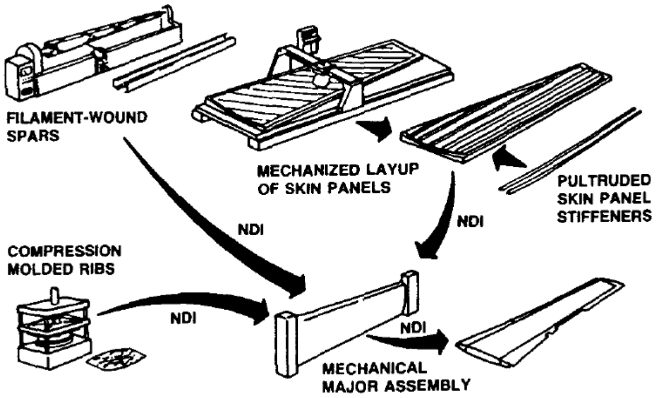

Figure 2.17 Production process of a plane wing. (Jones, 1999)

2.3.2 Curing

Curing is the irreversible change in the physical properties of a thermosetting resin brought about by a chemical reaction, condensation, ring closure, or addition. Cure may be accomplished by the addition of curing or cross- linking agents, with or without the addition of heat and pressure. Curing of resins can also be accomplished using ultraviolet radiation and electron beams, but these methods are used for very specific applications and are not commonly used for composite manufacturing. Processing materials must be added to a composite ply lay-up before autoclave curing. These materials control the resin content of the cured part and ensure proper application of autoclave pressure to the lay-up. In selecting materials for use in preparing a laminate for curing, cure temperatures and pressures must be considered, as well as compatibility of the processing materials with the matrix system.

A typical curing cycle of temperature versus time with notes on other actions is shown in Figure 2.18. The time scale is several hours, and the temperature scale is hundreds of °F (also hundreds of °C). The curing cycle starts with a gradual temperature increase under vacuum conditions so that volatiles and water (vapor) can be driven off. Then, the temperature is gradually increased to the maximum temperature which IS held-for a couple of hours to develop a high degree of cross-linking along with pressure application to consolidate the lamina.

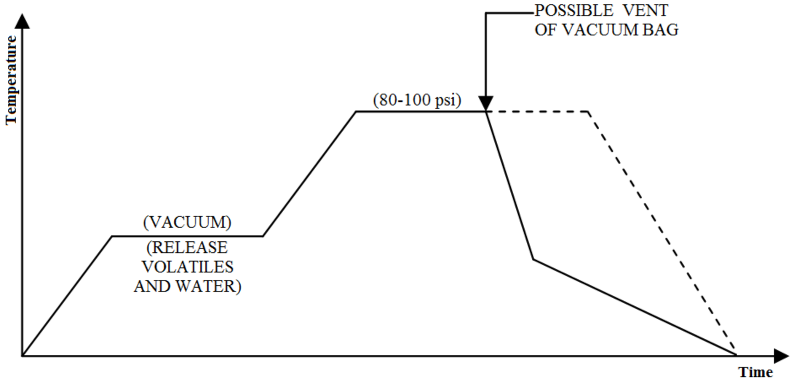

Figure 2.18 Epoxy cure cycle. (Jones, 1999)

As the temperature is gradually increased, resin cross-linking begins and is significant when the gel temperature is reached (the temperature at which the viscosity is so high that no further dimensional change occurs). The progressive cross-linking causes solidification, but the elevated temperature causes softening and hence lowers stiffness. At the highest temperature reached (if the proper prescribed cure cycle is followed which also means that the temperature must be held for a specified time), cross-linking is nearly complete. The resin is now solidified, but is of low stiffness because of the high temperature. Then, the temperature is gradually decreased to room temperature over a period of about an hour to avoid thermal shock. The pressure can be released quickly. If post curing is performed, no further cross-linking occurs unless the previous maximum temperature is exceeded and held for at least an hour (presuming the previous maximum temperature was held for an hour or so). Curing can be performed in several devices: heated mold (Figure 2.11), hot press (heated plates that are forced together), and an autoclave which is essentially a very large version of an ordinary kitchen pressure cooker (Figure 2.19). (Jones, 1999)

Figure 2.19 Autoclave for curing composites. (www.aschome.com, 2008)

2.4 Applications of Composite Materials

Composite materials have lots of applications in industry. Commercial and industrial applications of fiber-reinforced polymer composites are so varied that it is impossible to list them all. In this study, only the major structural application areas, which include aircraft, space, automotive, sporting goods, marine, and infrastructure will be discussed. Fiber- reinforced polymer composites are also used in electronics (e.g., printed circuit boards) , building construction (e.g., floor beams), furniture (e.g., chair spring s), power industry (e.g., transformer housing), oil industry (e.g., offshore oil platforms and oil sucker rods used in lifting underground oil), medical industry (e.g., bone plates for fracture fixation, implants, and prosthetics), and in many industrial products, such as stepladders, oxygen tanks, and power transmission shafts. Potential use of fiber-reinforced composites exists in many engineering fields. Putting them to actual use requires careful design practice and appropriate process development based on the understanding of their unique mechanical, physical, and thermal characteristics.

Aerospace Applications: The major structural applications for fiber-reinforced composites are in the field of military and commercial aircrafts, for which weight reduction is critical for higher speeds and increased payloads. With the introduction of carbon fibers in the 1970s, carbon fiber-reinforced epoxy has become the primary material in many wing, fuselage, and empennage components. The structural integrity and durability of these early components have built up confidence in their performance and prompted developments of other structural aircraft components, resulting in an increasing amount of composites being used in military aircrafts. The outer skin of B-2 (Figure 2.20) and other stealth aircrafts is almost all made of carbon fiber-reinforced polymers. The stealth characteristics of these aircrafts are due to the use of carbon fibers, special coatings, and other design features that reduce radar reflection and heat radiation.

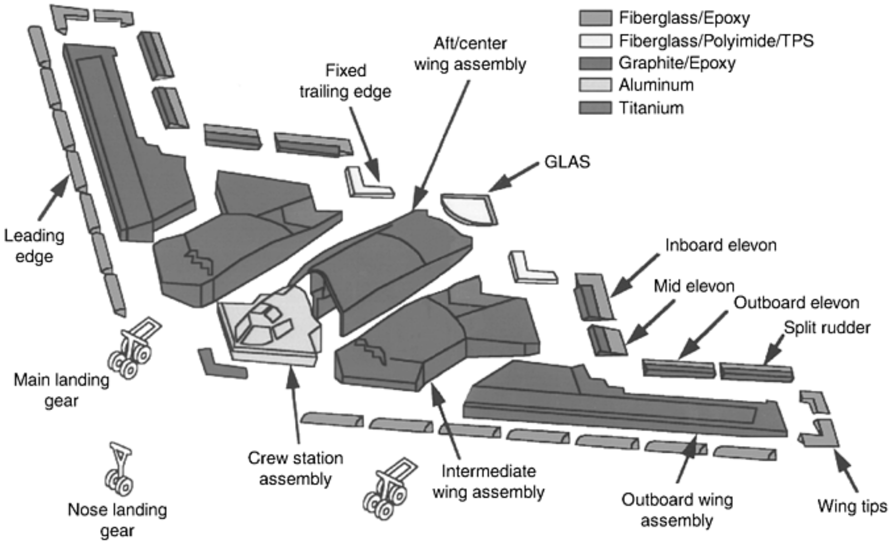

Figure 2.20 The B-2 stealth bomber aircraft, which is made of advanced composite materials. (Miracle & Donaldson, 2001)

Figure 2.20 (cont.)

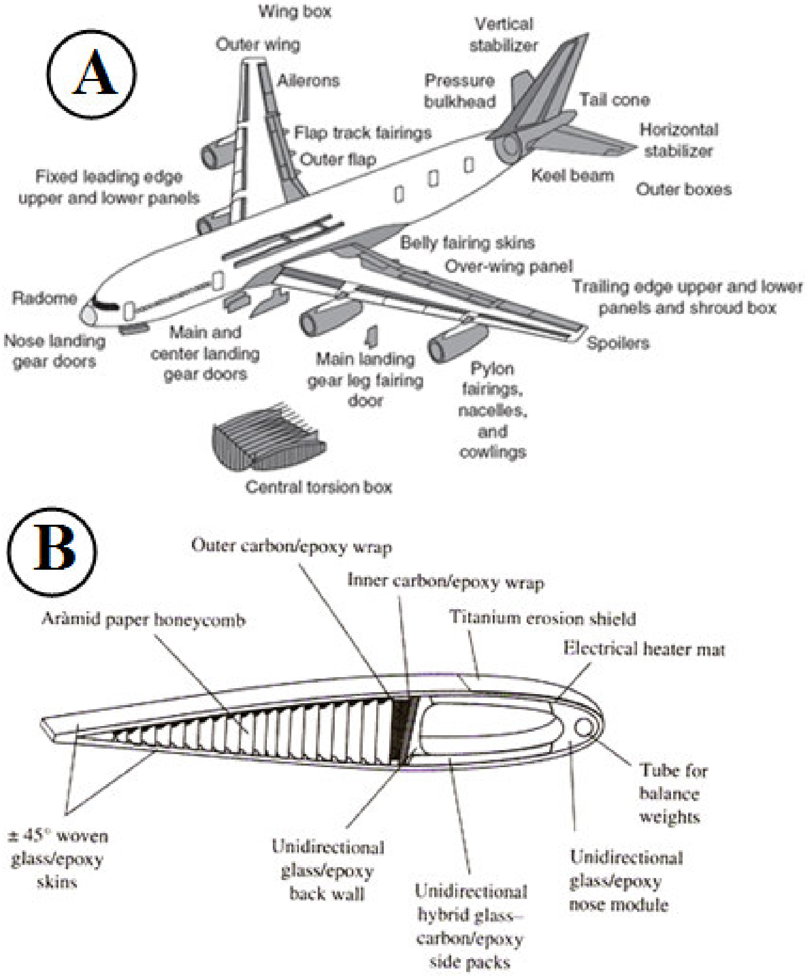

Figure 2.21 Use of fiber-reinforced polymer composites in Airbus 380 (A) (Mallick, 2007)and a helicopter rotor blade section (B) (Gibson, 1994).

Advanced composites are used in air defense and civil applications that shown in Figure 2.21 (A). And in Figure 2.21 (B), composite construction of a helicopter rotor blade has shown.

Space applications: Among the various applications in the structure of space shuttles are the mid-fuselage truss structure (boron fiber-reinforced aluminum tubes), payload bay door (sandwich laminate of carbon fiber-reinforced epoxy face sheets and aluminum honeycomb core), remote manipulator arm (ultrahigh-modulus carbon fiber-reinforced epoxy tube), and pressure vessels (Kevlar 49 fiber-reinforced epoxy). Fiber-reinforced polymers are used for support structures for many smaller components, such as solar arrays, antennas, optical platforms, and so on. A major factor in selecting them for these applications is their dimensional stability over a wide temperature range. A space application of composites has shown in Figure 2.22.

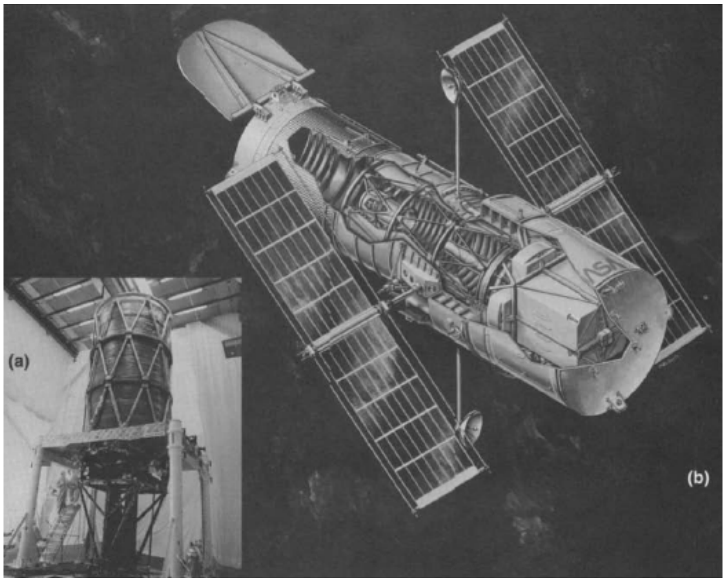

Figure 2.22 Composite structural truss (a) aboard Hubble Space Telescope (b) aligns primary and secondary mirrors. (Peters, 1998)

Automotive applications: Applications of fiber-reinforced composites in the automotive industry can be classified into three groups; body components, chassis components, and engine components. Composites have proven to be very successful in a wide range of exterior body panels and are used in hundreds of vehicle applications. Exterior body components, such as the hood or door panels, require high stiffness and damage tolerance (dent resistance) as well as a ‘‘Class A’’ surface finish for appearance. Excellent surface finish, light weight, and a thermal coefficient of expansion near that of steel have made these applications successful. Customers appreciate the dent and corrosion resistance of composite panels. The composite material used for these components is E-glass fiber-reinforced sheet molding compound (SMC) composites. Another manufacturing process for making composite body panels in the automotive industry is called the structural react ion injection molding (SRIM). The fibers in these parts are usually randomly oriented discontinuous E-glass fibers and the matrix is a polyurethane or polyurea.

Sporting goods applications: Tennis rackets, golf club shafts, fishing rods, bicycle frames, snow and water skis helmets, athletic shoe soles and heels, and the most of the other sporting goods are made of composites. Fiber- reinforced polymers are extensively used in sporting goods and are selected over such traditional materials as wood, metals, and leather in many of these applications. The advantages of using fiber-reinforced polymers are weight reduction, vibration damping, and design flexibility.

Marine applications: Use of composites in marine applications is widespread. The two major advantages of fiber reinforced plastics over metals are resistance to the marine environment, particularly the elimination of galvanic corrosion and the ease of tailoring structures, which are fabricated by molding processes. In addition, composites have high strength-to-weight ratios. (Peters, 1998) Glass fiber-reinforced polyesters have been used in different types of boats (e.g., submarines, sail boats, fishing boats, dinghies, life boats, and yachts) ever since their introduction as a commercial material in the 1940s. Today, nearly 90% of all recreational boats are constructed of either glass fiber-reinforced polyester or glass fiber-reinforced vinyl ester resin.

Infrastructure: Fiber- reinforced polymers have a great potential for replacing reinforced concrete and steel in bridges (Figure 2.23), buildings, and other civil infrastructures. The principal reason for selecting these composites is their corrosion resistance, which leads to longer life and lower maintenance and repair costs.

Figure 2.23 An epoxy/glass fiber-reinforced construction of a bridge. (www.bceo.org, 2008)

CHAPTER THREE

LOW VELOCITY IMPACT IN THIN LAMINATED COMPOSITES

3.1 Introduction

In working conditions, composite structures can exposed to hit by foreign objects. For instance, birds can crash to the plane wing in a flight or in manufacturing process, tools can drop or hit to the composite structure. And the impact loading can be occurred during the takeoff or landing of an aircraft due to the debris or stones in the road. Composite materials are more susceptible to impact damage than a similar metallic material. An impact loading may not be directly damage to the composite. The composite material that subjected to the impact loading could not be failed, and you will see any of damage debris. But inside the material, fiber and/or matrix cracks can occur. Using the material after the load, cracks could grow with the load, and finally material can fail. For these reasons, impact is a big problem in composites and has received considerable attention in the literature. During an impact event, obtaining a detailed description of contact between the impactor and composite structure is not required for the dynamic analysis of impact. But the contact law relating the contact force to the indentation is required.

In commonly used material systems, strain rate effects can be neglected. Hence, the static and the dynamic contact laws are identical. So that, statically determined contact laws can be used in dynamic analysis. In a laminated composite specimen, impactor damages composite and causes a permanent deformation in the contact zone. So, the unloading curve differs from the loading curve. If another impact load is applied to the specimen, reloading curve differs from the first loading curve. This load-unload and reload curves cannot be obtained by numerical methods. They can only be obtained by experimentally. Dynamic behavior of laminated composite specimen must be described accurately to predict the impact dynamics. Simple spring-mass system or two and three dimensional elasticity models can explain some simple cases. There are some sophisticated theories like beam, plate and shell theories that one of them must be chosen to model the structure.

The impact models may not represent the entire structure. For instance, making an impact test to analyze the damage evolution on the structure, a small specimen from the entire structure has to be used. Testing all of the body is very expensive and unnecessary, besides it is impossible (for example, a Airbus A380). There are some types of test mechanisms to simulate impact. A sophisticated type of drop-weight testers will given point to simulate low-velocity impacts.

Impact damage consists of delaminations, matrix cracking, and fiber fracture. On the bases of experimental studies, during the low-velocity impacts, damage initiates with matrix cracks. And this cracks causes delaminations at the interfaces between plies that have different fiber orientations than each other. For thin specimens, bending stresses cause matrix cracking in the lowest ply, and damage propagates through other plies up to the impacted face from the bottom with the matrix cracks and delaminations in ply interfaces, like a reversed pine tree. For stiffer specimens, matrix cracks initiate from the impacted surface of the specimen because of the high contact stresses. And the damage propagates from this surface to the bottom through other plies like a pine tree.

Extensive experimental investigations have revealed that there are no delaminations at the interface between the plies that consist of the same fiber orientations. Delaminations occur because of the fiber orientation angles of adjacent plies. The damage prediction in composites is such a sophisticated event that is not necessary to obtain in detail. Damage propagation starts at the place that first matrix crack occurred. The contact stress transfer continues from this point and in each new matrix crack, the stress distribution changes. After four or five cracks the stress values are more complicated and nearly impossible to determine an exact solution. However, some purely qualitative models explain the orientation and size of delaminations at the interfaces through the thickness of the specimen. The other models predict the onset delaminations by predicting the appearance of the first matrix crack. And in some models, the final state of delaminations can be estimated. Impact-based delaminations cause sudden reduction in stiffness, strength, and stability of the laminate. Hence, impact event is very important in design.

In this chapter, giving essential information about low-velocity impact is aimed. First, the contact laws will be discussed. After that, the two impact models that are spring-mass and energy balance models will e explained. Then, low-velocity impact damage will be explained with the parameters that affecting impact damage. At last, the damage prediction in thin laminates will be discussed.

3.2 Contact Laws

Impact problem can basically be described as shown in Figure 3.1. An impactor that has a mass of *m* kg and a radius of *r* mm with the velocity of *V* drops on the composite plate that is fixed from the outwards of dark surface (top and bottom).

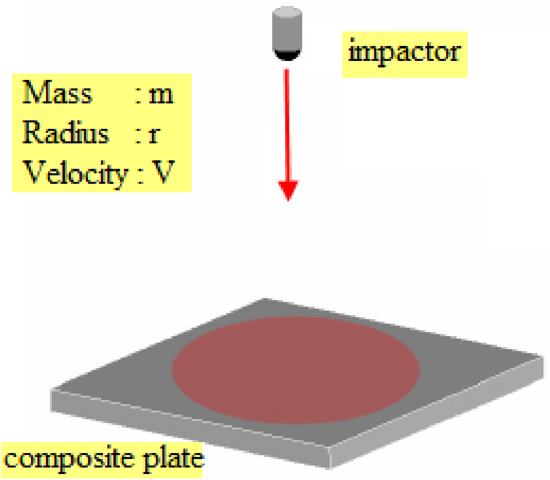

Figure 3.1 A basic model of an impact problem.

Contact law is a relationship between the contact force and indentation, and has been used by Timoshenko to study the impact of a beam by a steel sphere. Contact laws are obtained by experimentally. Because of the case that explained in introduction, the unloading curve differs from the loading curve. Hence, considering the impactor and the specimen as two solids in contact and analyzing it as a dynamic problem is so complicated and cannot describe the effect of permanent and deformation on unloading process. To predict the contact force history and the deformation of the specimen, a detailed model of the contact zone is needless. Impact is a dynamic event. The indentor excites the several vibration modes in composite by hitting the specimen. But in most materials, wave propagation and strain rate effects are negligible; hence the statically determined contact laws can be used in impact dynamics.

The ratio between the energy lost in the half-space and the initial kinetic energy of the sphere is given by (Hunter, 1997),

$$1.04\left(\frac{V}{\left(E/\rho\right)^{\frac{1}{2}}}\right)^{\frac{3}{5}} \tag{3.1}$$

E/ρ is the specific modulus that shows the quality of composites as mechanical advantage. In equation (3.1), V describes the initial velocity of the projectile.

$$c = \left(E/\rho\right)^{\frac{1}{2}} \tag{3.2}$$

‘c’ is the phase velocity of compressive elastic waves in the solid, and it’s greater than the initial velocity of the projectile. After a few microseconds, contact area is very small and the indention is independent of the overall deflection of the specimen. But then, by expanding the contact area, the overall deflection of the specimen affects the pressure distribution under the impactor’s indentor. So, the interaction between the indentor and the specimen must be calculated carefully.

3.2.1 Contact between Two Isotropic Elastic Solids

In this section, it is assumed that the two of the materials in contact are smooth elastic and solid. Essential results from Hertz theory of contact will be used. For two isotropic bodies of revolution (shown in Figure 3.2 (A)), contact occurs in a circular zone with a radius of a in which the normal pressure p is;

$$p = p_0 \left[1 - \left(\frac{r}{a}\right)^2\right]^{\frac{1}{2}} \tag{3.3}$$

, where p_0 is the maximum contact pressure at the center of the contact zone, r is the radial position of an arbitrary point in the contact zone as shown in Figure 3.2 (B).

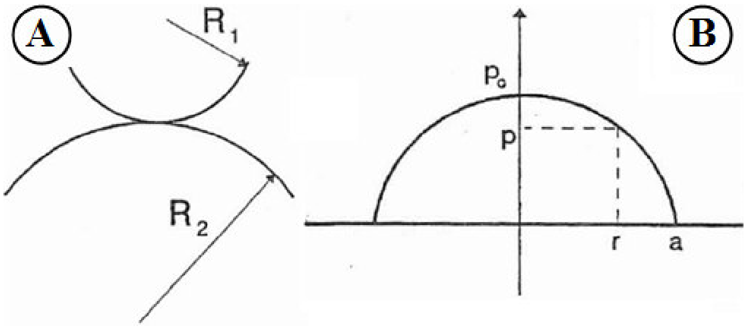

Figure 3.2 Two bodies of revolution for Hertzian analysis of contact (A), and the pressure distribution in the contact zone (B). (Abrate, 1998)

$$\frac{1}{R} = \frac{1}{R_1} + \frac{1}{R_2} \tag{3.4}$$

$$\frac{1}{E} = \frac{1 - \nu_1^2}{E_1} + \frac{1^2 - \nu_1^2}{E_2} \tag{3.5}$$

, where R_1 and R_2 are the radii of two bodies. E is the Young modulus, and ν is the Poisson's ratio. The notation 1 represents the indentor, 2 represents the specimen properties.

$$a = \sqrt[3]{3\frac{PR}{4E}} \tag{3.6}$$

$$\alpha = \frac{a^3}{R} = \sqrt[3]{\frac{9P^2}{16RE^2}} \tag{3.7}$$

$$p_0 = \frac{3P}{2\pi a^2} = \sqrt[3]{\frac{6PE^2}{\pi^3 R^2}} \tag{3.8}$$

$$P = k\alpha^{\frac{3}{2}} \tag{3.9}$$

, where P is the contact force, k is the contact stiffness and α is the indention. Equation (3.9) is referred as *Hertz contact law* and it can be applied to the laminated composites, although laminated composites are not homogeneous and isotropic.

$$k = \frac{4}{3} E\sqrt{R} \tag{3.10}$$

3.2.2 Indentation of A Laminate

In laminated composites, the materials in contact are not smooth elastic. They are elastoplastic. During impact, the contact force reaches its maximum values and then drops down to zero that this is called unloading. But in some situations, the indentor ricochets from the specimen and drops again and this situation can replicate in multiple times. This event causes to occur reloading; therefore, contact laws should include the unloading and reloading phases.

In loading phase, the contact law follows Hertzian law of contact closely. Hence, the equations can be used to obtain the variables. (From the equation (3.3) to (3.10)) On the basis of Crook's investigations, the permanent indention can be obtained as

$$P = P_m \sqrt{\left(\frac{\alpha - \alpha_0}{\alpha_m - \alpha_0}\right)^5} \tag{3.11}$$

$$\alpha_0 = \alpha_m \left(1 - \sqrt{\left(\frac{\alpha_{cr}}{\alpha_m}\right)^5}\right) \tag{3.12}$$

, where P_m is the maximum force before unloading, α_m is the maximum indentation, and α_0 is the permanent indentation. α_{cr} is the critical indentation that represents the minimum value to permanency. This means when $\alpha_{m<}$ α_{cr} there is no permanent indentation. If the α_m is greater than α_{cr} permanent indentation occurs and is given in equation (3.12).

During the reloading phase, the reloading curve distinctly differs from the unloading curve, but always returns to the point that unloading began as shown in Figure 3.3. The unloading curve can be obtained by:

$$P = P_m \sqrt{\left(\frac{\alpha - \alpha_0}{\alpha_0 - \alpha_0}\right)^3} \tag{3.13}$$

From equation (3.13), $P = 0$ when $\alpha = \alpha_0$. The parameter α_0 is related to the actual permanent indentation α_P and the maximum indentation α_m during the loading phase by:

$$\alpha_0 = \beta(\alpha_m - \alpha_P) \tag{3.14}$$

, where the permanent indentation α_P and the parameter β are determined by experiments. To obtain the unloading curve, equation (3.14) is unnecessary, the equation (3.12) enough for it.

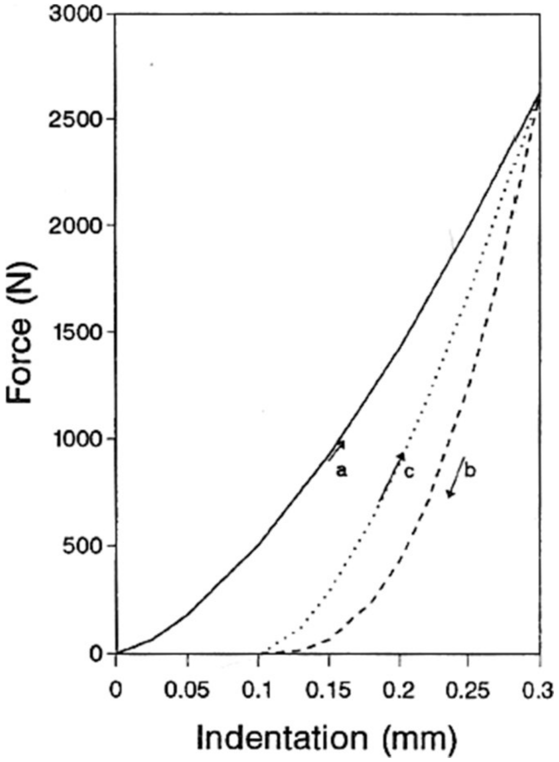

Figure 3.3 Indentation of a laminate. (a) Loading, (b) unloading, (c) reloading. (Abrate, 1998)

In the Figure 3.3, the area under each of the curves gives the energy that spent on loading or reloading and earned with unloading.

3.2.3 The Governing Equation

The governing equation * has shown in eq. (3.15) which is the base equation that finite element code is derived from. (Wu & Chang, 1999)

$$[M]\{\ddot{d}\} + [K]\{d\} = \{F\} \tag{3.15}$$

, where

$[M]$: Mass matrix	$\{\ddot{d}\}$: Acceleration vector	$\{F\}$: Force vector
$[K]$: Stiffness matrix	$\{d\}$: Displacement vector	

* Damping effects are neglected.

The base Equation 3.15 can be developed to solve the impact problem under the Newmark method. At the time $t + \Delta t$ ($all\ equations\ in\ this\ section$ [3.2.3] $are\ related\ to\ this\ time$), the base equation turns into

$$[M]\{\ddot{d}\}^{t+\Delta t} + [K]\{d\}^{t+\Delta t} = \{F\}^{t+\Delta t} \tag{3.16}$$

The velocity vector and the acceleration vectors at this time can be written as

$$\{\dot{d}\}^{t+\Delta t} = \{\dot{d}\}^{t} + (1-\lambda)\Delta t\{\ddot{d}\}^{t+\Delta t} \tag{3.17}$$

$$\{\ddot{d}\}^{t+\Delta t} = \frac{1}{\beta\Delta \mathrm{t}^2}\{d\}^{t+\Delta t} - \frac{1}{\beta\Delta t^2}\{d\}^{t} - \frac{1}{\beta\Delta t}\{\dot{d}\}^{t} - \left(\frac{1}{2\beta} - 1\right)\{\ddot{d}\}^{t} \tag{3.18}$$

where, λ and β are the constants in finite difference method that take $1/2$ and $1/4$ values respectively. By substituting Equation 3.18 into 3.16

$$\begin{aligned}&[M]\frac{1}{\beta\Delta t^2}\{d\}^{t+\Delta t} - [M]\frac{1}{\beta\Delta t^2}\{d\}^{t} - [M]\frac{1}{\beta\Delta t}\{\dot{d}\}^{t} - [M]\left(\frac{1}{2\beta} - 1\right)\{\ddot{d}\}^{t} \\ &+[K]\{d\}^{t+\Delta t} = \{F\}^{t+\Delta t}\end{aligned} \tag{3.19}$$

The equation can be reconstructed as

$$\underbrace{\left([M]\frac{1}{\beta\Delta t^2} + [K]\right)}_{[\hat{K}]}\{d\}^{t+\Delta t} = \underbrace{\overbrace{[M]\left(\frac{1}{\beta\Delta t^2}\{d\}^{t} + \frac{1}{\beta\Delta t}\{\dot{d}\}^{t} + \left(\frac{1}{2\beta} - 1\right)\{\ddot{d}\}^{t}\right)}^{\{H\}^{t}} + \{F\}^{t+\Delta t}}_{\{\hat{F}\}^{t+\Delta t}} \tag{3.20}$$

where, $[\hat{K}]$ is the effective stiffness matrix, and $\{\hat{F}\}^{t+\Delta t}$ is the effective force vector. $\{H\}^{t}$ is a part of the force vector at initial conditions. The sum of the displacements $\{d\}$ caused by a part of the initial force vector $\{H\}$ and the contact force $\{F\}$ at time $t + \Delta t$ can be written as

$$\{d\}^{d+\Delta t} = \{d\}_H^{t+\Delta t} + f^{t+\Delta t}\{d\}_U^{t+\Delta t} \qquad (3.21)$$

where, $f^{t+\Delta t}$ is the contact force at time $t + \Delta t$. This force can be found for two conditions as

$$f^{t+\Delta t} = K\left(\int_0^t \int_0^t \frac{f}{m} dtdt - \delta_{CH}^{t+\Delta t} - f^{t+\Delta t}\delta_{CU}^{t+\Delta t}\right)^{1.5} \qquad \textit{loading case} \quad (3.22)$$

$$f^{t+\Delta t} = f_m\left(\frac{\int_0^t \int_0^t \frac{f}{m} dtdt - \delta_{CH}^{t+\Delta t} - f^{t+\Delta t}\delta_{CU}^{t+\Delta t} - \alpha_0}{\alpha_m - \alpha_0}\right)^{2.5} \qquad \textit{unloading case} \quad (3.23)$$

where, $\delta_{CH}^{t+\Delta t}$ and $\delta_{CU}^{t+\Delta t}$ are the deflection values at the center of the mid-surface in impact direction at time $t + \Delta t$. The contact force $f^{t+\Delta t}$ at this time can be calculated from the Equation 3.22 and 3.23 for each cases by using Newton-Raphson method. The displacement vector $\{d\}^{d+\Delta t}$ can be calculated from Equation 3.21, and the acceleration vectors can be calculated from Equations 3.17 and 3.18. The entire problem can be computerized with a loop, which computes these equations for each timer step. (Wu & Chang, 1989) The finite element code (3DIMPACT) that is used for comparing the experimental study with numerical solutions includes the Newmark method and implicit integration method for non-linear dynamic response calculations. (Aktaş, 2007)

3.3 Low Velocity Impact Damage

In this section, general overview about low velocity impact damage has discussed. The morphology, development and the parameters that effects damage has been given with delamination prediction and experimental methods has explained.

3.3.1 Morphology of Low Velocity Impact Damage

In a laminated composite material, the impact damage consists of delaminations, matrix cracks, and fiber fractures. The term *delamination* means separating the bonded plies from interfaces. Delamination affects the entire structure in sharp strength reductions. Delamination is an inter-ply event and has a direct relation between the differences in the ply orientations. In any inter-plies that have the same ply orientations occur delamination. Delamination area has a peanut-like shape that the waist of peanut is under the contact point as shown in Figure 3.8.

Several investigations revealed that, delaminations occur when the contact force reaches at a threshold value. This value could not be predefined including all laminates or a specified orientation. The threshold value can only be obtained by experiments. However, producing completely identical specimens is not possible, so that, the threshold level of the initial contact force can be differ from one to another. The experimental studies indicate that delamination starts with the first discontinuity in the contac*t* force history that indicates the threshold contact force value. There is no relation between the initial kinetic energy with delamination.

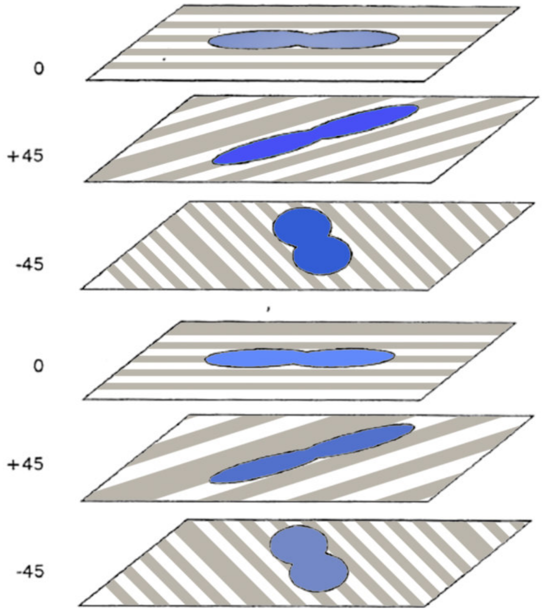

Figure 3.8 Orientation of delaminations. (Abrate, 1999)

Delamination is independent from kinetic energy. Sjoblom proposed a simple model to explain the initial contact force that starts delamination in 1987. The radius of the contact zone that occurred with the contact force P is $r = (D\alpha)^{1/2}$ that D represents the diameter of indentor and α is the indention. Hertz contact law can be expressed with assuming the transverse shear stress is distributed uniformly over a cylinder with a radius of r, and height of h in the form of

$$P = (2\pi h\tau_{max})^{\frac{3}{2}} D^{\frac{3}{4}} k_c^{-\frac{1}{2}} \tag{3.24}$$

, where P is the initial contact force and k_c is the contact stiffness. The experimental studies on this equation proofs that P increases with $h^{\frac{3}{2}}$.

The damage process is initiated by matrix cracks. There are two types of matrix cracks; tensile and shear cracks. Tensile cracks initiate when the inplane normal stress exceed the transverse tensile strength of the ply. The shear cracks occur due to the transverse shear stresses. Shear cracks initiates at an angle from the midsurface.

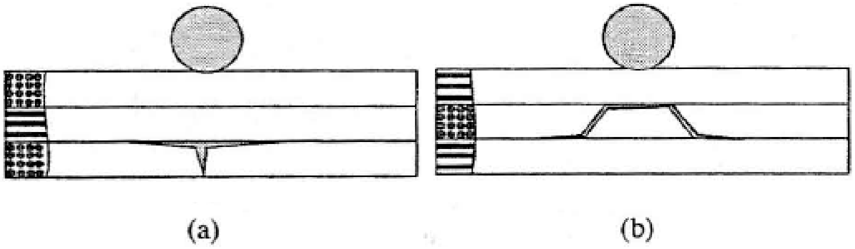

Figure 3.9 Tensile or bending crack (a), and the shear crack (b). (Abrate, 1999)

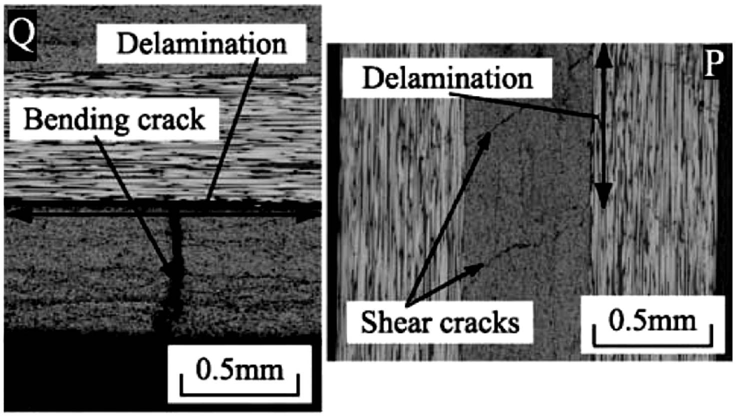

Figure 3.10 Cross-sectional micrographs, showing bending and shear cracks. (Takeda, Minakuchi & Okabe, 2004)

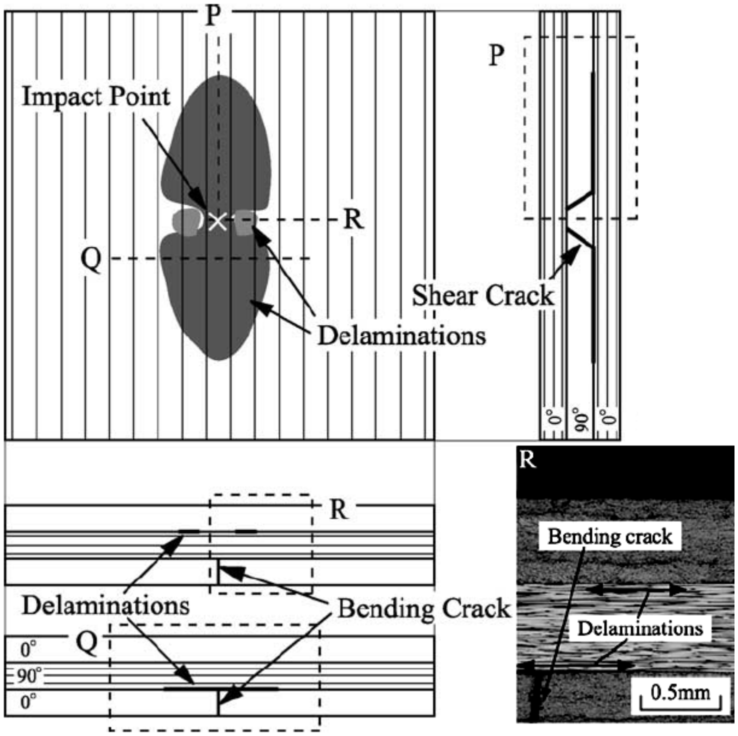

Figure 3.10 (cont.)

The tensile and shear matrix cracks have shown in Figure 3.9 and in Figure 10 (detailed). In thick laminates, matrix cracks initiate from the surface that exposed to impact damage directly, because of the high localized stresses, and grow like a pine tree pattern as shown in Figure 3.11 (a). In thin laminates, matrix cracks start from the opposite face of the impacted force because of the bending stresses, and grow with delaminations like a reversed-pine tree pattern as shown in Figure 3.11 (b).

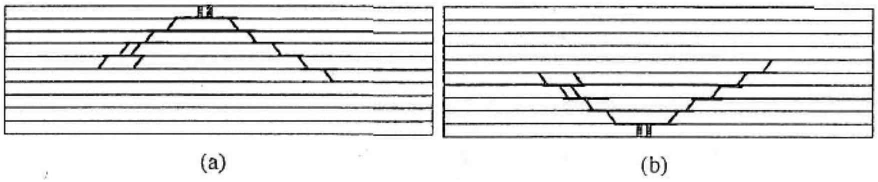

Figure 3.11 Pine tree (a), and the reversed-pine tree (b) damage patterns. (Abrate, 1999)

3.3.2 Damage Development and Qualitative Models for Predicting Delamination Patterns

In relatively low (to the thickness) initial kinetic energy impact damages, delamination may not be occurred. For thin laminated composite specimens, the relatively low impact energy cause matrix cracks on the bottom face, and it does not develop. The force-time curves are relatively smooth, and exhibit almost an elastic behavior. Matrix cracks can occur easily. They don't need high energy levels to start, and they do not cause a sudden drop in stiffness. But in higher impact energy levels, matrix cracks can develop rapidly with large delaminations, and they drop the stiffness of the structure down with the help of delaminations.

Several investigations have been made to predict delamination patterns. There are two simple models that explain the reasons that delamination occurs when the laminate subjected to localized loads. Both of the two models are valid for the case that, the laminate is made up of several orthotropic layers. This case causes a problem, like deflection of the composites that each of them are made of different metals and bonded together with glue, then subjected to the thermal loads under a heat source. During the impact loading, bending stiffness of the layers, that are bonded together, are different from each other; or there is a mismatch in their bending stiffness. Hence, interlaminar stresses are different from each ply group, either. Each layer attempts to deform in a particular way, and transverse normal and shear stresses applied at the interfaces restrict the layer to behave as one plate. When these stresses become too large, delamination occurs.

The first model *'bending stiffness mismatch'* proposed to predict the orientation, size, and shape of the delaminations by Liu in 1998. According to this model, delaminations occur, because the sub-laminates above and below a given interface have different bending rigidities. In this model, it is assumed that delaminations occur due to the bending rigidities between two plies. The mismatch coefficients are given as

$$M = \frac{\left[D_{ij}(\theta_b) - D_{ij}(\theta_t)\right]}{\left[D_{ij}(0^0) - D_{ij}(90^0)\right]} \tag{3.25}$$

, where the D_{ij} are the components of bending rigidity matrix D relating moment resultants to plate curvatures. Each ply is considered separately, so $D_{ij}(\theta_b)$ is the rigidity of the bottom layer, and $D_{ij}(\theta_t)$ is the rigidity of top layer.

Another model presented to find out why two layers with different orientations should delaminate when subjected to concentrated transverse loads by Lesser and Flippov (1991) If the layers are not bonded together, during the impact loading, each ply will deform separately. But in bonded mode, the each of the plies that are in contact with interfaces, and will be restricted to deform together as one plate. In this case, the same shape delamination occurs at interfaces due the same interlaminar stresses acting on each interface.

3.3.3 Test Methods of Impacted Laminates

After the impact loading, the damage inside the laminates is necessary to comment on the experiment. For semi-transparent composites, like Kevlar or glass epoxy composite, delamination can be observed with a spot directed to the damaged area. But for opaque composites, observing internal damages is quite complicated. There are two main types of test methods that the one is destructive, and the other is non-destructive technique.

In destructive technique, the impacted laminate is exposed to several chemical processes to debond or deply each lamina. Then, the separated lamina strips examine in microscope to indicate delaminations and the matrix cracks of each ply. The debonding process begins with cutting the slices with a diamond lapidary saw using water spray to minimize local heating. Then, composite is mounted in epoxy resin and ground on a finer abrasive silicon carbide paper. Or a gold chlorine solution with an isotrpoyl carrier is used to reveal the damaged area. For light-damaged composites, small holes can be drilled to penetrate the solution through the laminate. When the solution dried, it precipitates over the fracture surfaces. Then, the matrix is pyrolised in an oven at about 420 ^{o}C. After that, the laminate can be separated into individual parts.

If the non-destructive techniques are compared with destructive, the non-destructive technique is expensive and requires sophisticated equipments to carry out. The C-scans, ultrasonic inspections, infrared thermography, vibro-thermography, tapping technique, optical, and electrical techniques are used to determine the presence of eventual impact damage over the laminate. C-scan technique depends on reflecting x-rays throughout to the damage area and taking its photograph. This method indicates a crude vision of impacted plies. Many of the features of damage area are lost, and it does not show how delaminations distributed through the thickness or their size/orientation (shown in Figure 3.12). To overcome these problems, improved ultrasonic inspection techniques have been developed.

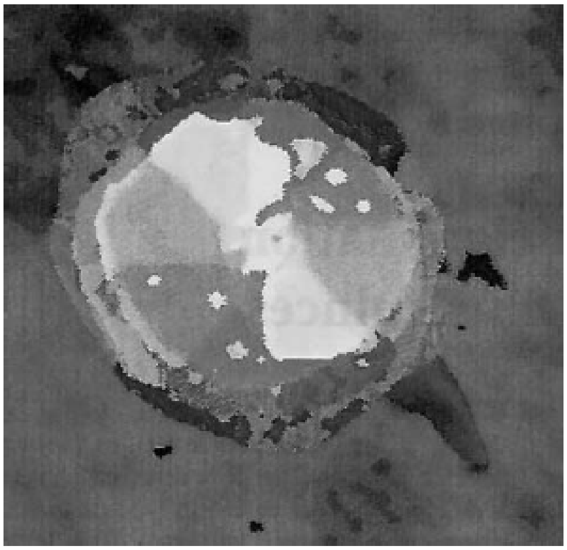

Figure 3.12 Ultrasonic C-Scan of a $[45_2^o, 0_2^o, -45_2^o, 90_2^o]_s$, 7.1 J impacted laminate. (Guinarda, Allixb, Gue´dra-Degeorgesa & Vineta, 2000)

In infrared thermography technique, damaged laminate is placed into a heated water tank, and exposed to a heat flow. Then the temperature on the surface of laminate is measured with a thermovision system, hence the heat conducts through the delaminations. The temperature differences on the thermophotograph of laminate delineate the damaged areas inside the specimen. In the vibro-thermography technique, high frequency and low amplitude mechanical vibrations are exposed to the laminate. The stresses caused by vibrations concentrate at the delamination areas. Then taking a thermal picture of the specimen shows the damage inside the specimen. In tapping technique, the laminate is tapping lightly, and analyzing the propagation of the sound waves throughout the specimen. The frequencies of the sound waves that travelling inside the laminate differs at the delaminations. Hence, the damaged and undamaged regions can be observed from the frequency spectrum. The real-time damage monitoring can be possible with using a widely spread array of embedded optical fibers. In this technique, optical fibers placed that the light is transmitted throughout the specimen and received to the sensors that are connected to the computer. When a fiber fracture occurs during the impact, the light transmission stops, then the computer detects the damage and its location in real-time. The last technique is the electrical method. In this method, electrical current is applied along the carbon fibers, and electrical field is measured. When a fiber fracture occurs, the current releases and leaks through the specimen; then the electrical field changes. This change in the electrical field creates detectable perturbations in the magnetic field. By measuring the changes in magnetic field, the location and extend of the damage can be detected.

The damage development can be observed with high speed cameras. These cameras can record the motion up to 40000 fps that means taking photographs with 25µs intervals. The damage propagation can be recorded to the camera. After that, the delaminations and the damage propagation can be examined and comment on. Another technique is the Shadow-Moire that helps us to observe the damage development. In this technique, a stationary master grid placed lose to the specimen remains undeformed, while the grid formed by the shadow of that master grid on the specimen will deform with the specimen. The interference of the master grid and its shadow produce dark and bright fringes from which the normal displacements of the panel could be determined. The high speed cameras can be used to record the damage propagation, either.

3.3.4 Parameters Affecting The Impact Damage

There are so many parameters that affect the impact damage. Material properties, target stiffness, projectile characteristics, layup and stitching, preload and the environmental conditions have influences on impact damage. Some material properties of composite specimen like $(E_1, E_2, \nu_{12}, G_{12})$ affect the impact dynamics or the strength of the laminate. The matrix material, reinforcement and interface properties have a distinct effect on impact resistance. And also, the bending stiffness mismatch coefficient (eq. 3.60) and the contact stiffness k_c have effects on impact damage. Lowering the contact stiffness lowers the contact forces and increases the contact area. By lowering contact stiffness, delaminations can reduce. It has been discussed before that damage initiates with matrix cracks. When a matrix crack reaches an interface between layers with different fiber orientations, delamination starts. Hence, the threshold kinetic energy is efficient in matrix cracks. Matrix cracks are independent from the fiber type and the fiber property. So, the type of fibers being used does not seem to affect the onset of matrix cracking and delaminations. For higher levels of impact energy, fibers that have higher failure strains are expected to improve the impact resistance of the composite.

During the impact damage, a new layer that has a very high toughness and high shear strain resin can arise at interface between the plies. This situation is called *interleaving*, and it improves the impact resistance significantly. For reducing interlaminar shear stresses, adhesive layers can be placed along interfaces of a laminate. This will reduce the delaminations. For epoxy-glass composites, inserting a rubbery interface between the fibers and the matrix can achieve the impact resistance.

Stiffness of the specimen plays a significant role as discussed before. For flexible specimens, the impact load causes bending at the lower plies in low velocities. First, at the lowest ply the matrix cracks, then it grows like a chaining reaction towards the impact face with drawing reversed pine tree model. For stiffer specimens, the crack initiates from the contact surface with a pine tree model. These models have shown in Figure 3.11.

Damage can be influenced by the characteristics of projectile. A steel or aluminum impactor causes different damage areas in the specimen. The steel projectiles produce slightly more damage. This difference can be enlighten with the higher elasticity modulus of steel that gives a higher contact stiffness, which induces higher contact forces and smaller contact zone. At the other hand, there is no relation between stacking sequence and the projectile type directly.

Damage initiation is matrix and interface dependent, so the damage initiation is not depend on stacking sequence. But during the impact, the peak load or the energy at the peak load is strongly depend on stacking sequence.

The thickness of plies which have different orientation with subsequent plies, is so important that increases the delamination size. And increasing the orientation angle differences between interacting plies causes higher delaminations. Increasing the differences between the longitudinal and transverse modulus of the specimen leads to higher bending stiffness mismatching that increase delamination. Stitching the laminate is an extra production step that can improve the damage resistance and can reduce the delaminations. But it has some drawbacks that fiber damage can occur due to the needle during stitching, or resin-rich pockets can introduce by the needle which cause stress concentrations and can reduce the strength of the laminate.

Laminates can be preloaded before the experiment that in real applications, most laminates are preloaded due to the structural connections. Preloading or pre-tension decreases the time required to reach the maximum impact load and increases the indention depth that is the stiffening effect of preloading. The investigations revealed that pretension drastically reduce the impact energy required to produce final fracture of ceramic-matrix-composites.

Temperature is the most important effect that changes properties of entire system, directly. The other factors are the moisture and the saturated solutions to the laminate. A remarkable study on the effects of environmental conditions to the impact damage has proposed by Strait et al. in 1992. This study has showed that the threshold kinetic energy is increased significantly when glass fiber-reinforced composites are subjected to long-term exposure to sea water before impact, and the peak load during impact and the total absorbed energy are dramatically reduced. (Abrate, 1998)

3.4 Damage Prediction in Laminates

The tensile and shear cracks are discussed in previous sections that tensile and shear cracks occur in thin laminates. In this section, the damage prediction with damage initiation and the propagation of delaminations during impact damage will be discussed.

Delamination propagation directions change if they were shear or bending originated as shown in Figure 3.13 (A and B).

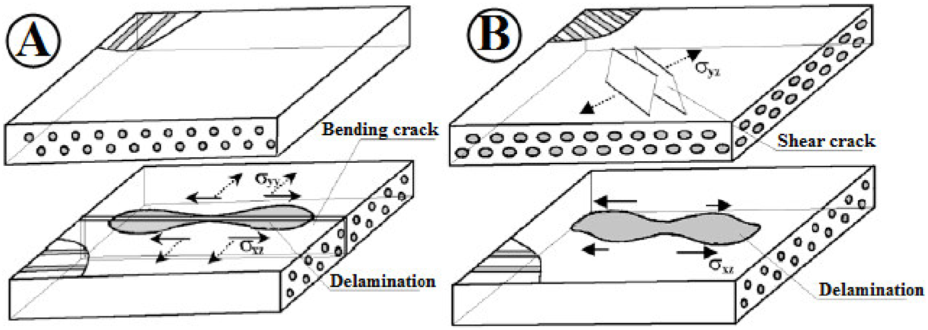

Figure 3.13 Propagation of delaminations induced by bending (A) or shear crack (B).

The transverse normal stress is usually small, so σ_{zz} can be neglected. For 2-D impact problem of beam subjected to a cylindrical impactor, σ_{xz} is also zero. After these simplifications, eq. 3.26 can be obtained as

$$\left(\frac{\bar{\sigma}_{yy}}{Y}\right)^2 + \left(\frac{\bar{\sigma}_{yz}}{S_i}\right)^2 = e_M^2 \tag{3.26}$$

, where S_i is the in-situ transverse shear strength, and Y is the in-situ transverse normal strength. $\bar{\sigma}_{yy}$ and $\bar{\sigma}_{yz}$ are the average stresses over the thickness of the ply. The strength *Y* is taken as: $\sigma_{yy} > 0 \;\; => \;\; Y = Y_t, \qquad \sigma_{yy} < 0 \;\; => \;\; Y = Y_c$

If matrix cracking is predicted in a layer of the laminate, a delamination can be initiated from the crack. Choi and Chang (1992) proposed impact-induced delamination growth criterion for low-velocity impact; that can be as

$$D_a\left[\left(\frac{{}^{n}\bar{\sigma}_{yz}}{{}^{n}S_i}\right)^2+\left(\frac{{}^{n+1}\bar{\sigma}_{xz}}{{}^{n+1}S_i}\right)^2+\left(\frac{{}^{n+1}\bar{\sigma}_{yy}}{{}^{n+1}Y}\right)^2\right]=e_D^2 \tag{3.27}$$

, where D_a is a constant which has to be determined from experiments. *n* and *n+1* corresponds to the upper and lower plies of the *n*th interface, respectively. $\bar{\sigma}_{yz}$ and $\bar{\sigma}_{yy}$ are the averaged interlaminar and inplane transverse stresses within the *n*th and *(n+1)*th ply, respectively. $\bar{\sigma}_{xz}$ is the averaged interlaminar longitudinal stress within the *(n+1)*th ply. (Karakuzu, Aslan, Okutan, 2002) According to this equation, if $e_D \geq 1$, matrix cracks. The strength *Y* is taken as

$$\bar{\sigma}_{yy} \geq 0 \;\; => \;\; Y = Y_t, \qquad \bar{\sigma}_{yy} < 0 \;\; => \;\; Y = Y_c \tag{3.28}$$

CHAPTER FOUR

PRODUCING LAMINATED COMPOSITES FOR EXPERIMENT

In this chapter, the production process of the specimen explained with pictures. Our specimens have same orientation and same thickness with each other. They are nearly identical. Number of plies and the fiber orientations defined by the supervisor, and set to be $[0/30/60/90]_s$. This 8 plies laminate consist of epoxy matrix, and glass fibers. And also, the edge length of the square specimen is defined as 100 mm.

Unidirectional E-glass fabric having weight of 509 g/m2 was used as reinforcing material. The first step of the manufacturing process is determining the optimum plate size that will be cut to obtain specimens. The height of the roller is 1270 mm as shown in the Figure 4.1 (A). A virtual circle is assumed to have the diameter of 1270 mm, and then a square is drawn into the circle that has the maximum area. The edge length of this square is obtained as $1270/\sqrt{2} \cong 898\ mm$. Then, the square is drawn to the glass fiber in 30° angle and cut with a scissor as shown in Figure 4.3. Four pieces have been cut at this angle to provide the requirements. The 60° is needless, because this angle can be obtained by flipping and rotating the fiber as shown in Figure 4.1 (C) and (D). Then 4 copies of other pieces have been cut in 0° angle (similarly, 90° fiber angle can be obtained by rotating) as shown in Figure 4.2.

In the second step, the epoxy (CY225) and hardener (HY225) curing resin are prepared by mixing them in a heater. The mixing ratio is 1/1. Then, the heater has set to a temperature of $90\ °C$. While the oven was heating the resin, the next step have been performed.

In third step, a sheet metal is laid down at the middle of the doubled nylons before orienting the plies. Then, the lowest ply at 0° angle is laid down. Meanwhile, the resin is blended at the elevated temperature. Then, the resin is applied to the

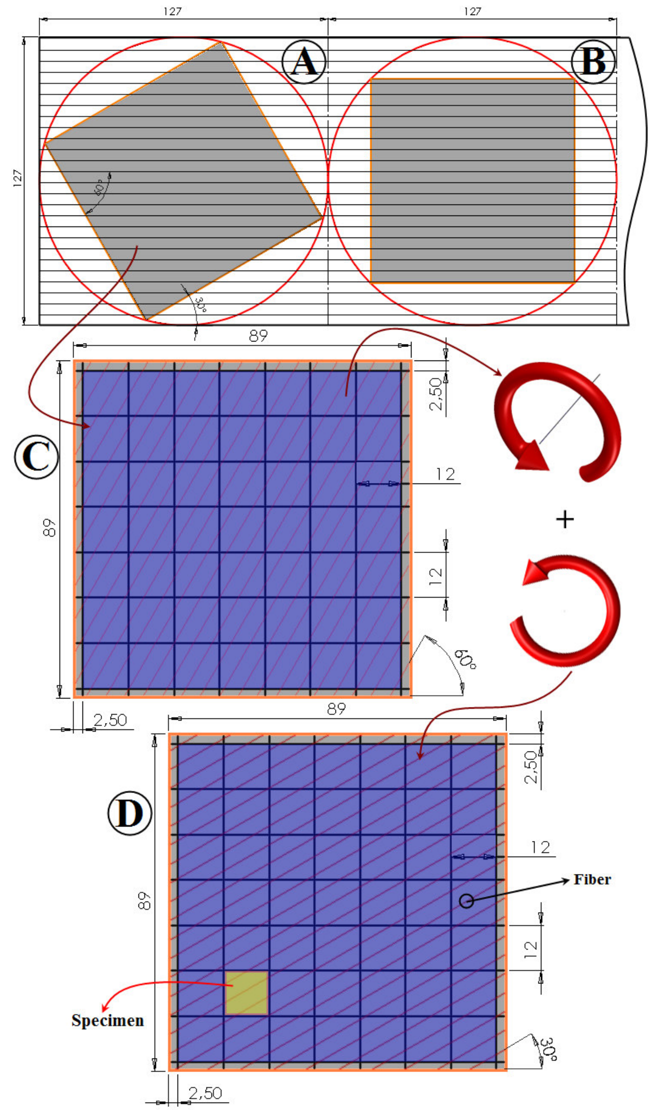

Figure 4.1 Cutting schemas of fiber blocks for 30° and 60° (A, C, D), with 0° and 90° (B). [Lengths are in *cm* unit.]

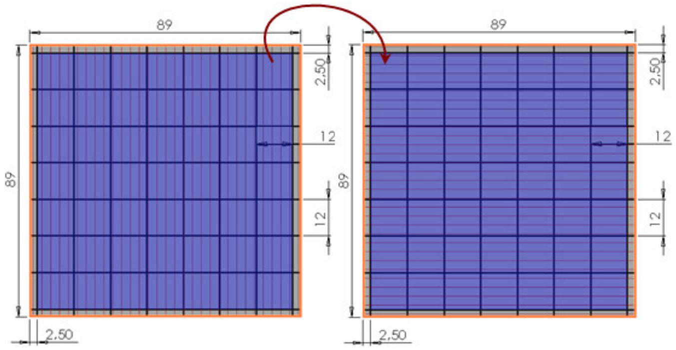

Figure 4.2 Changing the fiber angle for 90° to 0° or 0° to 90°. [Lengths are in *cm* unit.]

first ply with rollers. The rolling speed is neither fast nor slow; it's at a speed which does not let the resin to dry.

When the lowest ply finished, the following two plies have lay down with the angle of in $30°$ and $60°$ respectively. The resin is applied to the single ply only at the bottom and top plies. At the other plies, the resin is applied to the doubled fiber plies. After the last fiber ply is resined, the laminate is covered with nylon. Then, the second sheet metal had put before curing, and covered with nylon to avoid resin leakage. At the fourth step, the laminate is covered by sheet metals and covered by nylons, and then put into the hot press. Curing process materialized at the pressure of $150\ bar$ and the temperature of $120\ °C$ for 2 hours.

Figure 4.3 Product is ready for test.

After the curing process, the laminates are cut into the squares that each laminates have the edge length of 100 mm. A finished specimen has shown in Figure 4.3. The final thickness of the composite specimen is about 2.9 mm.

CHAPTER FIVE

LOW VELOCITY IMPACT EXPERIMENT AND FINITE ELEMENT RESULTS

5.1 Introduction

In this chapter, the impact tester will be introduced, and then the experimental conditions will be given. Subsequently, the mechanical properties of specimen and the impactor will be given. After that, the results –calculated with 3D impact code- will be discussed. Finally, the experimental results will be compared with the software results.

5.2 Impact Test Machine and Test Conditions

The *guided falling weight* technique is applied for all specimens with the tester machine called *“Fractovis Plus”* as shown in Figure 5.1. A schematic diagram of the impact testing machine was given in Figure 5.2. According to the diagram, the impactor consists of three components: a dropping crosshead, an impactor rod or striker, and an impactor nose. The steel impactor rod has a diameter of 12.7 mm and is attached to the dropping crosshead. A piezoelectric head striker is used in the experiments. It is characterized by higher robustness which makes it more suitable for testing very hard materials like advanced composites. A force transducer having a capacity of 22.24 kN was mounted on the front end of the impactor striker and encapsulated by a hemispherical nose. The impactor was set at a dropping height of 30~1100 mm to give a constant impact velocity at 0.75~4.6 m/s for tests.

Figure 5.1 Fractovis Plus Low velocity impact tester (A) and its equipments; impactor nose (B_1), piezoelectric impactor nose (B_2), Data Acquisition System (DAS) (C), the specimen clamp mechanism (D), and the springs (E).

The total mass of the impactor, however, ranged from 2 to 70 kg (by adding various deadweights (shown in Figure 5.4) to the crosshead), resulting in impact energy from 0.6 to 755 J. For impact energy higher than 755 J, an additional energy system (springs have shown in Figure 5.1 (E)) can be integrated which supports up to 1800J. The tester has also a built-in heater and cooler (if a nitrogen tube is connected) which are connected to the computer through advanced data acquisition system (DAS) (shown in Figure 5.1 (C)).

In each impact test, a composite specimen with dimensions of 100 mm x 100 mm was placed between two steel plate holders as shown in Figure 5.2.

The composite specimen thus had a fixed (22500 N clamping force) boundary condition (in Figure 5.3). In impact testing, the impactor contacted the center of composite specimens, resulting in so-called central impact.

As the impactor dropped and approached the composite specimen, its time trigger passed through a time sensor (Figure 5.2) right before contact-impact occurred. The initial impact velocity was then calculated from the distance between two edges on the time trigger and the time interval they passes through the sensor. Once impact began, the contact forces at many consecutive instants were detected by the force transducer attached to the impactor. The force history data was send through DAS and downloaded to a computer for graphical processing.

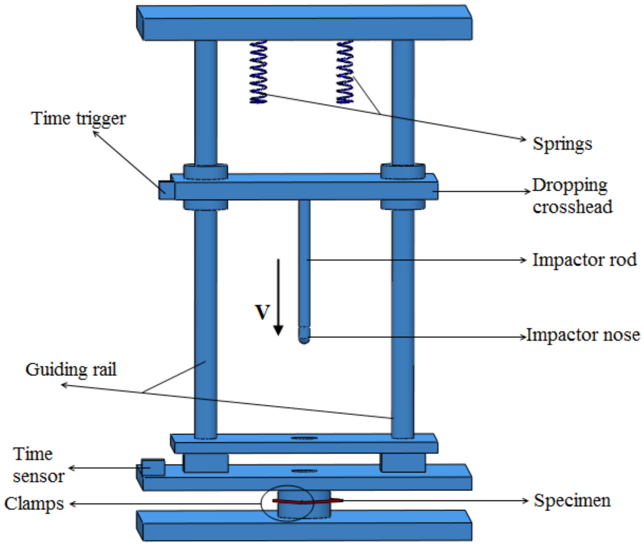

Figure 5.2 Schematic version of the tow velocity impact tester.

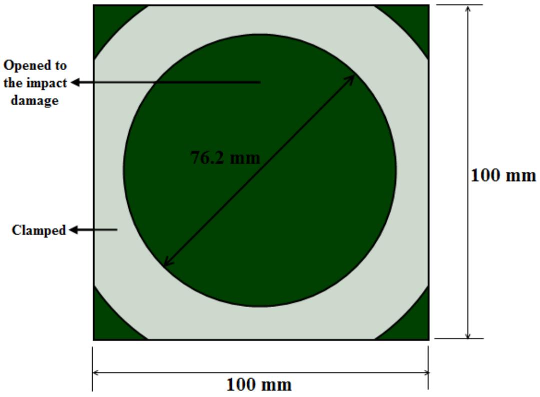

Figure 5.3 Clamped and unclamped faces of the specimen during impact.

The corresponding velocity history of the impactor could then be calculated from integrating the force history (after being divided by the mass of the impactor) and using the initial impact velocity.

Subsequently, the corresponding displacement history of the impactor could be calculated from integrating the velocity history. Based on the force and displacement histories, the force-displacement relation and the energy history of the impactor could be established.

Assuming the impactor was perfectly rigid and the energy loss on the contact-impact interface between the impactor and the specimen was negligible, the force-displacement relation of the impactor could be considered as the force-deflection curve of the composite specimen.

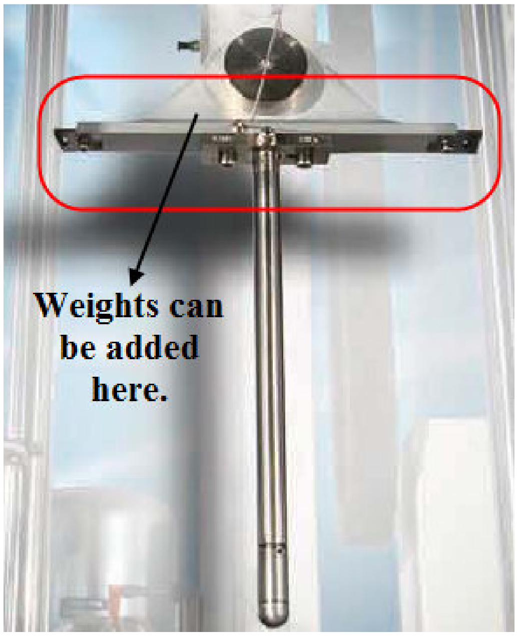

Figure 5.4 Weight adding unit.

And the kinetic energy of the impactor right before contact-impact took place, i.e. the *impact energy*, would be the energy transferred to the composite specimen. However, depending on the impact energy level and the type of specimen investigated, either a partial or the total amount of impact energy could be absorbed by the composite specimen in forms of damage, heat and others. (Liu, Raju & Dang, 2000)

5.3 Experimental Results

The impact tests are performed with Fractovis Plus tester at the temperature of 20 ^{o}C and at about 1 bar air pressure. In the test machine, the impactor with a hemispherical nose of 12.7 mm in diameter, and a force transducer with the capacity of 22.24 kN is used. The specimens are square with a 100 mm. in length per edge. The different impactor masses are used; 5.02 kg, 10.02 kg, 15.02 kg, 20.02 kg that impactor mass and the crosshead mass are included. The fiber orientation angle is the constant for all specimens as [0 I 30 I 60 I 90]s.

The experiments are performed in three main titles which consist of *constant impact energy, constant impactor mass, constant impact velocity*. The effect of mass, energy and velocity are aimed to find out. If a table was drawn to explain the experiment done, that was similar as the Table 5.1.

Table 5.1 Experiment specifications that objected to the specimens.

5 kg – 10 Joule (**2 m/s**)	**5 kg** – 20 Joule (2.828 m/s)	**5 kg** – 30 Joule (3.464 m/s)
10 kg – **2 m/s** (20 Joule)	**5 kg** – **40 Joule** (4 m/s)	**40 Joule** – 10 kg (2.828 m/s)
15 kg – **2 m/s** (30 Joule)	**40 Joule** – 20 kg (**2 m/s**)	**40 Joule** – 15 kg (2.309 m/s)

According to the Table 5.1, 9 main experiments have been performed. Each experiment had been repeated with three times and the mean values are selected to comment on them. The values are marked to represent *constant impactor mass, constant impact energy,* and *constant impact velocity* conditions for discussing the effect of impactor mass, velocity and energy more easily. After that point of this study, *constant (or equal) mass* represents the 5 kg impactor mass, *constant (or equal) energy* represents the 40 Joule impact energy, and *constant (or equal) impact velocity* represents the 2 m/s impactor velocity (in the gravity direction) in the diagrams, figures, tables and writings.

The mechanical properties of the specimen had been measured by Mehmet Aktaş in 2007 at Dokuz Eylül University with several experiments for different temperatures. The composite material that he used consists of the same materials that used while producing the specimens for this study.

Table 5.2 Mechanical properties of the specimen. (Aktaş, 2007)

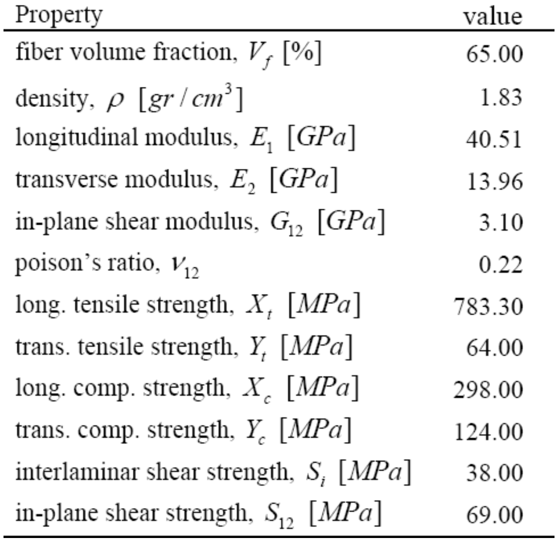

Property	value
fiber volume fraction, V_f [%]	65.00
density, ρ $[gr/cm^3]$	1.83
longitudinal modulus, E_1 $[GPa]$	40.51
transverse modulus, E_2 $[GPa]$	13.96
in-plane shear modulus, G_{12} $[GPa]$	3.10
poison's ratio, ν_{12}	0.22
long. tensile strength, X_t $[MPa]$	783.30
trans. tensile strength, Y_t $[MPa]$	64.00
long. comp. strength, X_c $[MPa]$	298.00
trans. comp. strength, Y_c $[MPa]$	124.00
interlaminar shear strength, S_i $[MPa]$	38.00
in-plane shear strength, S_{12} $[MPa]$	69.00

The mechanical properties of the composite specimen at room temperature have given in Table 5.2.

Before giving the graphs, explaining the three main deflection types are important. Impact damage occurs in three ways which are rebounding, penetration, and perforation. In the first two damage types, the specimen subjected to the impact damage reflects some of the energy from its body. This reflected energy spends on rebounding or negative penetration. In a perfect penetration, the impactor's velocity becomes zero and it knits with the specimen. In the rebounding condition, impactors's velocity becomes zero for a while, and then it accelerates in the opposite direction of the initial velocity vector. For the third case, the contact force increases to a critical value, then it reduces to a minimum value. At that moment, the specimen is perforated. In our experiments, the first two types of impact damage occurred.

To explain the damage types, contact force, deflection, impact velocity and impact energy versus time graphs are given in Figure 5.5.

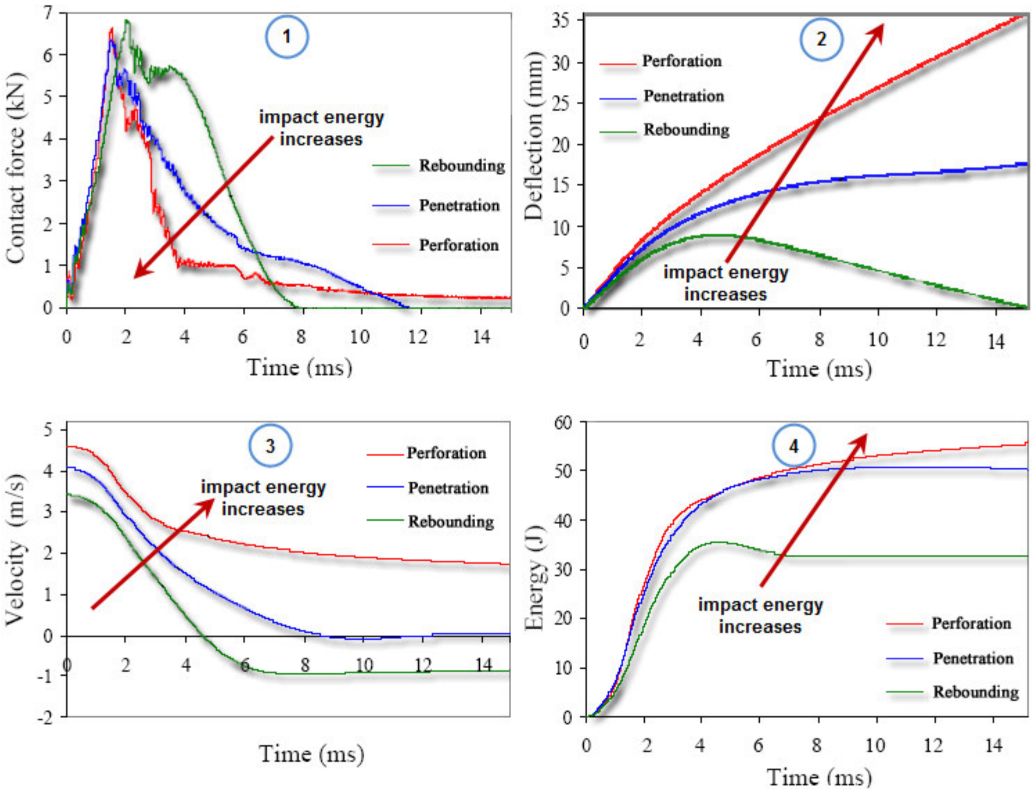

Figure 5.5 Three main impact damage types. (Aktaş, 2007)

It's clear from the Figure 5.5-1 that, with increasing impact energy, penetration goes to the perforation. In this Figure, the contact force never becomes zero due to the friction forces between the perforated area (hole) and the impactor. In Figure 5.5-2, the increase of deflection can be seen in three conditions. In rebounding condition, the final deflection is zero, because deflection graphs gives the displacement of the impactor; if the impactor is rebounded, the final deflection becomes zero (negative values are neglected for deflection). In penetration case, the deflection increases and then stops at a value. This value equals the distance from the impacted surface of the specimen where the impactors nose embedded. In perforation case, deflection increases to an infinitive value due to the smaller friction forces which is not enough to stop it. According to the Figure 5.5-3, it can be easily said that in rebounding situation, velocity takes a negative value. And for fully penetrated impactor, the final velocity becomes zero when the projectile is embedded to the specimen as shown in Figure 5.5-3. In the same Figure, it can also be seen that the velocity never resets to the zero, because there is no matrix or fiber to restrict the impactor. The greatest effect on penetration is impact energy level. But, for the equal mass with variable velocity, impact energy level affects less than the situation for equal velocity with variable mass. Hence, in constant impact energy condition, increasing the impactor mass inceases the penetration. After a critical value, penetration becomes perforation that will be discussed in further pages. It's clear from the Figure 5.5-4 that, rebounding occurs when the impact energy is greater than absorbed energy.

With the energy profiling method (EPM), penetration and perforation threshold values can be seen more clearly. In the Figure 5.6, AB region represents the rebounding case, BC represents the penetration case, and CD represents the perforation case. The diagram values are defined from the area under the contact force – deflection history as

$$E_i = \int_i F(\delta)\, d\delta \tag{5.1}$$

for any time. (E_i) represents the impact energy, and (E_a) represents the absorbed energy. P_n and P_r represents the penetration and perforation thresholds, respectively.

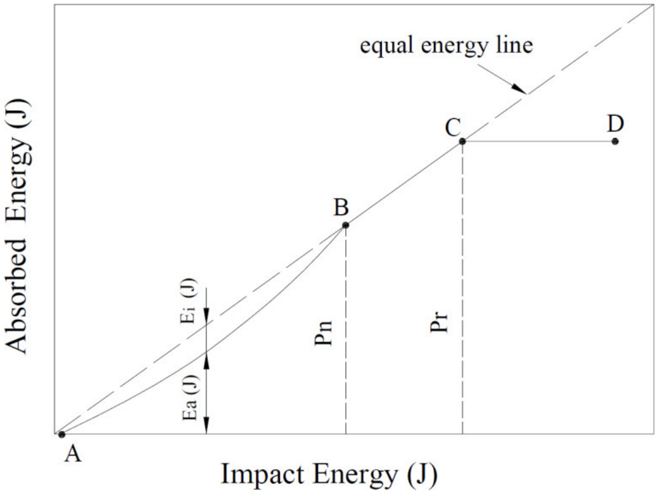

Figure 5.6 Three cases of damage types in EPM (Aktaş, 2007)

After the experiments, the energy profiling diagram in Figure 5.7 shows that the experiments are performed in the first case, rebounding. Only one type of test specimens have reached the penetration threshold. These are the specimens that 40 Joule impact energy has applied with 20 kg of mass at constant velocity.

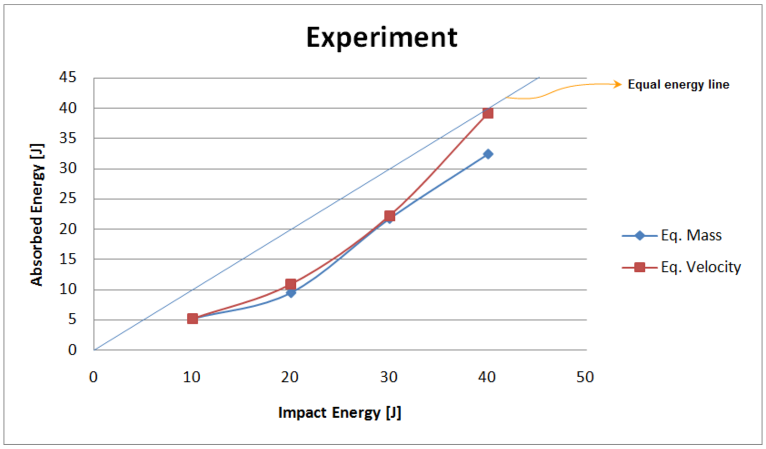

Figure 5.7 Energy Profiling Diagram of the experimental results.

In maximum penetrated specimens are the heaviest and have the maximum impact energy in the whole experiments. This shows that mass is the most effective parameter in penetration damage after impact energy. But on the other hand, the minimum mass specimens' absorbed energy curves are nearly congruent from 10 Joule to 30 Joule impact energy levels. In higher impact energy levels, the difference between eq. mass and eq. velocity curves increases rapidly. But in general, light and fast impactors rebound more than the heavy and slow impactors for constant energy.

5.3.1 Effects of Impact Energy, Impact Velocity, and Impactor Mass

The experimental results are classified in three main titles as shown in Figure 5.5. After that, the results are classified in two cases again for each effect. The first case is the effect of impact energy at constant impactor mass, and the second case is at constant impactor velocity.

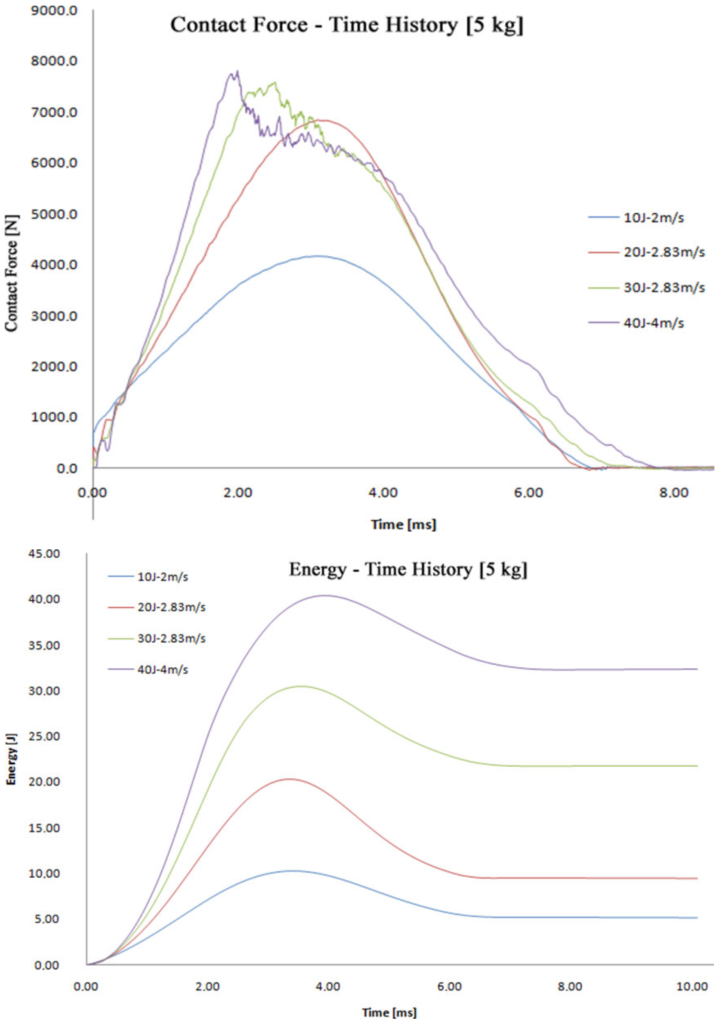

Figure 5.8 The contact force-time (top), and the energy-time (bottom) histories of experiments for [0°/30°/60°/90°]s at constant impactor mass.

In Figure 5.8, it’s clear to see that contact force increases with impact energy. Obliquely, delaminations increases with impact energy in part. The loading portions of the graphs are nearly same, but unloading portions are different due to the different damage mechanisms. At 10 and 20 Joule impact energy levels, the load and unloading portions of the curves are smoother. If these specimens are examined after the experiment, it would be seen that a very few (almost no) fiber fractures were occurred. The damage consists most of matrix damage. For 30 and 40 Joule impact energy levels, fiber fractures are significantly stands out.

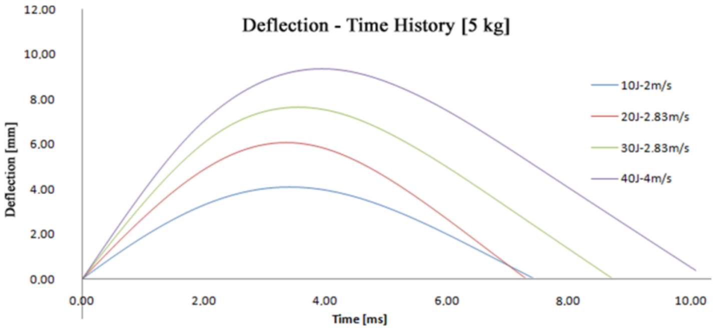

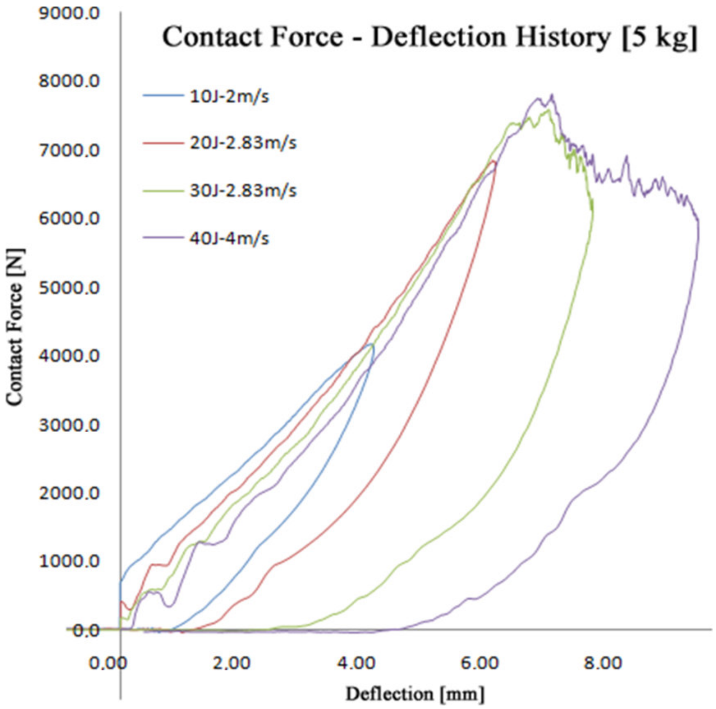

Figure 5.9 The deflection-time (top), and contact force-deflection (bottom) histories of experiments for [0°/30°/60°/90°]s at constant impactor mass.

In the Figure 5.9 (top), it’s seen that the most deflection occurred in the 40 Joule 5 kg specimens. This means that the 40 Joule 5 kg specimens absorbed the most energy in constant impactor mass case. And the most rebounding occurred in 20 Joule 5 kg specimens.

On the other hand, if the whole experiment data is analyzed together, the delamination threshold is obtained about 6.5 kN. This explains the rapid growth in delaminations as shown in Table 5.4. Comparing Table 5.4 and Figure 5.8 with this Contact Force-Time diagrams, the fiber fractures can be predicted at 30J and above.

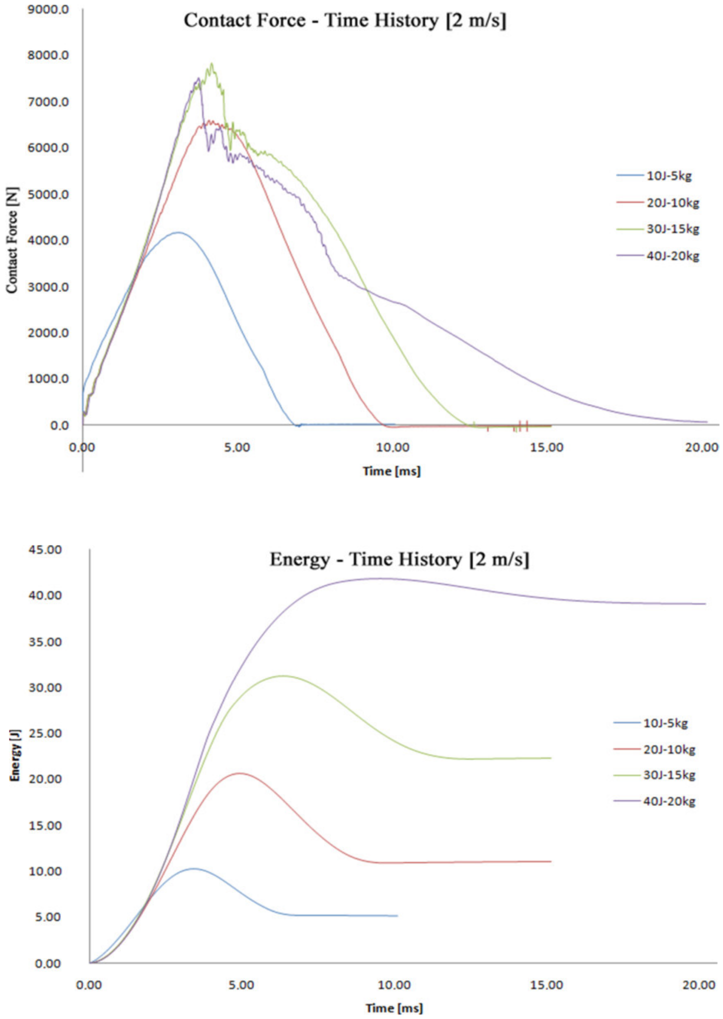

Figure 5.10 The contact force-time (top), and the energy-time (bottom) histories of experiments for [0°/30°/60°/90°]s at constant impact velocity.

At constant impactor velocity, energy level effects can be seen more clearly. In the Figure 5.10 (top) the significant rebounding portions can be seen. And the bottom of this figure, up to the 20 Joule impact energy, rebounded laminates reflect more energy than 40 Joule impacted specimens.

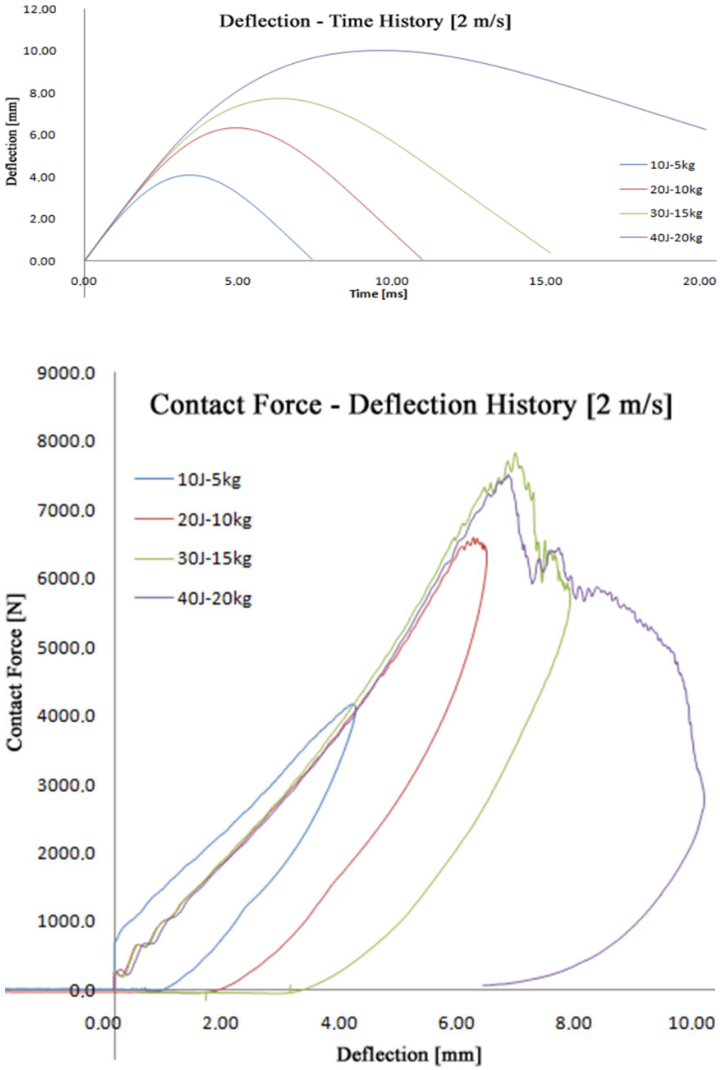

Figure 5.11 The deflection-time (top), and contact force-deflection (bottom) histories of experiments for [0°/30°/60°/90°]s at constant impactor velocity.

In Figure 5.11 (bottom), the absorbed energy can be calculated from the area under the curves. In this figure, 20 Joule – 10 kg specimens reflects most of the impact energy and damaged at a minimum level. But the 40 Joule – 20 kg specimens absorbed the most of the energy and damaged at a maximum level in the entire experiment. If the Figure 5.11 (top) is examined, the projectile embedded to the specimen in 30 and 40 Joule energy levels. The reflected energy cannot compensate the required energy to overcome the frictional forces. If it is assumed that, 40 Joule 20 kg specimens are fully penetrated, it would not be wrong. From the Figure 5.11, it's clear that absorbed energy increases with increasing the impact energy and the impactor mass together.

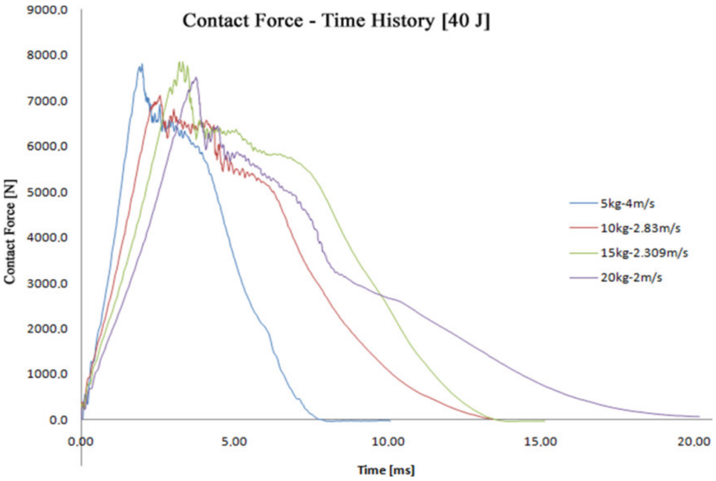

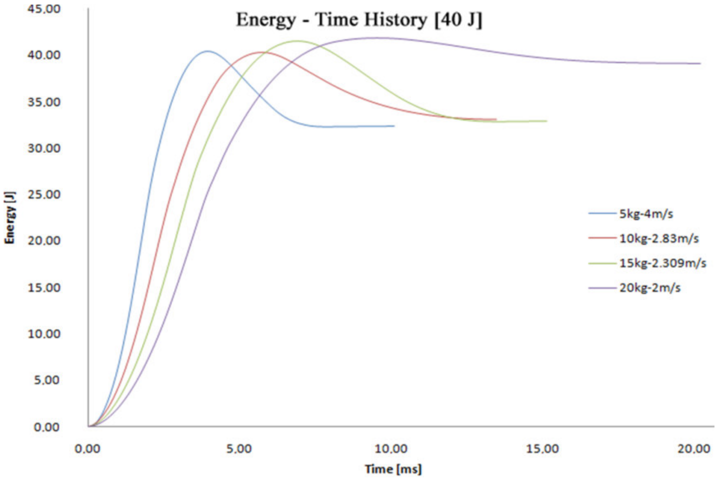

Figure 5.12 The contact force-time (top), and the energy-time (bottom) histories of experiments for [0°/30°/60°/90°]s at constant impact energy.

In Figure 5.12 (top), it's clearly seen that deformations commonly form of fiber fractures. And from the bottom of this figure, the absorbed energy increases with impactor mass.

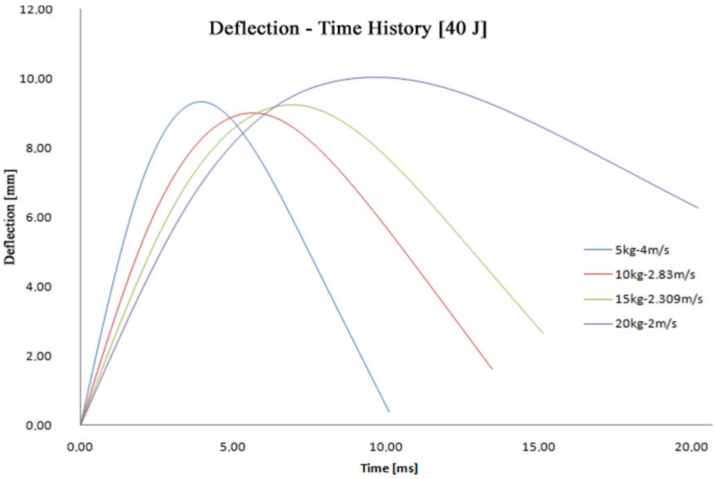

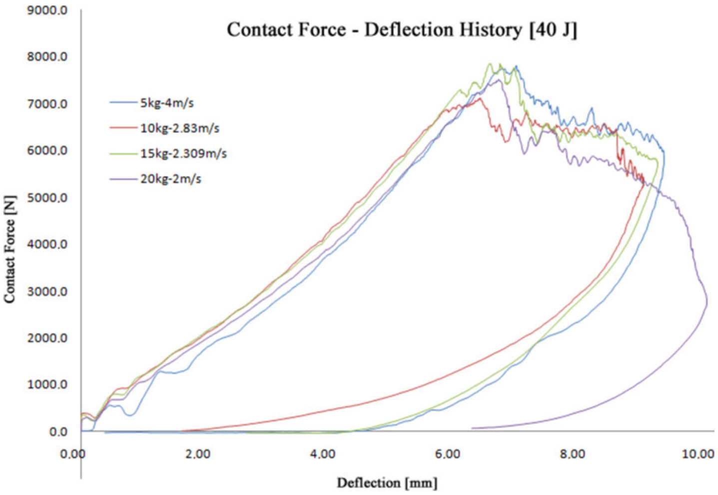

Figure 5.13 The deflection-time (top), and contact force-deflection (bottom) histories of experiments for [0°/30°/60°/90°]s at constant impact energy.

In Figure 5.13 (top), the impactor is embedded in all of the specimens. The reflected energy is unsuccessful beside the frictional forces. Also, the fiber fractures are at the highest values.

From the Figures 5.8-13, it can be seen that at constant impactor mass, increasing the energy increases the velocity as well, and increases the delamination. At constant impact energy, increasing the mass increases the damage area and absorbed energy. If 40 Joule – 20 kg specimen is chosen with 40 Joule – 5 kg specimens, the difference between damage mechanisms can be seen clearly. At the lighter impactor mass, the impact energy is spent mostly on delaminations; but for the heavier impactor mass, impact energy is spent mostly on fiber fracture. The reason of this difference depends on the difference of inertia forces between 5 and 20 kg impactors. Despite the velocity relations, stopping the lighter impactor is easier than the heavier. The high velocity and low mass impactors produce more dynamic vibrations (in frequency) than the heavier and low velocity impactors. These high frequency vibrations overcome the shear forces by breaking the molecular chain of the epoxy in each interface layer. This causes delaminations. But for the heavier impactor, smaller amount of energy is converted into vibrations than the lighter, hence the mass energy breaks the fibers which cause fiber damage.

To simplify understanding the impact event, only the peak values of the contact force, deflection of the specimen, and permanent deflections with absorbed energy are given in Table 5.3 and Figure 5.14.

Table 5.3 Maximum values of experimental results.

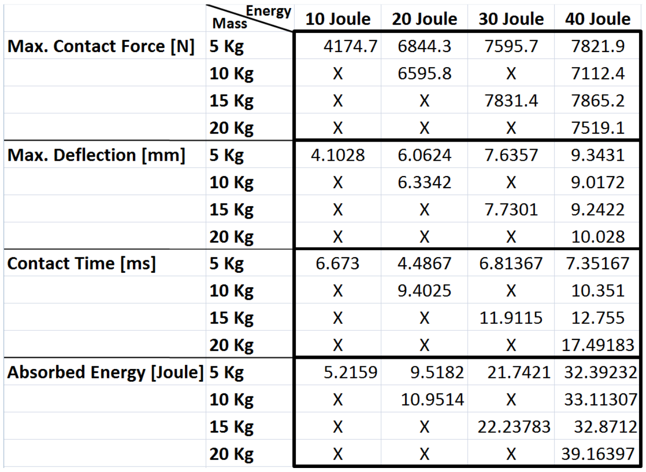

	Energy / Mass	10 Joule	20 Joule	30 Joule	40 Joule
Max. Contact Force [N]	**5 Kg**	4174.7	6844.3	7595.7	7821.9
	10 Kg	X	6595.8	X	7112.4
	15 Kg	X	X	7831.4	7865.2
	20 Kg	X	X	X	7519.1
Max. Deflection [mm]	**5 Kg**	4.1028	6.0624	7.6357	9.3431
	10 Kg	X	6.3342	X	9.0172
	15 Kg	X	X	7.7301	9.2422
	20 Kg	X	X	X	10.028
Contact Time [ms]	**5 Kg**	6.673	4.4867	6.81367	7.35167
	10 Kg	X	9.4025	X	10.351
	15 Kg	X	X	11.9115	12.755
	20 Kg	X	X	X	17.49183
Absorbed Energy [Joule]	**5 Kg**	5.2159	9.5182	21.7421	32.39232
	10 Kg	X	10.9514	X	33.11307
	15 Kg	X	X	22.23783	32.8712
	20 Kg	X	X	X	39.16397

In Table 5.3, the difference of contact times between 40 Joule 5 kg and 20 kg specimens shows the energy transfer speeds. Transferring the energy in a very short time corresponds to the magnitude of the power of impact. High-powered impacts cause more delaminations and higher frequency vibrations than low-powered impacts at the same impact energy.

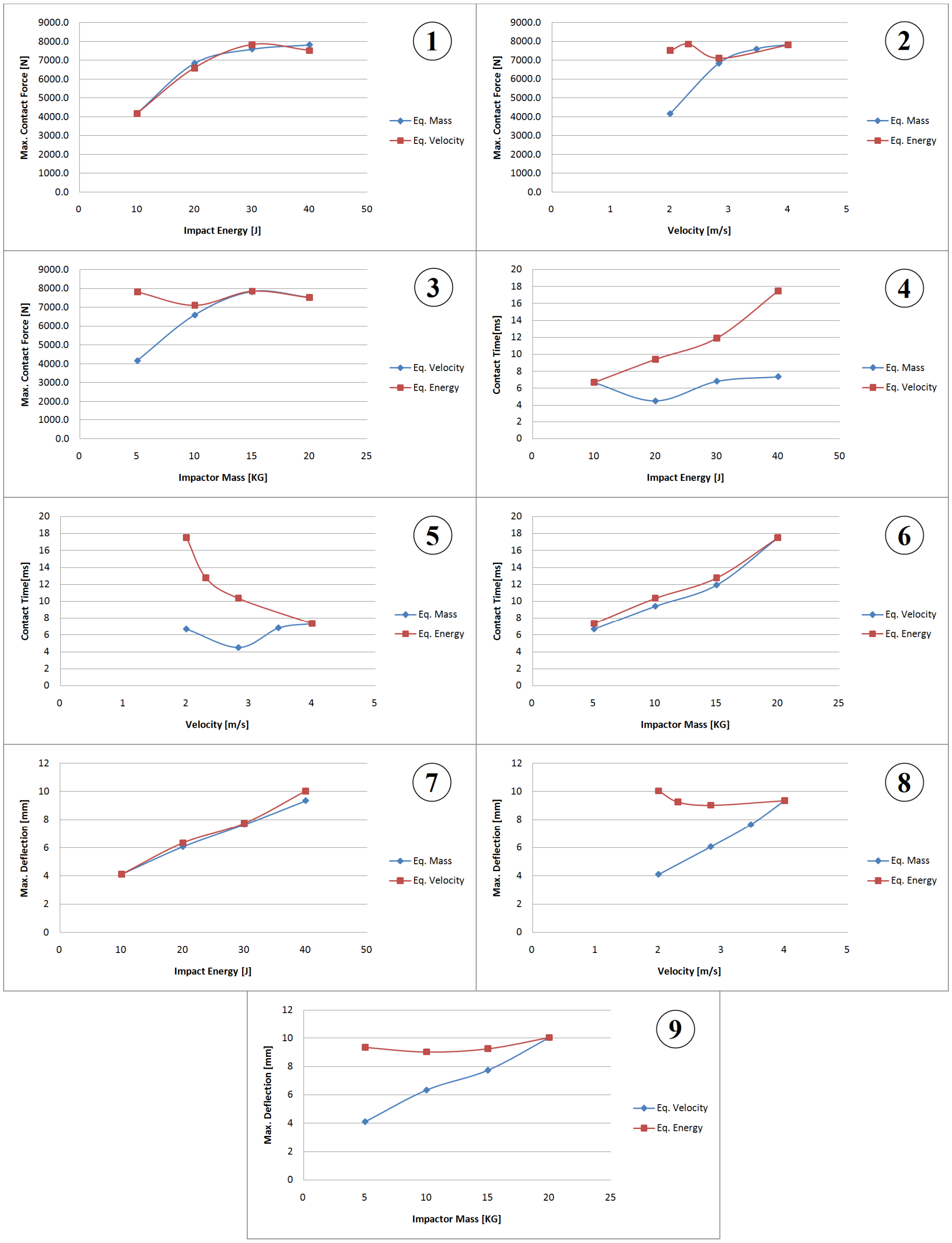

Figure 5.14 Multiple graphs generated from the max values of experim. results for [0°/30°/60°/90°]s.

The impact power of 40 Joule (39.164 Joule absorbed) 20 kg specimen is 2.239 mWatt, and the impact power of 40 Joule (32.392 Joule absorbed) 5 kg specimen is 4.406 mWatt. If the 40 Joule 5-10-15 kg specimens are compared, the impact power corresponds to 4.406 mWatt, 3.199mWatt, 2.577 mWatt, respectively. These results shows that, impact power increases the delaminations and reduces indention (deflection) and fiber fractures at constant energy. The contact time-velocity diagram can be seen from the Figure 5.14-(5). The other diagrams are showed in Figure 5.14-(1-12) to understand the impact event easier. After these explanations, it can be said that increasing the impact energy (providing to increase impactor mass) increases the indention of the impactor. And again, increasing the impact energy increases delaminations after the threshold value of contact force for delamination initiation.

5.3.2 Damage Areas

To discuss the damage areas, giving the damage mechanisms is important. When a foreign object impacts on a composite laminate, several damage modes occurs. These are matrix cracks, delaminations and the fiber breakage. One or more damage modes can occur alone or together according to the impact parameters. The fiber breakage will be discussed with delaminations and matrix cracks that are illustrated together in the Figure 5.15. In this study, at the higher impact energy levels and impactor mass, splitting between fiber and matrix with fiber fractures are dominant damage modes around the impact point. Also, the delaminations are greater because of debonding delaminations at the bottom interface layer.

In the Figure 5.15, the bottom layer delamination is debonding, the 30° laid “H” is the splitting border. This border can be seen only you examine the specimen carefully. It’s angle is 30°, because the most of the inner delaminations throughout the laminate is between 30° and 60° plies. Then, the dominant breaked fibers are at 30° angle.

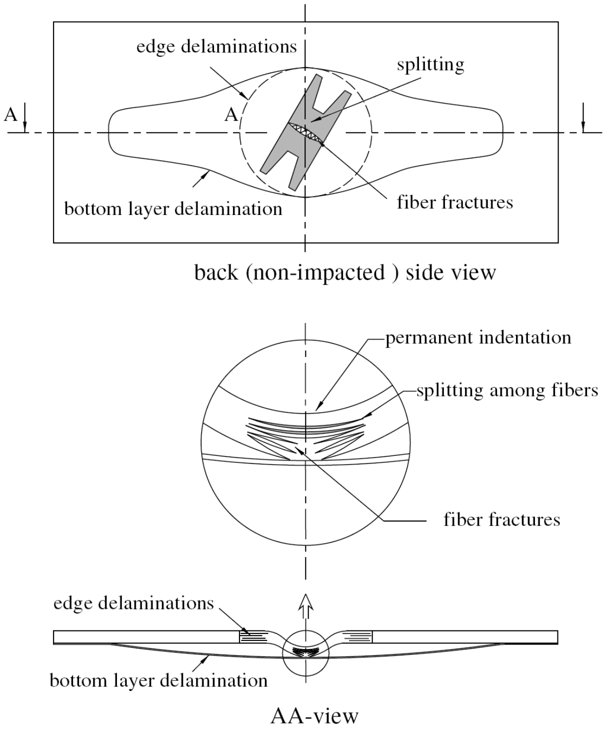

Figure 5.15 Delamination modes (Re-produced from the original at Aktaş, 2007)

In Figure 5.16, the splitting border, fiber fracture and bottom layer delamination are shown clearly. It's important to see that, there is no delamination after bottom layer delamination.

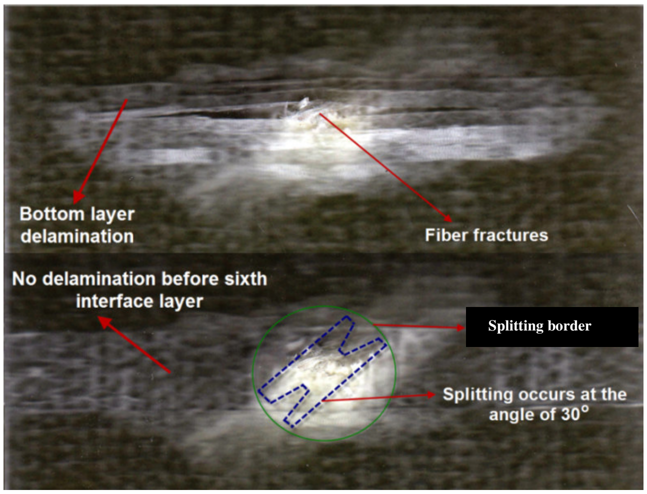

Figure 5.16 The impact damage from the back face that 5kg impactor mass applied with 40 Joule impact energy to the specimen for [0°/30°/60°/90°]s.

In Figure 5.17, matrix cracks and edge delaminations of a 40 Joule 5 kg laminate at impacted and non-impacted faces. The images processed with a computer code to see through the laminate more easily. In Figure 5.19, at the middle and right corner of the non-impacted face with 40 Joule, 2 m/s specimen is the best result to see the fiber damages inside the laminate. The 30° ply is seen before 0° the bottom layer clearly.

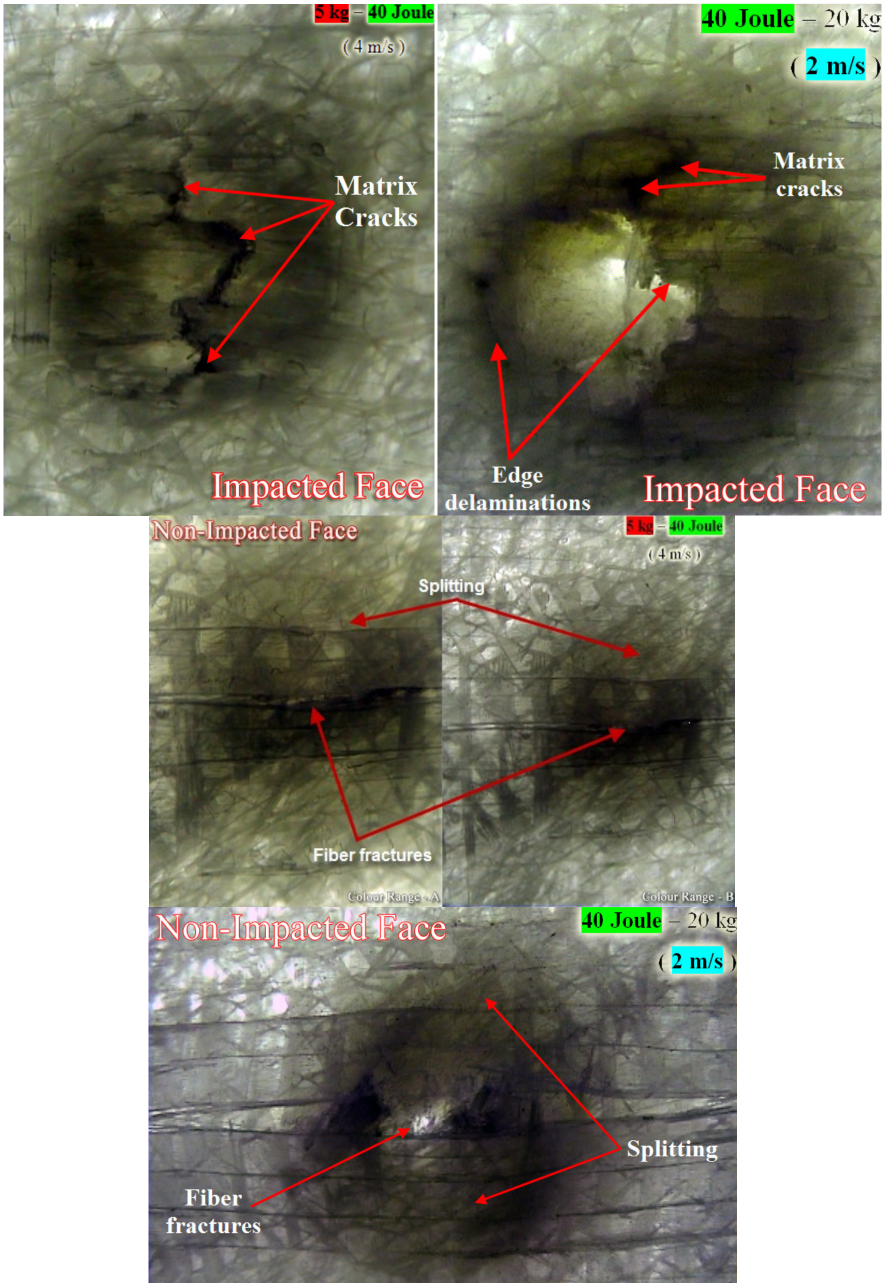

Figure 5.17 The impact damage on the impacted face that 5kg impactor mass applied with 40 Joule impact energy to the specimen for [0°/30°/60°/90°]s.

In the Figure 5.17, the difference between the same impact energy with 5 and 20 kg impactor mass specimens. The difference of indention of the laminates is clear as discussed before.

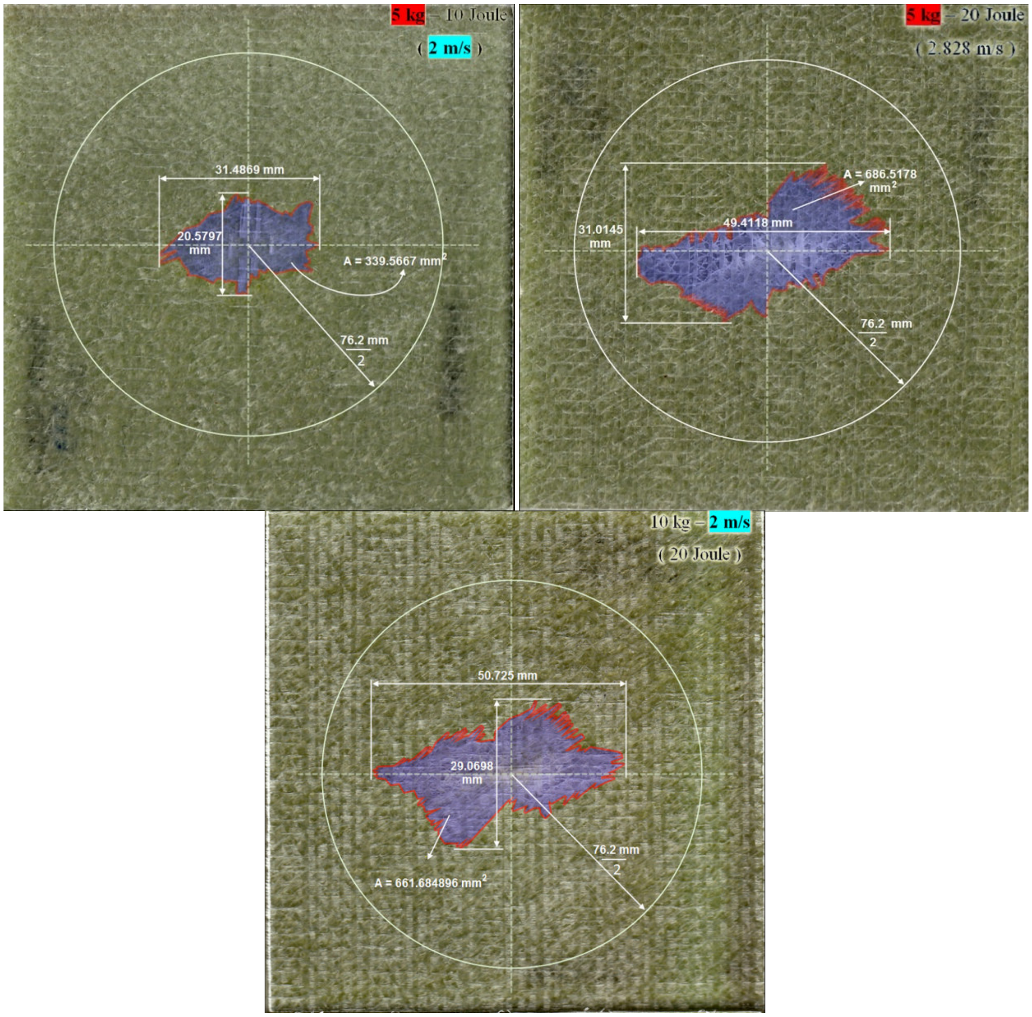

Figure 5.18 Delamination area and delamination length of the specimens for [0°/30°/60°/90°]s.

In the Figures 5.18-19, the seen delamination areas are highlighted and mirrored (to correct the direction of orientation angles) to examine delaminations easier. It was said the "seen" delamination areas. Because these areas are mostly composed of the delaminations at the bottom interface layers (between the last two layers). The highlighted areas are calculated with a 2D graphical computer code and scaled to the full-sized real specimen for accuracy. The delamination lengths are also calculated. The white circles are balanced to the clamps of the impact tester machine.

The center point of this circle is coincident with impact point.

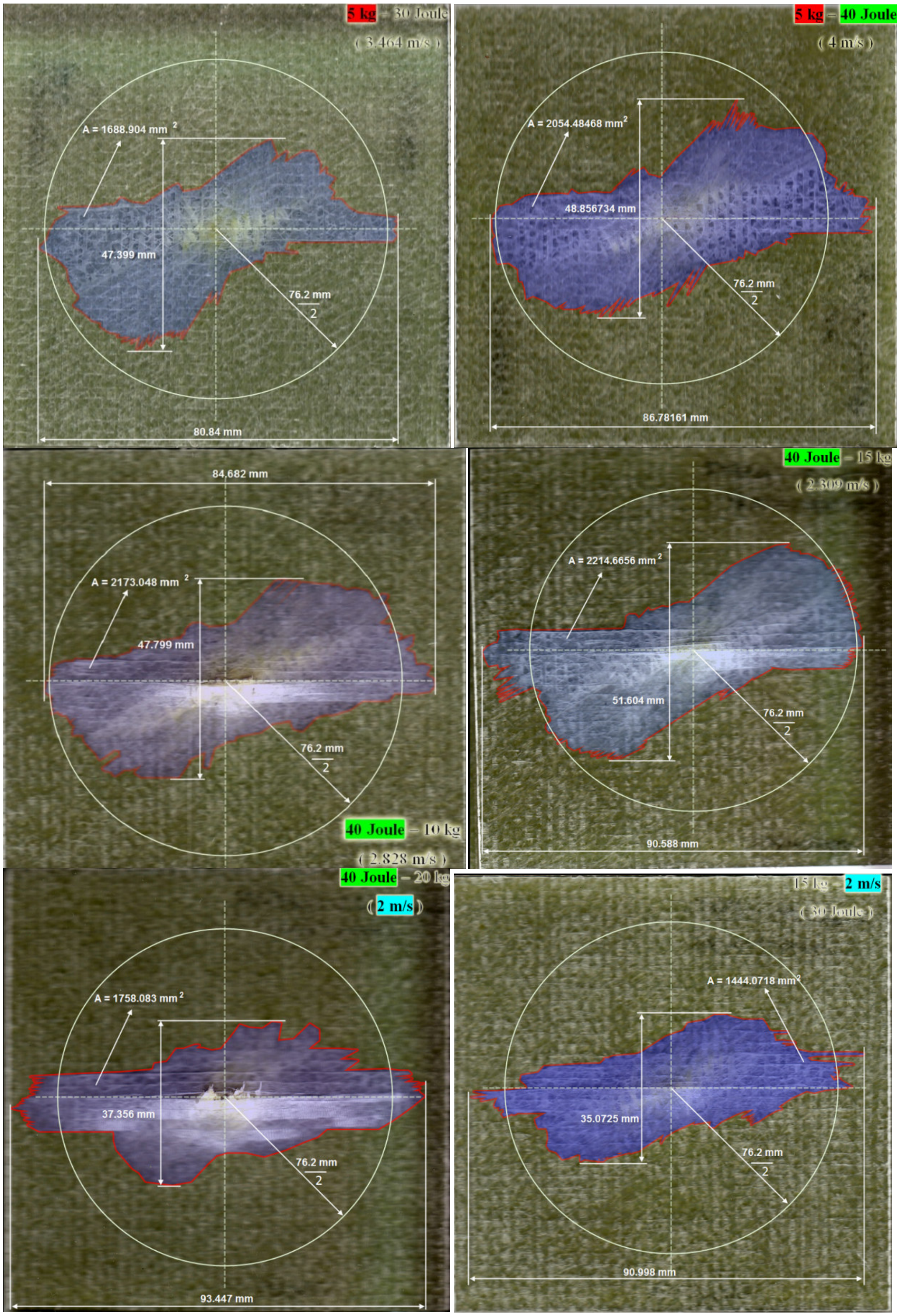

Figure 5.19 Delamination area and delamination length of the specimens for [0°/30°/60°/90°]s.

In the Figure 5.19, the 40 Joule and 5 kg specimen can be seen that the entire delamination through thickness is the greatest in all specimens, due to the high frequency vibrations as discussed before. The overlapped delamination areas can also be seen from Table 5.4. In this table, the mentioned area as overlapped, is the *seen* delamination areas from the non-impacted face of the laminate.

Table 5.4 Overlapped delamination areas for 9 specimens.

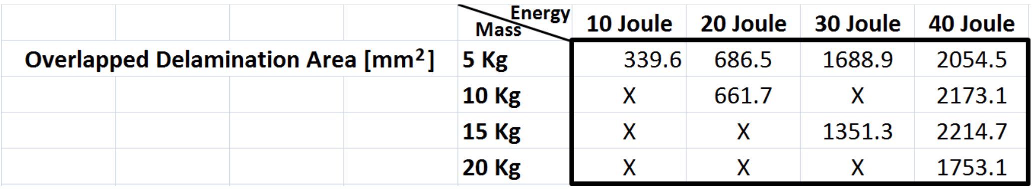

	Energy / Mass	10 Joule	20 Joule	30 Joule	40 Joule
Overlapped Delamination Area [mm^2]	**5 Kg**	339.6	686.5	1688.9	2054.5
	10 Kg	X	661.7	X	2173.1
	15 Kg	X	X	1351.3	2214.7
	20 Kg	X	X	X	1753.1

5.4 Finite Element Code and Numerical Results

3D impact code is used as a solver in numerical analysis. It is a ForTran-based transient dynamic finite element analysis code which calculates stresses and contact forces of the composite plates during impact along with a failure analysis for predicting the threshold of impact damage and initiation of delaminations. It was used for numerical simulation. The dynamic stress analysis was carried out using an eight-point brick element and the direct Gauss quadrature integration scheme is used through the element thickness to account for the change in material properties from layer to layer within the element. The Newmark scheme (Bethe & Wilson, 1976) is adopted to perform time integration from step to step. A contact law incorporated with the Newton–Raphson method is applied to calculate the contact force during impact. The analysis of transient contact forces between the impactor and the composite, transient stresses in the laminates is based on three-dimensional linear elasticity with the consideration that, in each layer, the materials are homogeneous and orthotropic. The computer code allows evaluation of delamination areas by means of suitable stress analysis and damage criteria. The finite element mesh used for the calculations is presented in Figure 5.20.

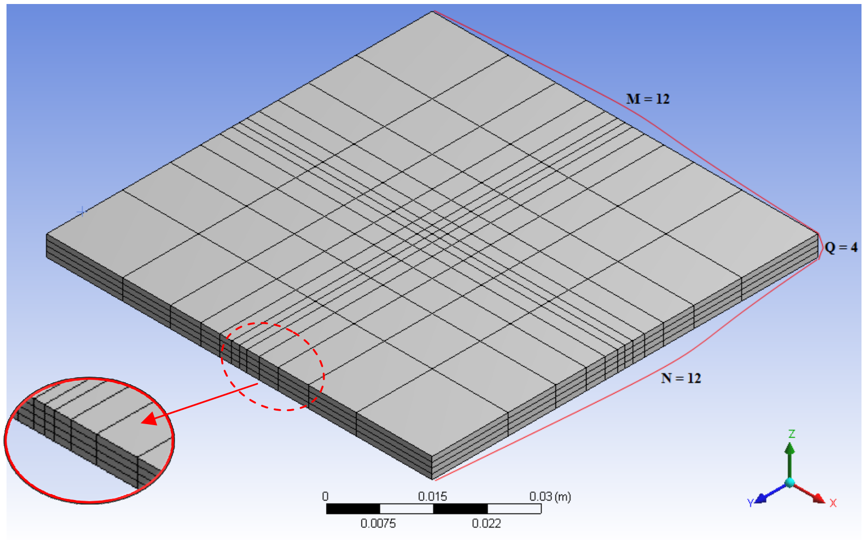

Figure 5.20 The finite element model of the impact code.

The laminate is divided into a total of N x M x Q elements as shown in Figure 5.20. The overall shape is a square which has the dimension of 76.2 mm per edge. A total of four elements are used through the thickness of the laminate. The mesh is made progressively coarser towards the boundary. Choi and Chang (1992) evaluated the effect of finite element mesh size on the stability of the numerical prediction based on the model. They found that the proposed failure analysis does not require the use of an extensive fine mesh. Therefore, a regular mesh of 576 $[N(=12)xM(=12)xQ(=4)]$ is used in the numerical calculations for generating the results. (Aslan, Karakuzu, Okutan, 2002)

The comparison between experimental study and the numerical study has given in different forms such as diagrams, tables and illustrations. In the contract force-time histories, it can be seen that the peak levels differ from the experiment. The main reason for this situation is the fiber fracture criterion which is not included in the finite element code that is used in this study. To overcome this problem, the curves in the entire contact force-time diagrams are fit to the sixth degree polynomials and the maximum value of these polynomials are taken to process for each impact parameter.

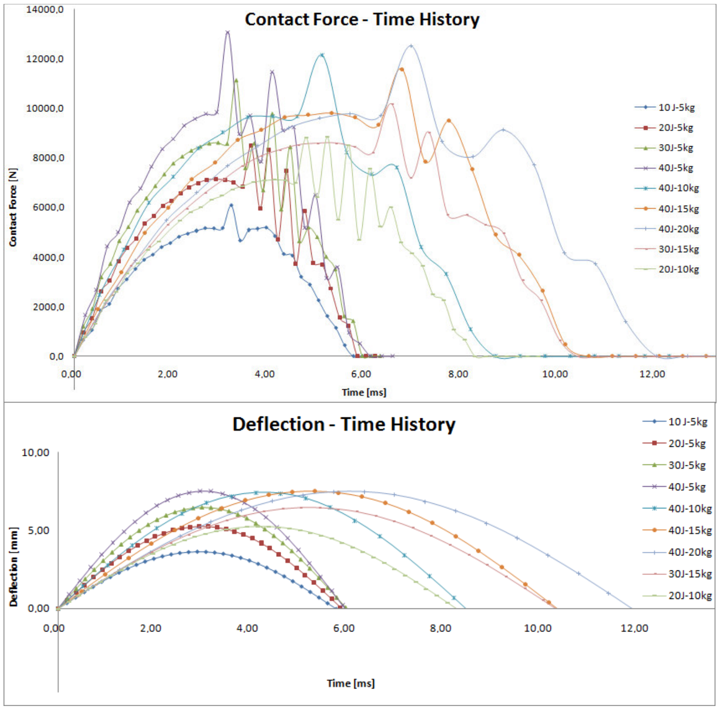

Figure 5.21 The contact force-time (top), and the deflection-time (bottom) histories of numerical solutions for constant impactor mass.

In Figure 5.21, the contact force-time and deflection-time diagrams are shown for all impact parameters. In this figure (bottom), deflection increases by increasing the impactor mass and energy. It's important to see that, the contact time is longer at heavy impactors. The contact time and the impact power depend mostly on impactor mass. The low-powered energy transfers cause lower frequencies, and result in higher penetration damages. Nevertheless, the high-powered energy transfers generate higher frequencies, and result in greater delamination areas.

In Figure 5.22, the 5 kg- 20 Joule parameter, numerical curve is the closer curve to the experimental curve in the whole experiments. If this specimenis examined, it can be seen (in Table 5.3) that this specimen has the lowest absorbed energy rate with 48% in entire study. Also, the most rebounding rate is occurred for this specimen. The most important result is, only a few fiber fracture was occurred in this specimen. This is the evident for why the numerical curve is so close to the experimental curve: fiber fracture criterion. The contact force-time histories of specimens for equal mass, equal energy, and the equal velocity impact parameters, are given in three groups in Figure 5.22, 5.23, and 5.24, respectively.

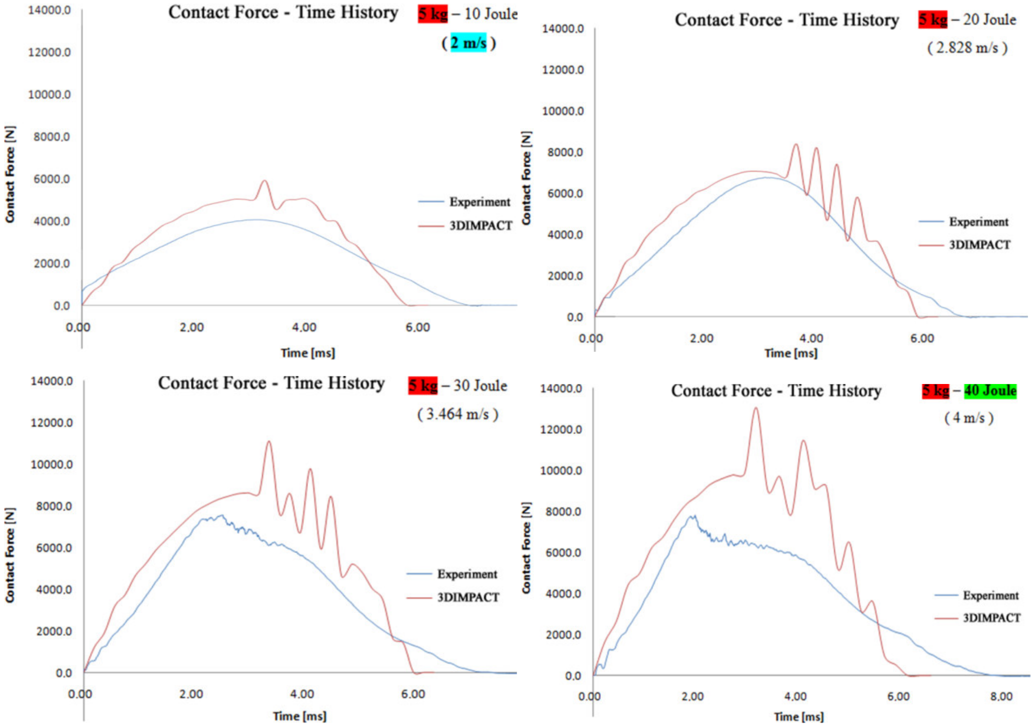

Figure 5.22 The contact force-time overlaid histories for equal impactor mass for [0°/30°/60°/90°]s.

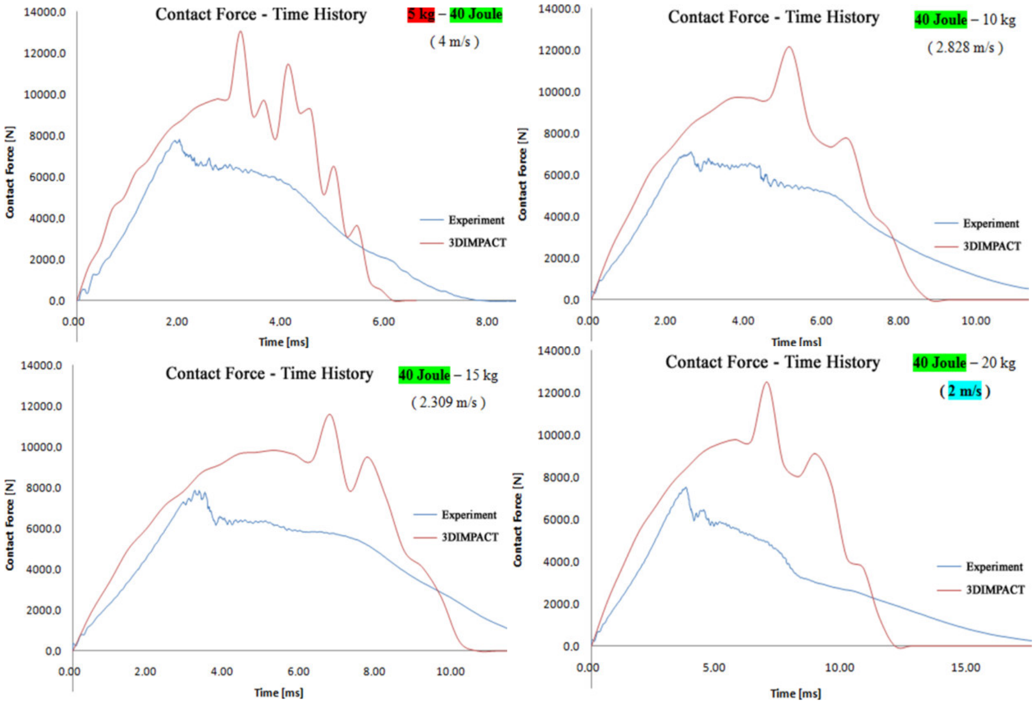

Figure 5.23 The contact force-time overlaid histories for equal impact energy for [0°/30°/60°/90°]s.

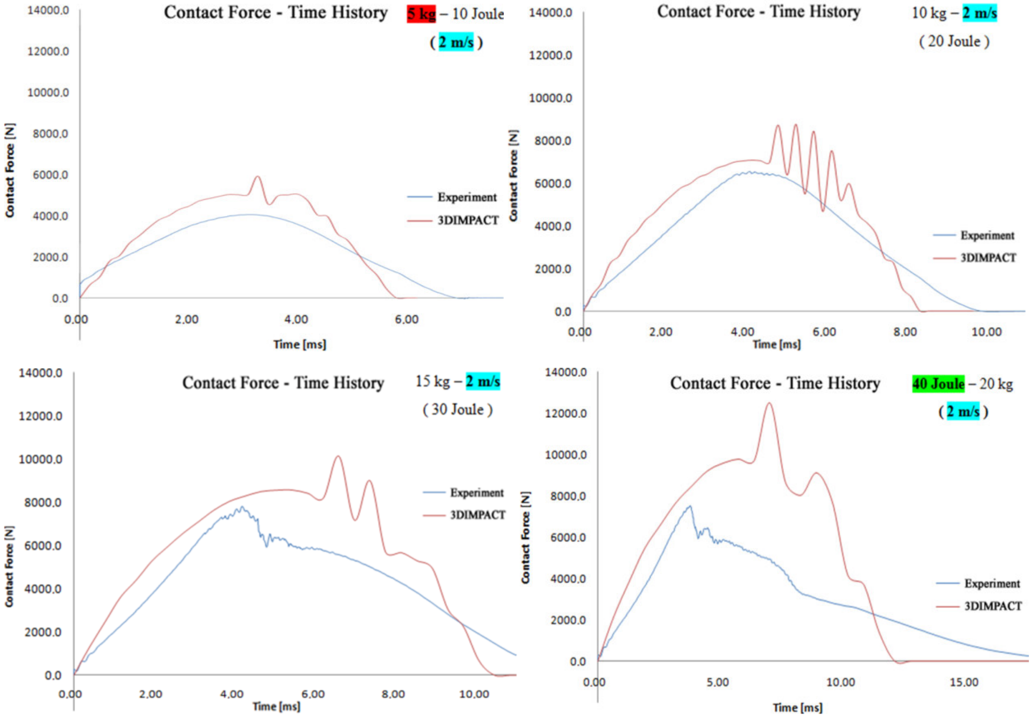

Figure 5.24 The contact force-time overlaid histories for equal impact velocity for [0°/30°/60°/90°]s.

To compare the maximum values of both experimental and numerical results are given in Table 5.5. (To have smoothest graph, the curves are emulated to the sixth degree polynomials and the peak values of these polynomials are taken as maximum)

Table 5.5 Maximum values for contact force, deflection & contact time for all orientation sequences.

		Max. Contact Force [N]				Max. Deflection [mm]				Contact Time [ms]			
	Mass Energy	5 Kg	10 Kg	15 Kg	20 Kg	5 Kg	10 Kg	15 Kg	20 Kg	5 Kg	10 Kg	15 Kg	20 Kg
[0 | 15 | -15 | 90]s	10 Joule	5830	X	X	X	3,692	X	X	X	5,633	X	X	X
	20 Joule	8400	8000	X	X	5,25	5,272	X	X	5,632	8,058	X	X
	30 Joule	9200	X	9100	X	6,523	X	6,53	X	5,787	X	10,28	X
	40 Joule	10420	10400	10420	10100	7,561	7,555	7,528	7,548	5,833	8,214	10,15	11,7
[0 | 30 | 60 | 90]s	10 Joule	4910 [4174,7]	X	X	X	3,629 [4,103]	X	X	X	5,48 [6,673]	X	X	X
(Experimental results are replaced between "[" and "]" symbols)	20 Joule	7200 [6844,3]	7400 [6595,8]	X	X	5,198 [6,062]	5,238 [6,334]	X	X	5,77 [4,487]	8,12 [9,403]	X	X
	30 Joule	9200 [7595,7]	X	8800 [7831,4]	X	6,434 [7,636]	X	6,455 [7,730]	X	5,77 [6,681]	X	10,03 [11,912]	X
	40 Joule	10180 [7821,9]	10000 [7112,4]	10200 [7865,2]	10150 [7519,1]	7,471 [9,343]	7,428 [9,017]	7,498 [9,242]	7,464 [10,028]	5,771 [7,732]	8,192 [10,351]	10,15 [12,755]	11,4 [17,492]
[0 | 30 | -30 | 90]s	10 Joule	5420	X	X	X	3,629	X	X	X	5,605	X	X	X
	20 Joule	8150	7820	X	X	5,189	5,228	X	X	5,632	8,058	X	X
	30 Joule	9250	X	10200	X	6,458	X	6,417	X	5,787	X	9,722	X
	40 Joule	10820	10600	10500	11200	7,508	7,432	7,445	7,463	5,75	8,214	10,15	11,37
[0 | 60 | -60 | 90]s	10 Joule	5800	X	X	X	3,657	X	X	X	5,633	X	X	X
	20 Joule	8300	7800	X	X	5,149	5,174	X	X	5,58	8,058	X	X
	30 Joule	9000	X	9900	X	6,382	X	6,394	X	5,657	X	9,722	X
	40 Joule	11200	10500	11100	11000	7,435	7,389	7,403	7,43	5,734	7,857	9,8	11,37
[0 | 75 | -75 | 90]s	10 Joule	5900	X	X	X	3,565	X	X	X	5,471	X	X	X
	20 Joule	7800	8000	X	X	5,124	5,104	X	X	5,605	7,84	X	X
	30 Joule	9200	X	10050	X	6,32	X	6,299	X	5,605	X	9,722	X
	40 Joule	11200	10800	11300	11200	7,346	7,316	7,32	7,346	5,58	7,857	9,8	11,05

In addition to this, the maximum values are given not only for the [0°/30°/60°/90°]s orientation sequences, but also for the [0°/15°/-15°/90°]s, [0°/30°/-30°/90°]s, [0°/60°/-60°/90°]s, [0°/75°/-75°/90°]s orientation sequences to add the study flexibility to comment on it.

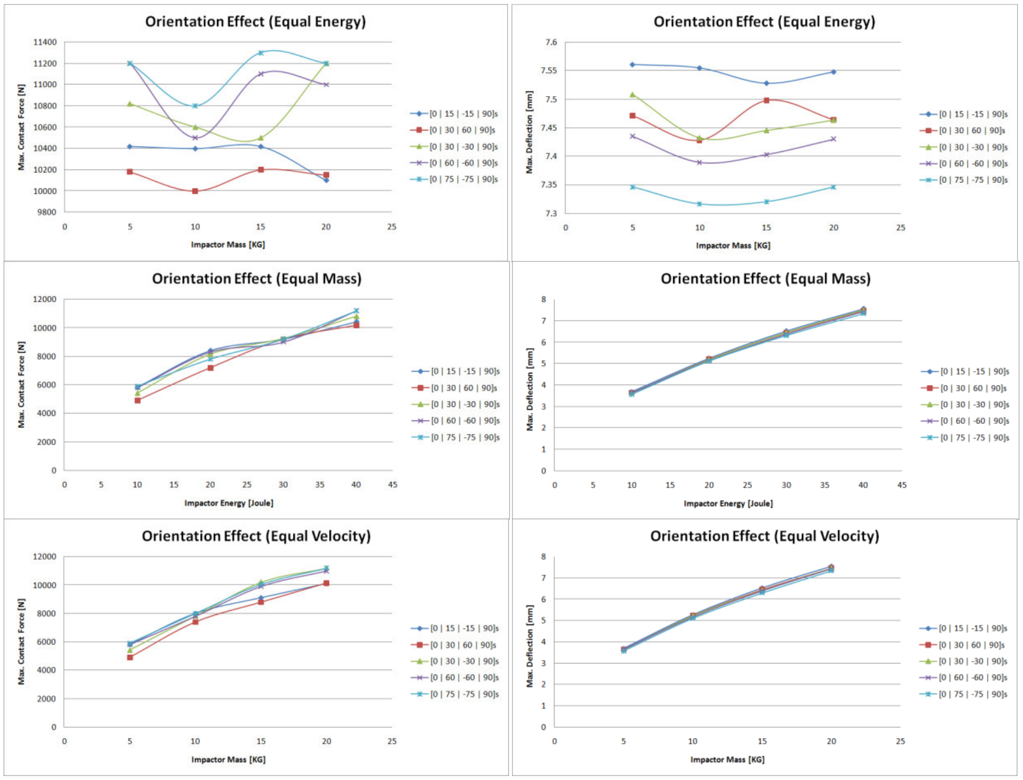

Figure 5.25 Orientation effect at equal impact energy, impactor mass and velocity.

The effect of orientation angle is grouped into three cases as done before; equal impact energy, equal impactor mass and equal velocity. In Figure 5.25, it's clear to see that, maximum contact force increases with increasing the difference between orientation angles for equal energy (40 Joule). And it can be seen that, the maximum contact force and deflection increases with impact energy. This increment is independent from the orientation angle.

To examine the effect of thickness, Figures 5.26-28 are given. From the diagrams in Figure 5.26, it can be seen that increasing the laminate thickness increases the maximum contact force.

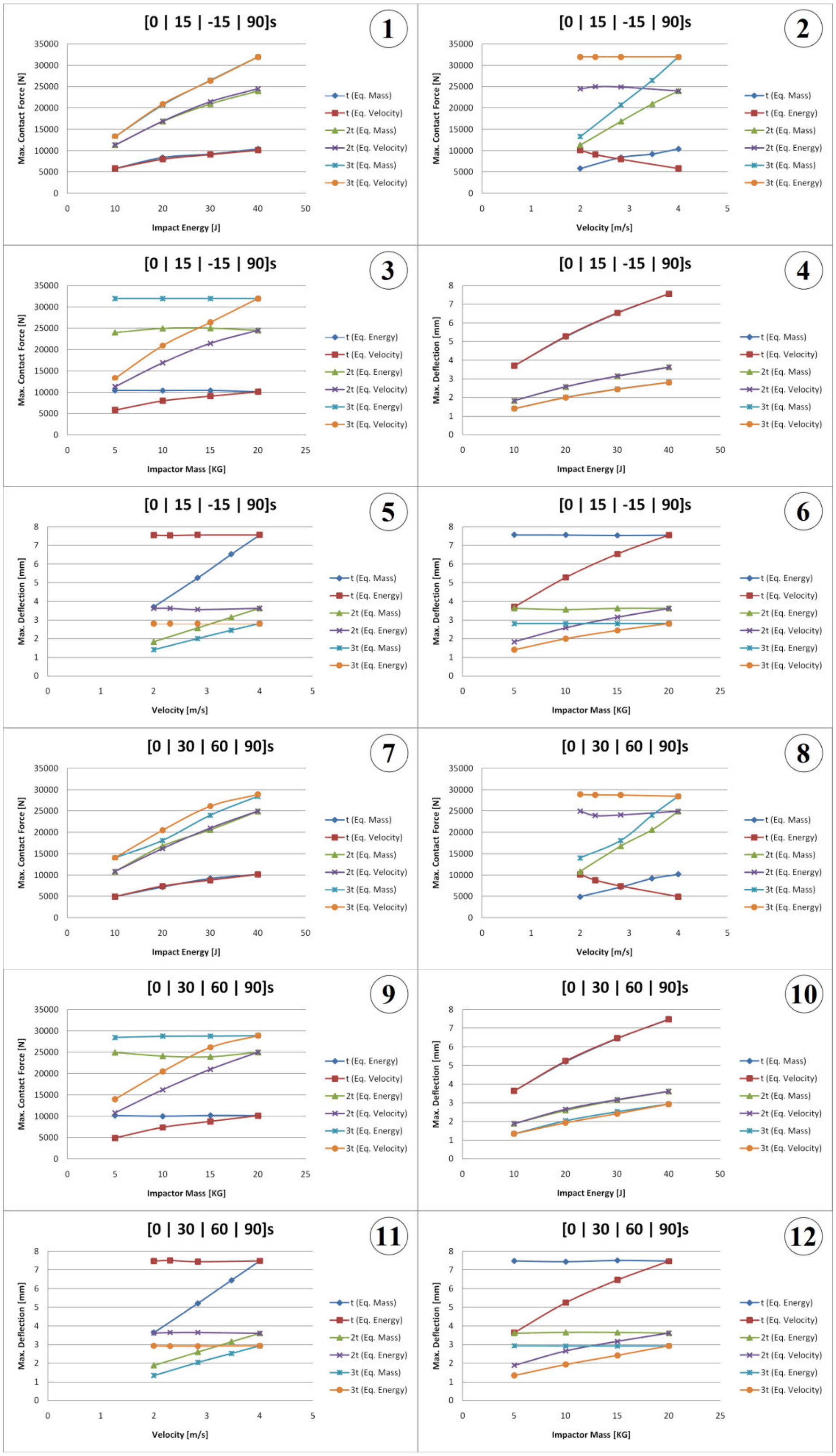

Figure 5.26 Multiple diagrams for thickness effect on max. contact force & deflection.

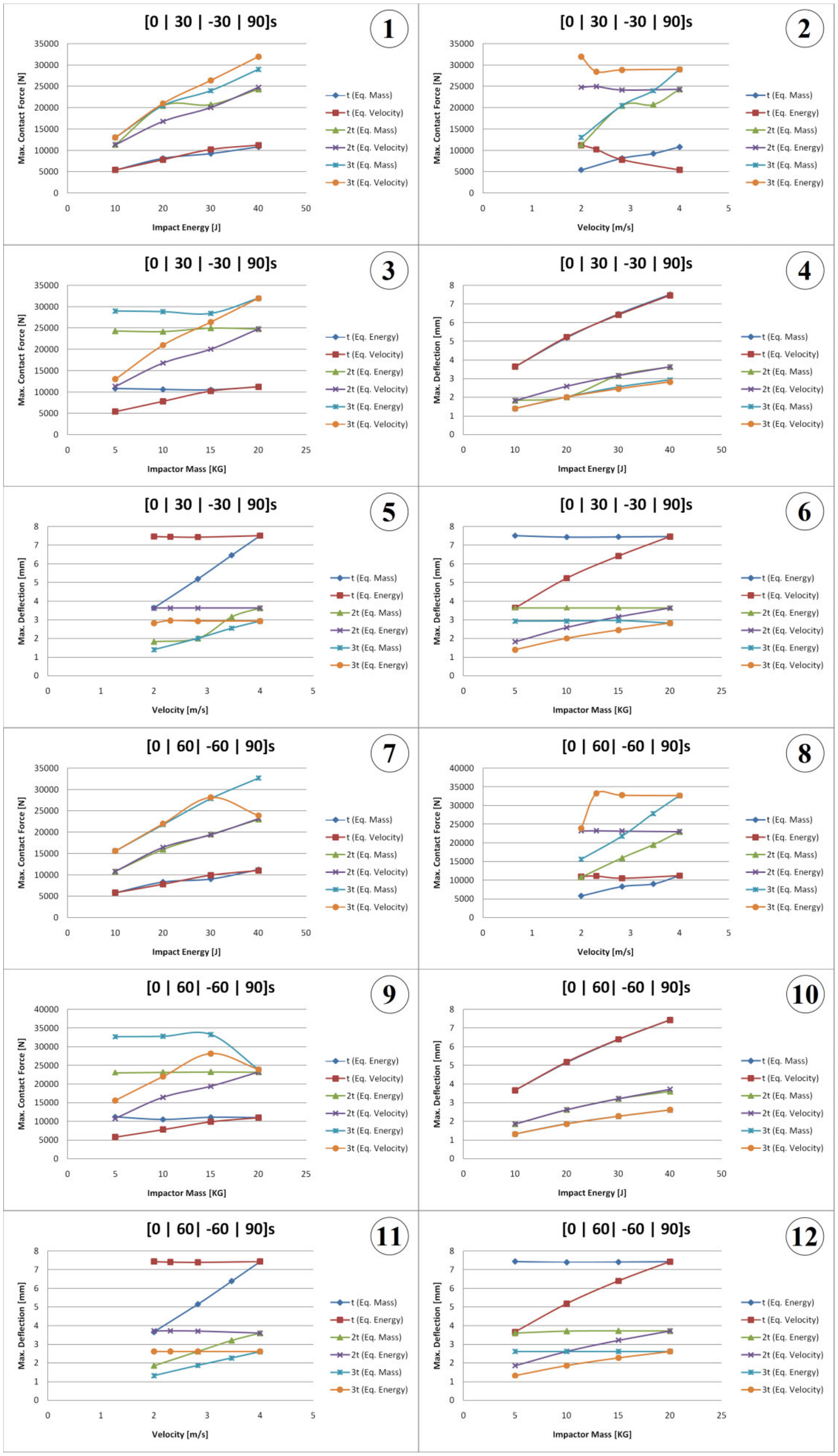

Figure 5.27 Multiple diagrams for thickness effect on max. contact force & deflection.

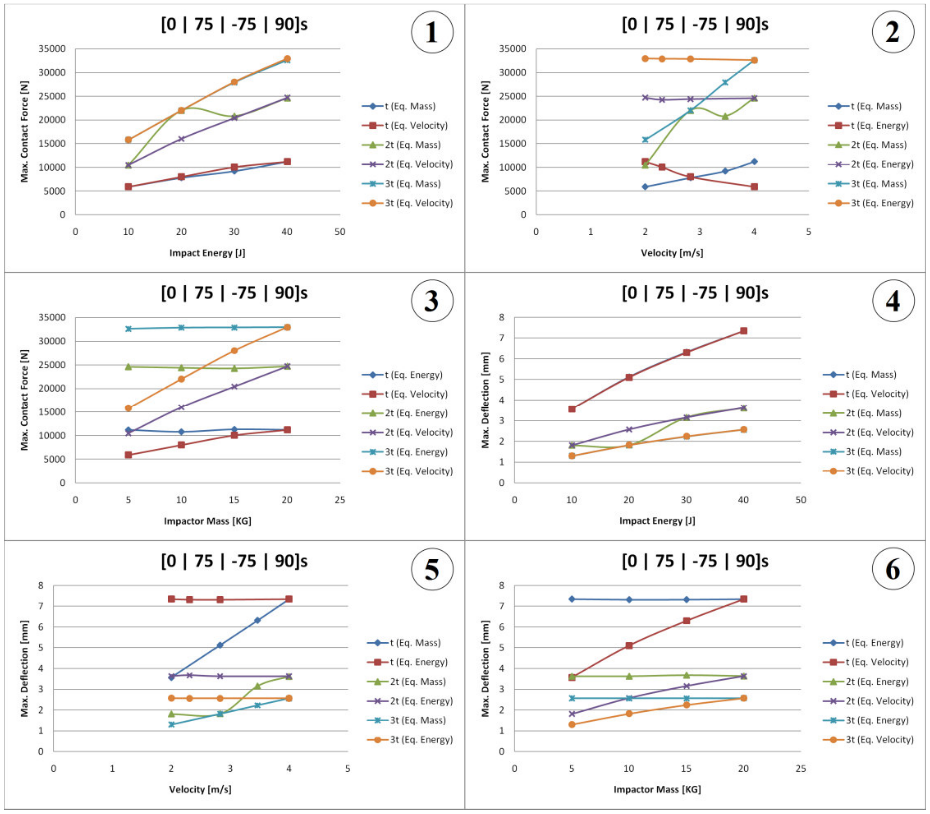

Figure 5.28 Multiple diagrams for thickness effect on max. contact force & deflection.

The maximum values of the numerical results are given in Table 5.6 to compare. In this table, it’s easy to say that, maximum contact force increases with increasing the difference between the two adjacent plies for constant impact energy in the thickness factor of T. The reason for this increment is the higher bending stiffness. For constant impact energy, the negative orientation angles are more effective than the positive ones.

After these diagrams, the computed delamination areas are compared with the experimental results in Figures 5.31-35 in detailed. The notations that used in the diagrams and illustrations are explained in Figure 5.29. The per unit area of the points in delamination illustration is calculated and projected in to the Figure 5.30. At the end, the overlapped delamination areas can be seen from the Table 5.7.

Table 5.6 Maximum values of contact force & deflection results from numerical solutions for different orientation sequences.

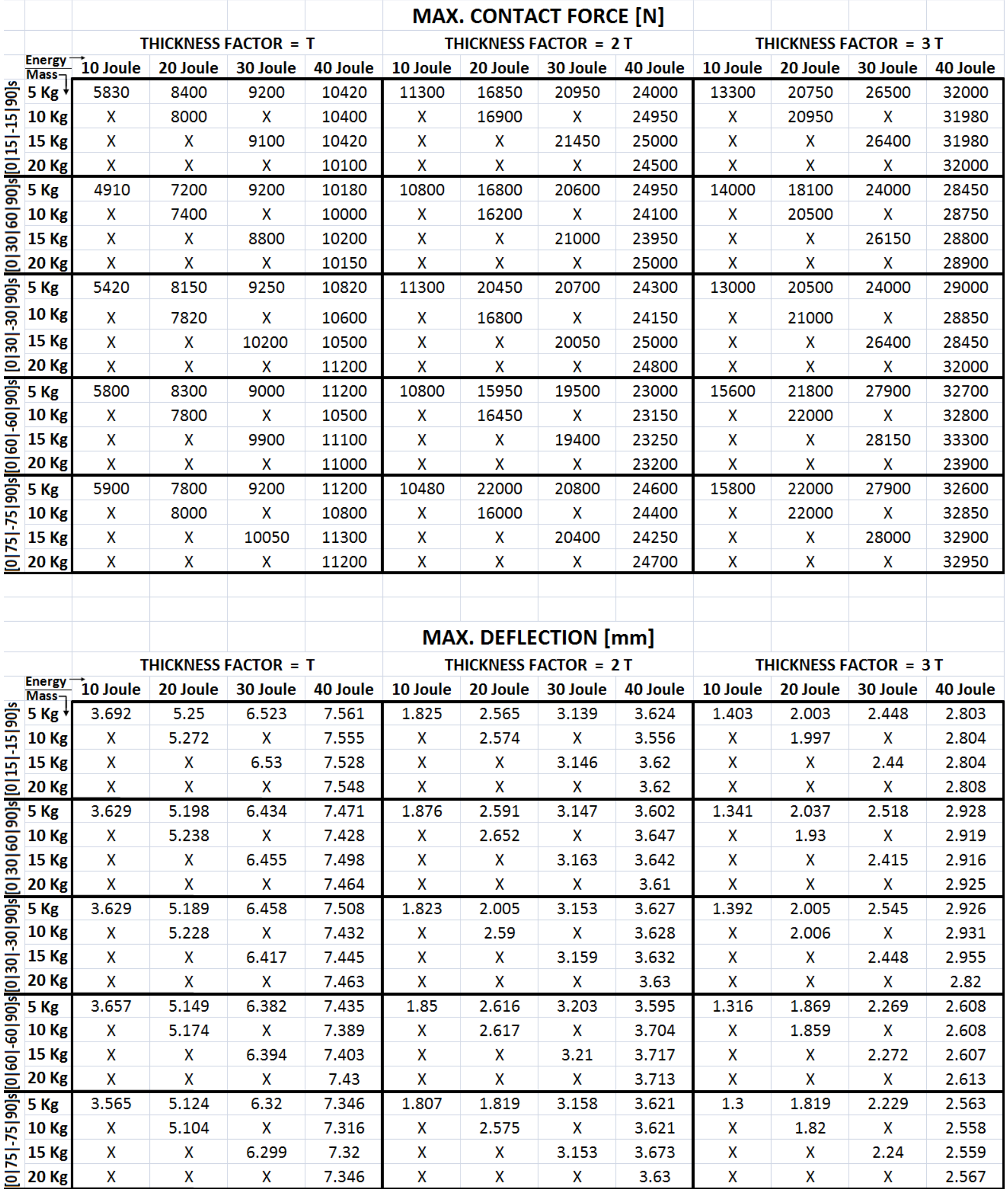

MAX. CONTACT FORCE [N]

		THICKNESS FACTOR = T				THICKNESS FACTOR = 2 T				THICKNESS FACTOR = 3 T			
	Energy → / Mass ↓	10 Joule	20 Joule	30 Joule	40 Joule	10 Joule	20 Joule	30 Joule	40 Joule	10 Joule	20 Joule	30 Joule	40 Joule
[0|15|-15|90]s	5 Kg	5830	8400	9200	10420	11300	16850	20950	24000	13300	20750	26500	32000
	10 Kg	X	8000	X	10400	X	16900	X	24950	X	20950	X	31980
	15 Kg	X	X	9100	10420	X	X	21450	25000	X	X	26400	31980
	20 Kg	X	X	X	10100	X	X	X	24500	X	X	X	32000
[0|30|60|90]s	5 Kg	4910	7200	9200	10180	10800	16800	20600	24950	14000	18100	24000	28450
	10 Kg	X	7400	X	10000	X	16200	X	24100	X	20500	X	28750
	15 Kg	X	X	8800	10200	X	X	21000	23950	X	X	26150	28800
	20 Kg	X	X	X	10150	X	X	X	25000	X	X	X	28900
[0|30|-30|90]s	5 Kg	5420	8150	9250	10820	11300	20450	20700	24300	13000	20500	24000	29000
	10 Kg	X	7820	X	10600	X	16800	X	24150	X	21000	X	28850
	15 Kg	X	X	10200	10500	X	X	20050	25000	X	X	26400	28450
	20 Kg	X	X	X	11200	X	X	X	24800	X	X	X	32000
[0|60|-60|90]s	5 Kg	5800	8300	9000	11200	10800	15950	19500	23000	15600	21800	27900	32700
	10 Kg	X	7800	X	10500	X	16450	X	23150	X	22000	X	32800
	15 Kg	X	X	9900	11100	X	X	19400	23250	X	X	28150	33300
	20 Kg	X	X	X	11000	X	X	X	23200	X	X	X	23900
[0|75|-75|90]s	5 Kg	5900	7800	9200	11200	10480	22000	20800	24600	15800	22000	27900	32600
	10 Kg	X	8000	X	10800	X	16000	X	24400	X	22000	X	32850
	15 Kg	X	X	10050	11300	X	X	20400	24250	X	X	28000	32900
	20 Kg	X	X	X	11200	X	X	X	24700	X	X	X	32950

MAX. DEFLECTION [mm]

		THICKNESS FACTOR = T				THICKNESS FACTOR = 2 T				THICKNESS FACTOR = 3 T			
	Energy → / Mass ↓	10 Joule	20 Joule	30 Joule	40 Joule	10 Joule	20 Joule	30 Joule	40 Joule	10 Joule	20 Joule	30 Joule	40 Joule
[0|15|-15|90]s	5 Kg	3.692	5.25	6.523	7.561	1.825	2.565	3.139	3.624	1.403	2.003	2.448	2.803
	10 Kg	X	5.272	X	7.555	X	2.574	X	3.556	X	1.997	X	2.804
	15 Kg	X	X	6.53	7.528	X	X	3.146	3.62	X	X	2.44	2.804
	20 Kg	X	X	X	7.548	X	X	X	3.62	X	X	X	2.808
[0|30|60|90]s	5 Kg	3.629	5.198	6.434	7.471	1.876	2.591	3.147	3.602	1.341	2.037	2.518	2.928
	10 Kg	X	5.238	X	7.428	X	2.652	X	3.647	X	1.93	X	2.919
	15 Kg	X	X	6.455	7.498	X	X	3.163	3.642	X	X	2.415	2.916
	20 Kg	X	X	X	7.464	X	X	X	3.61	X	X	X	2.925
[0|30|-30|90]s	5 Kg	3.629	5.189	6.458	7.508	1.823	2.005	3.153	3.627	1.392	2.005	2.545	2.926
	10 Kg	X	5.228	X	7.432	X	2.59	X	3.628	X	2.006	X	2.931
	15 Kg	X	X	6.417	7.445	X	X	3.159	3.632	X	X	2.448	2.955
	20 Kg	X	X	X	7.463	X	X	X	3.63	X	X	X	2.82
[0|60|-60|90]s	5 Kg	3.657	5.149	6.382	7.435	1.85	2.616	3.203	3.595	1.316	1.869	2.269	2.608
	10 Kg	X	5.174	X	7.389	X	2.617	X	3.704	X	1.859	X	2.608
	15 Kg	X	X	6.394	7.403	X	X	3.21	3.717	X	X	2.272	2.607
	20 Kg	X	X	X	7.43	X	X	X	3.713	X	X	X	2.613
[0|75|-75|90]s	5 Kg	3.565	5.124	6.32	7.346	1.807	1.819	3.158	3.621	1.3	1.819	2.229	2.563
	10 Kg	X	5.104	X	7.316	X	2.575	X	3.621	X	1.82	X	2.558
	15 Kg	X	X	6.299	7.32	X	X	3.153	3.673	X	X	2.24	2.559
	20 Kg	X	X	X	7.346	X	X	X	3.63	X	X	X	2.567

According to Table 5.6, maximum contact force are reached at [0/75/-75/90]s stacking sequence. Because the maximum bending stiffness occurs in this sequence. And it can be clearly seen that, deflection decreases by increasing laminate thickness due to the higher bending stiffness, again.

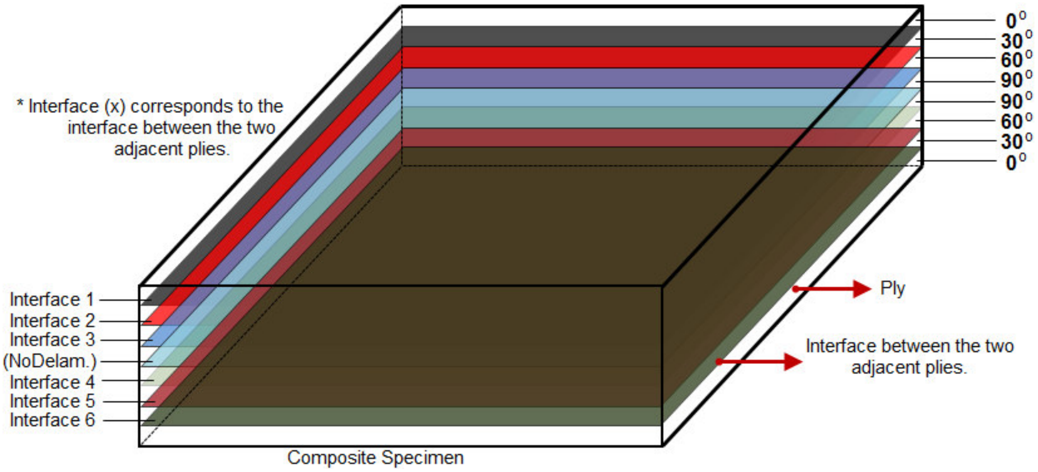

Figure 5.29 Notations for damage illustrations.

In Figure 5.29, there is no delamination at the symmetry plane. Because the difference between orientation angles at that plane is equal to zero.

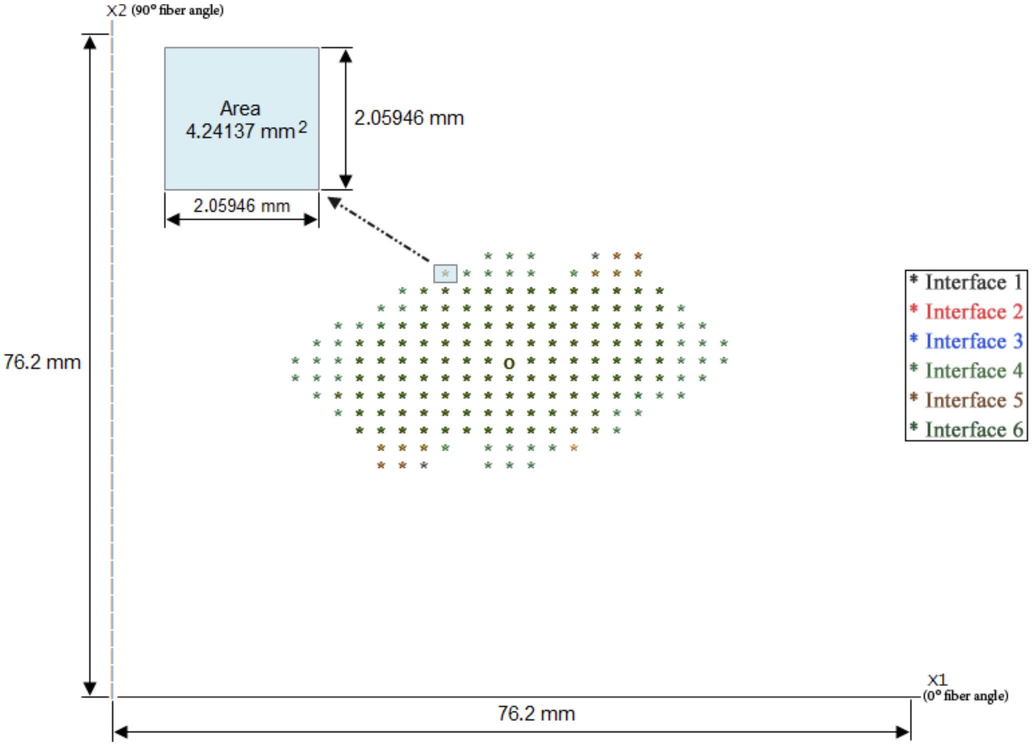

Figure 5.30 Measure & scales of the damage illustrations.

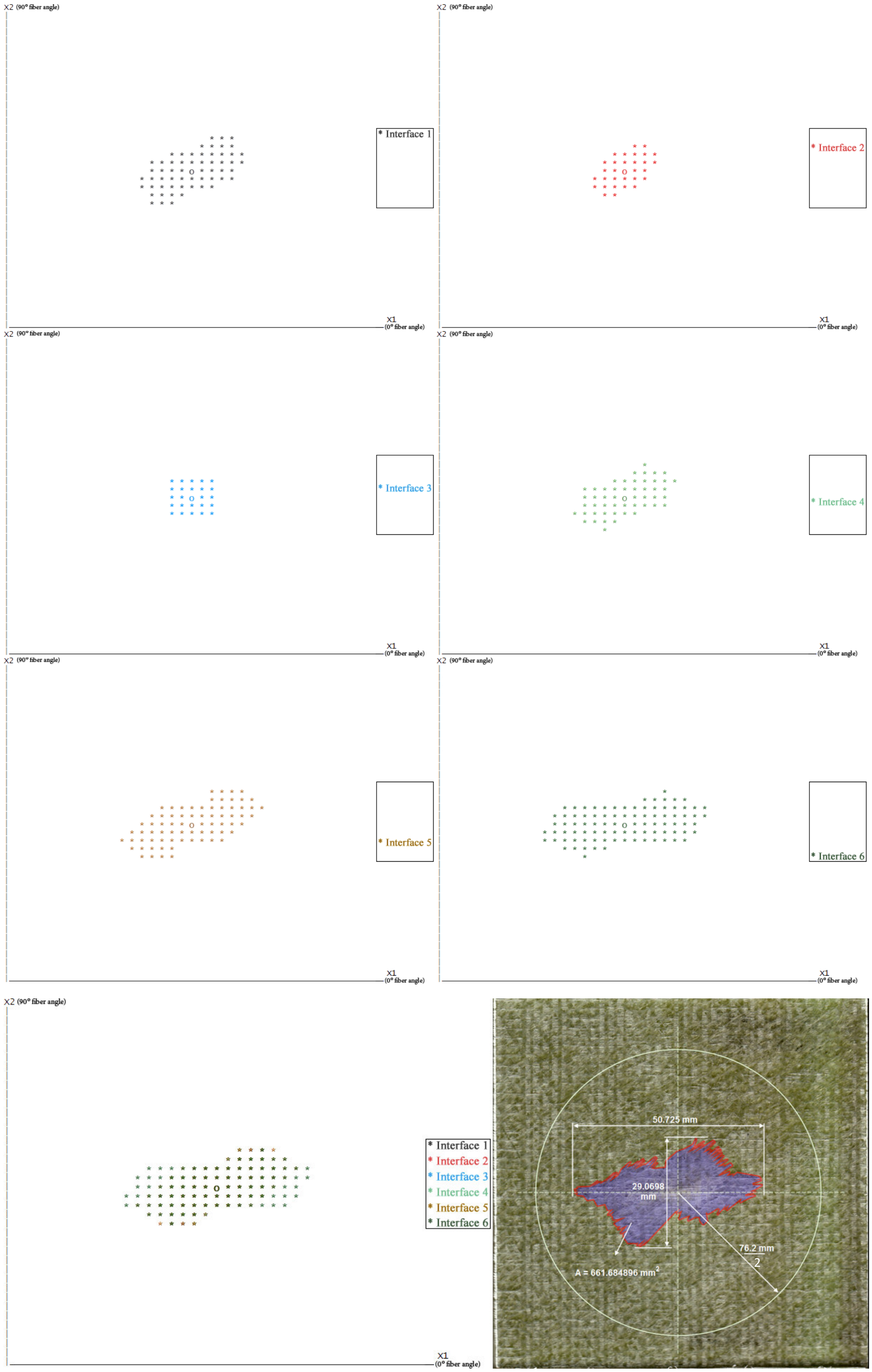

Figure 5.31 Damage illustrations for each and entire interfaces of 20 Joule - 2 m/s specimen.

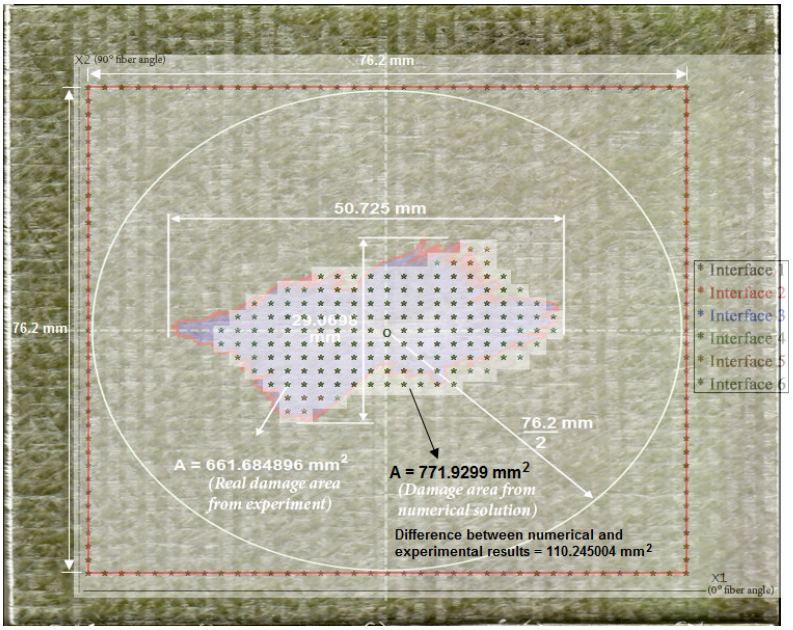

Figure 5.32 Difference between real and numerical delamination area for 20 Joule - 2 m/s specimen.

In Figure 5.31 and 5.33, each interface layer is represented with a color and a transparency level. The transparency level is applied with taking the stacking sequence and the interface layers into account. The overlapped delamination area is generated by overlaying the entire interface layers into each other with blending pixels.

In Figure 5.32 and 5.34, border square in numerical result has been constructed and the clamp circle has been scaled to the fit into this border. After that, the transparency levels have changed to view the difference between numerical and experimental results clearly. In the whole experiments, only the two specimens (20 Joule 5 kg and 10 kg) provide the numerical results. These specimens have the lowest absorbed energy as mentioned before. These specimens have the minimum fiber fractures. This proves the reason of the numerical error that depends on the fiber fracture criterion, again.

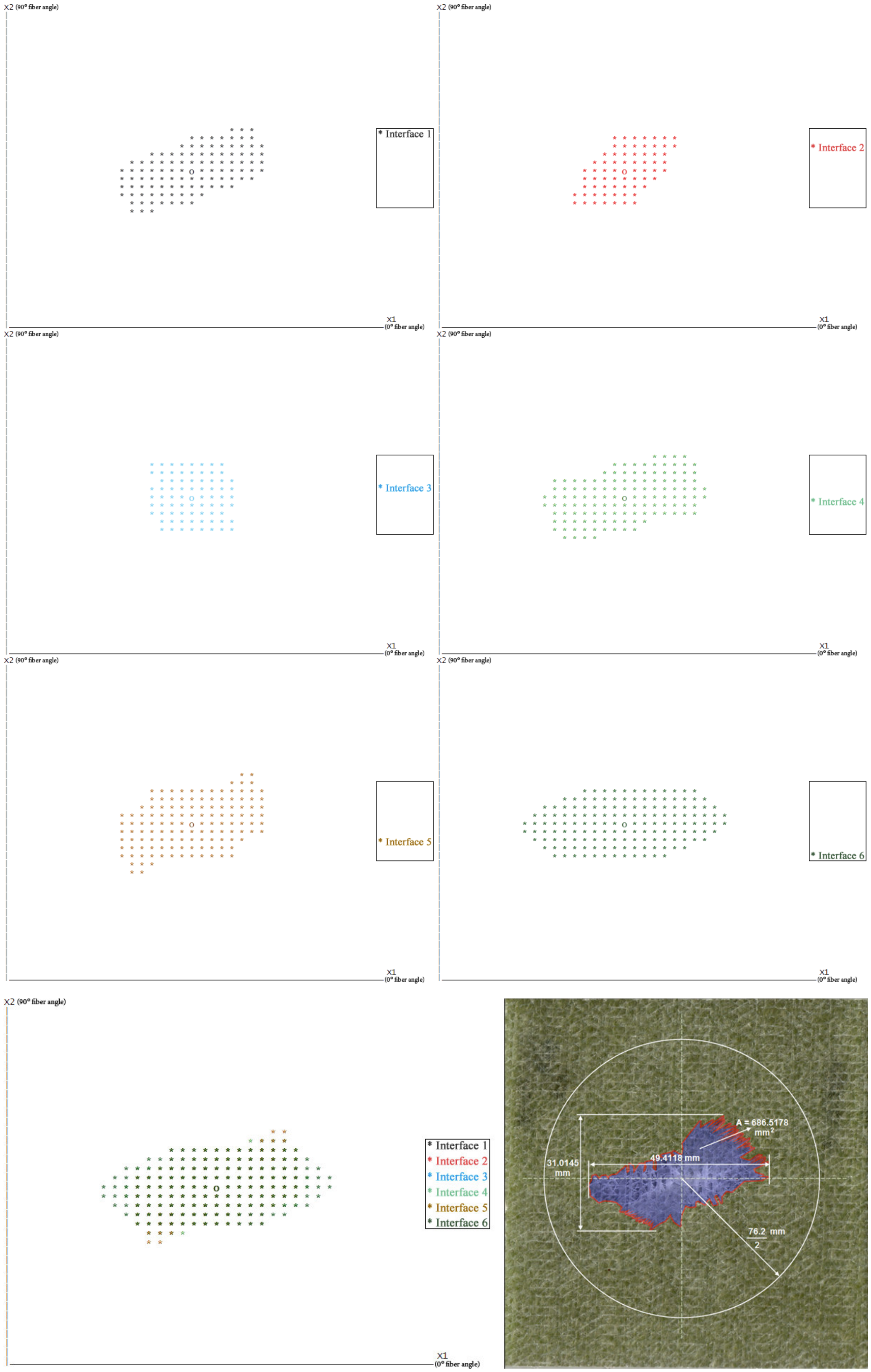

Figure 5.33 Damage illustrations for each and entire interfaces of 20 Joule – 5 Kg specimen.

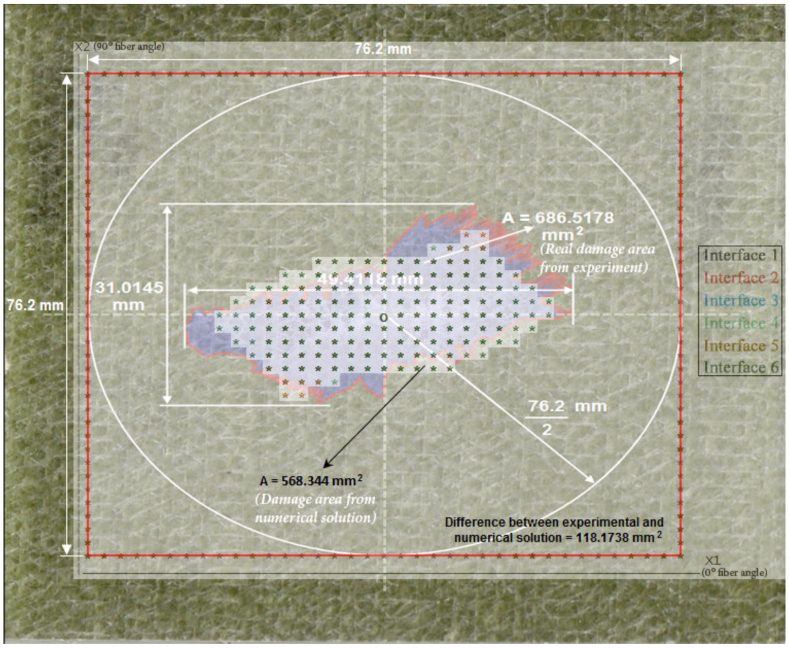

Figure 5.34 Difference between real and numerical delamination areas for 20 Joule – 5 kg specimen.

The difference between experimental and numerical data is maximum at the bottom interface layer that debonding occurs.

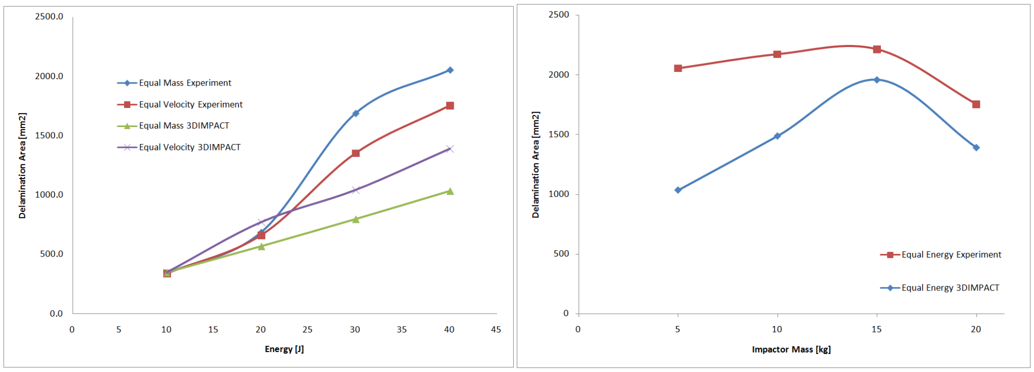

Figure 5.35 Delamination areas for experimental and numerical solutions.

In Figure 5.35 (right), delamination increases with impactor mass at a critical point for equal energy. After this point, delamination become smaller. The main reason for this situation is the fiber fractures. The mass increases the indention for equal impact energy. But for the same condition, increasing the impactor velocity (or decreasing the impactor mass) increases the delaminations.

Table 5.7 Overlapped delamination areas $[mm^2]$ from numerical results for [0°/15°/-15°/90°]s, [0°/30°/60°/90°]s, [0°/30°/-30°/90°]s, [0°/60°/-60°/90°]s, [0°/75°/-75°/90°]s orientation sequences.

		THICKNESS FACTOR = T				THICKNESS FACTOR = 2 T				THICKNESS FACTOR = 3 T			
	Energy → Mass ↓	10 Joule	20 Joule	30 Joule	40 Joule	10 Joule	20 Joule	30 Joule	40 Joule	10 Joule	20 Joule	30 Joule	40 Joule
[0|15|-15|90]s	5 Kg	466.551	793.137	911.895	1331.79	305.379	619.24	1492.96	1921.34	131.483	491.999	822.826	1497.2
	10 Kg	X	644.689	X	1293.62	X	602.275	X	1857.72	X	475.034	X	1378.45
	15 Kg	X	X	907.654	1408.14	X	X	1412.38	1891.65	X	X	653.171	1365.72
	20 Kg	X	X	X	1399.65	X	X	X	1887.41	X	X	X	1365.72
[0|30|60|90]s	5 Kg	347.793	568.344	797.378	1034.9	212.069	610.758	712.551	1645.65	110.276	220.551	483.517	627.723
	10 Kg	X	771.93	X	1488.72	X	534.413	X	1577.79	X	220.551	X	610.758
	15 Kg	X	X	1043.38	1959.51	X	X	661.654	1374.2	X	X	542.896	610.758
	20 Kg	X	X	X	1391.17	X	X	X	1484.48	X	X	X	610.758
[0|30|-30|90]s	5 Kg	500.482	754.964	916.137	1196.07	288.413	466.551	1306.34	1789.86	127.241	458.068	593.792	831.309
	10 Kg	X	678.62	X	1085.79	X	602.275	X	1798.34	X	432.62	X	797.378
	15 Kg	X	X	899.171	1136.69	X	X	1280.89	1705.03	X	X	814.344	788.895
	20 Kg	X	X	X	1170.62	X	X	X	1679.58	X	X	X	924.619
[0|60|-60|90]s	5 Kg	466.551	763.447	967.033	1170.62	203.586	542.896	721.033	924.619	178.138	441.103	687.102	873.723
	10 Kg	X	729.516	X	1102.76	X	534.413	X	941.585	X	407.172	X	856.757
	15 Kg	X	X	1009.45	1119.72	X	X	737.999	907.654	X	X	678.62	831.309
	20 Kg	X	X	X	1136.69	X	X	X	924.619	X	X	X	848.275
[0|75|-75|90]s	5 Kg	466.551	704.068	907.654	1051.86	178.138	237.517	585.31	805.861	152.689	237.517	508.965	678.62
	10 Kg	X	687.102	X	1034.9	X	424.137	X	754.964	X	229.034	X	653.171
	15 Kg	X	X	916.137	1060.34	X	X	585.31	737.999	X	X	500.482	576.827
	20 Kg	X	X	X	1051.86	X	X	X	763.447	X	X	X	602.275

To compare the thickness effect of delamination area for different orientation angles, the overlapped delamination areas are given in Table 5.7. It is clear that, delaminations occur between the interface layer of two adjacent plies due to the angular differences and bending stiffness. With this information, it is easy to say that the maximum differences in angles cause more delamination. But it cannot be clear as well. The investigations show that the positive and negative angles at the same difference in angles have different delamination areas. And the stacking sequence is also effective in delamination and damage areas.

According to the Table 5.7, it is clear that increasing thickness of the laminate decreases delaminations. Increasing the thickness makes the plate stiffer and the bending cracks cannot be occurred as easy as before due to the increment in the bending stiffness.

Overlapped delamination areas are illustrated for the entire orientations (mentioned in Table 5.7) and thicknesses in Figures 5.36-50 to understand the impact damage easier.

Figure 5.36 Damage areas from numerical results for [0°/15°/-15°/90°]s & thicknesses T.

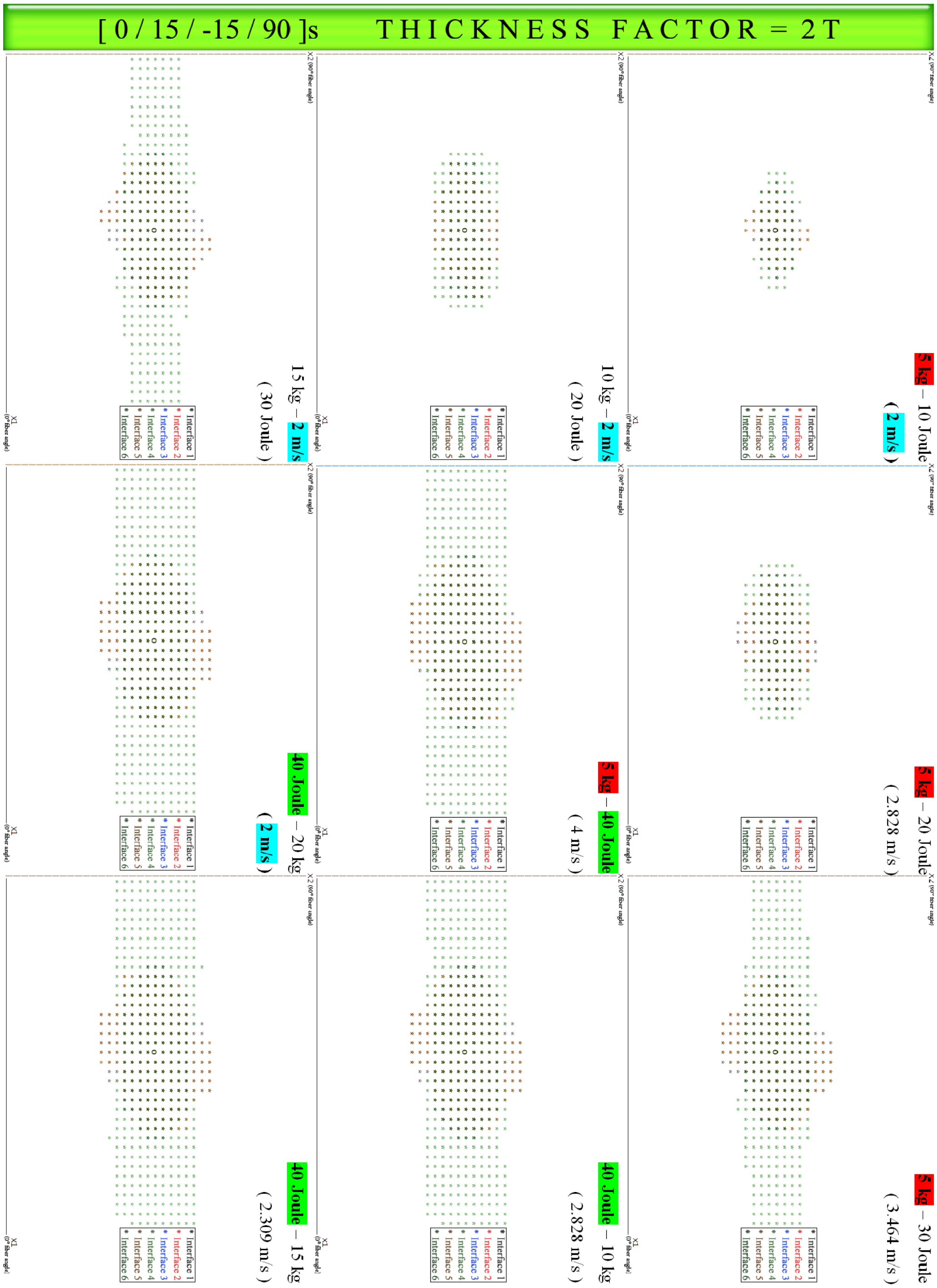

Figure 5.37 Damage areas from numerical results for [0°/15°/-15°/90°]s & thicknesses 2T.

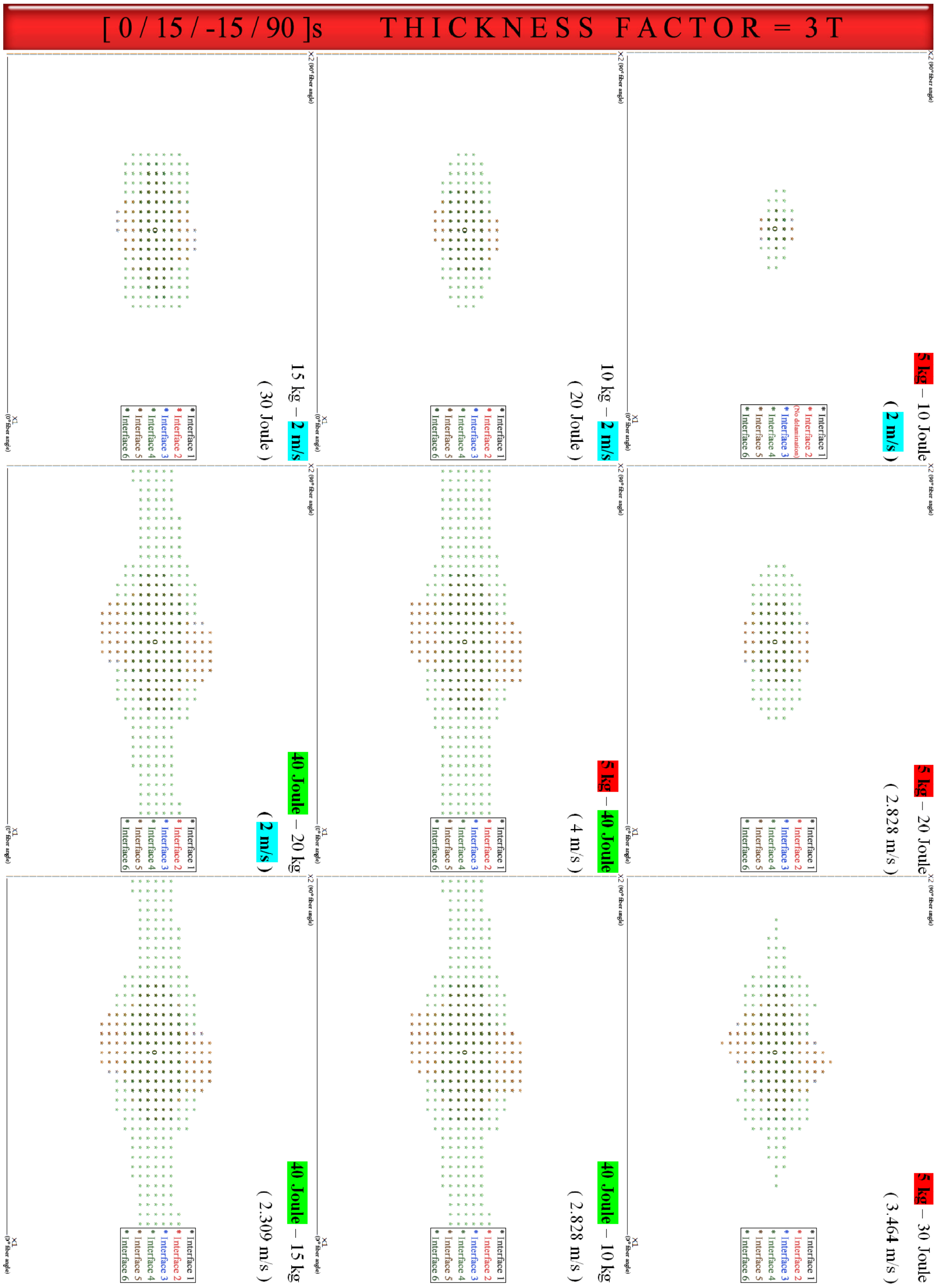

Figure 5.38 Damage areas from numerical results for [0°/15°/-15°/90°]s & thicknesses 3T.

Figure 5.39 Damage areas from numerical results for [0°/30°/60°/90°]s & thicknesses T.

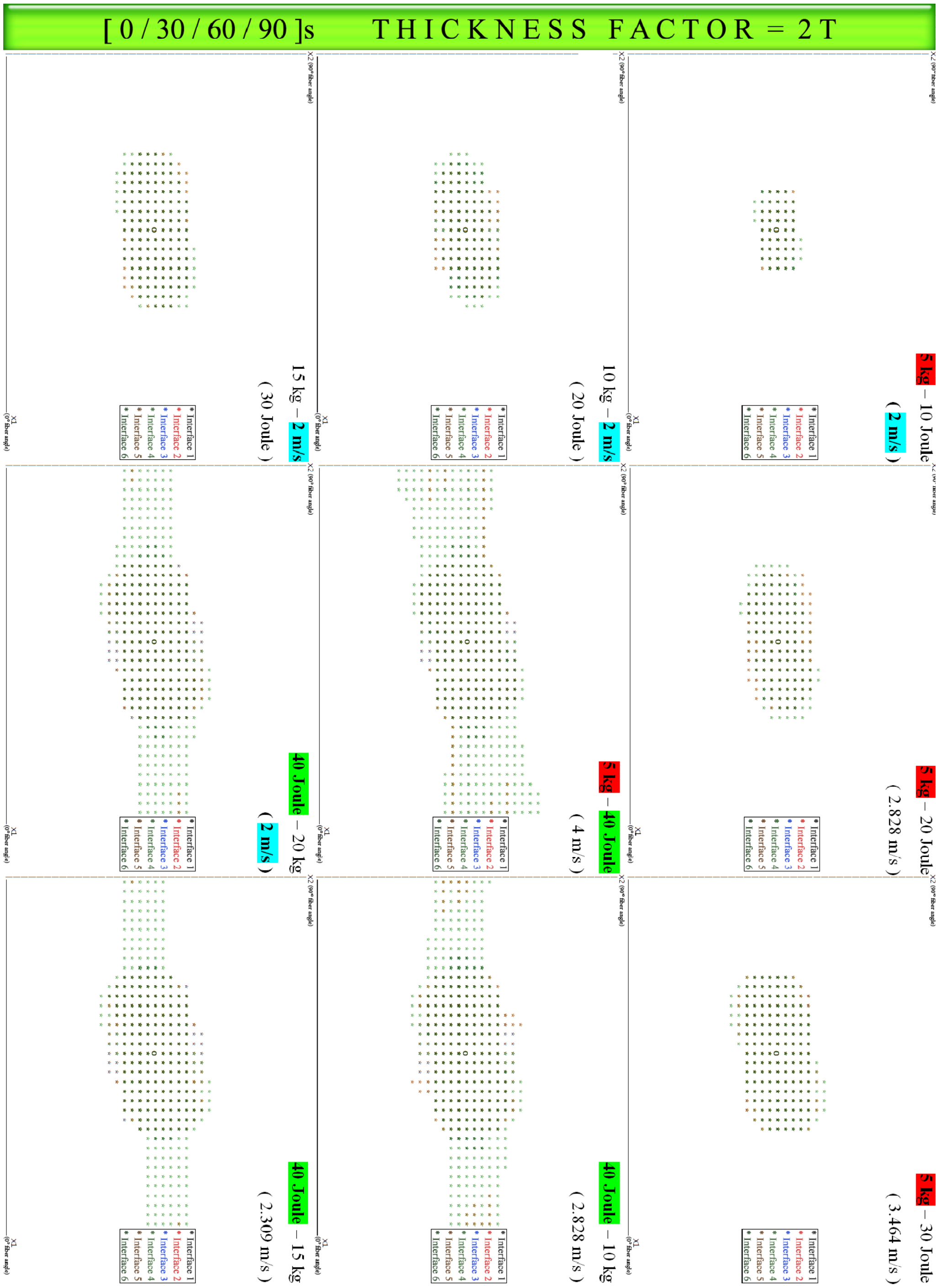

Figure 5.40 Damage areas from numerical results for [0°/30°/60°/90°]s & thicknesses 2T.

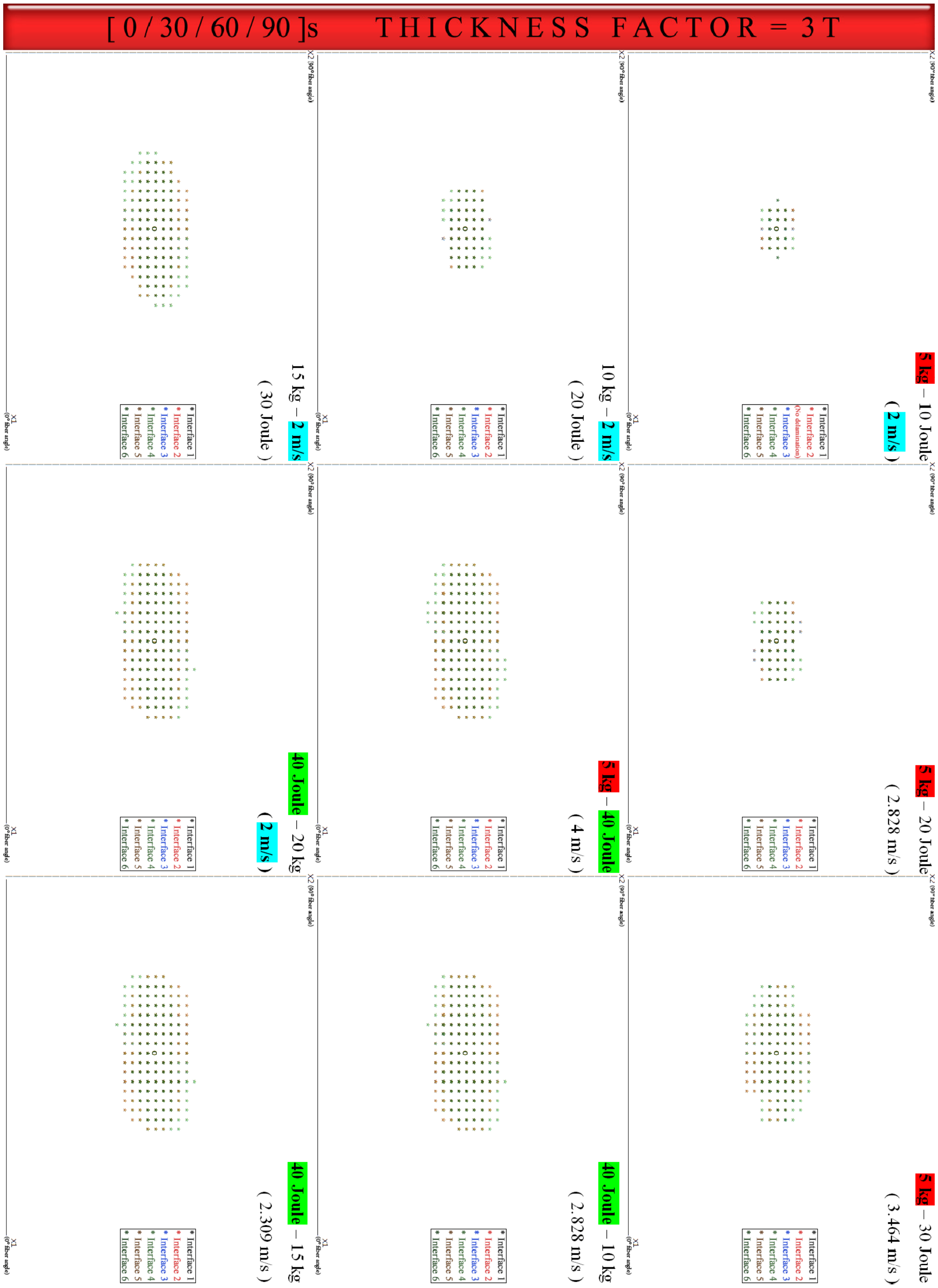

Figure 5.41 Damage areas from numerical results for [0°/30°/60°/90°]s & thicknesses 3T.

Figure 5.42 Damage areas from numerical results for [0°/30°/-30°/90°]s & thicknesses T.

Figure 5.43 Damage areas from numerical results for [0°/30°/-30°/90°]s & thicknesses 2T.

Figure 5.44 Damage areas from numerical results for [0°/30°/-30°/90°]s & thicknesses 3T.

Figure 5.45 Damage areas from numerical results for [0°/60°/-60°/90°]s & thicknesses T.

Figure 5.46 Damage areas from numerical results for [0°/60°/-60°/90°]s & thicknesses 2T.

Figure 5.47 Damage areas from numerical results for [0°/60°/-60°/90°]s & thicknesses 3T.

Figure 5.48 Damage areas from numerical results for [0°/75°/-75°/90°]s & thicknesses T.

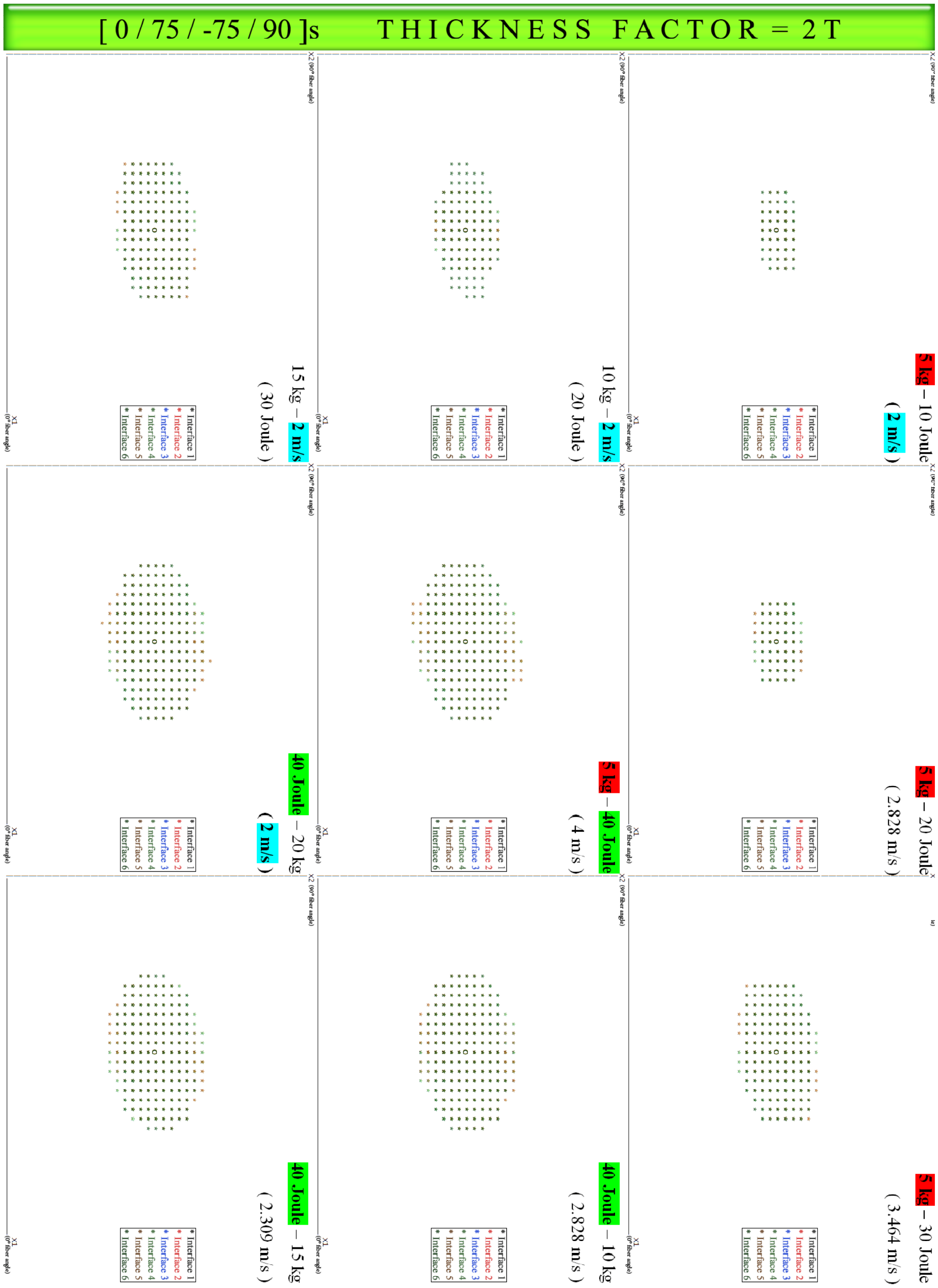

Figure 5.49 Damage areas from numerical results for [0°/75°/-75°/90°]s & thicknesses 2T.

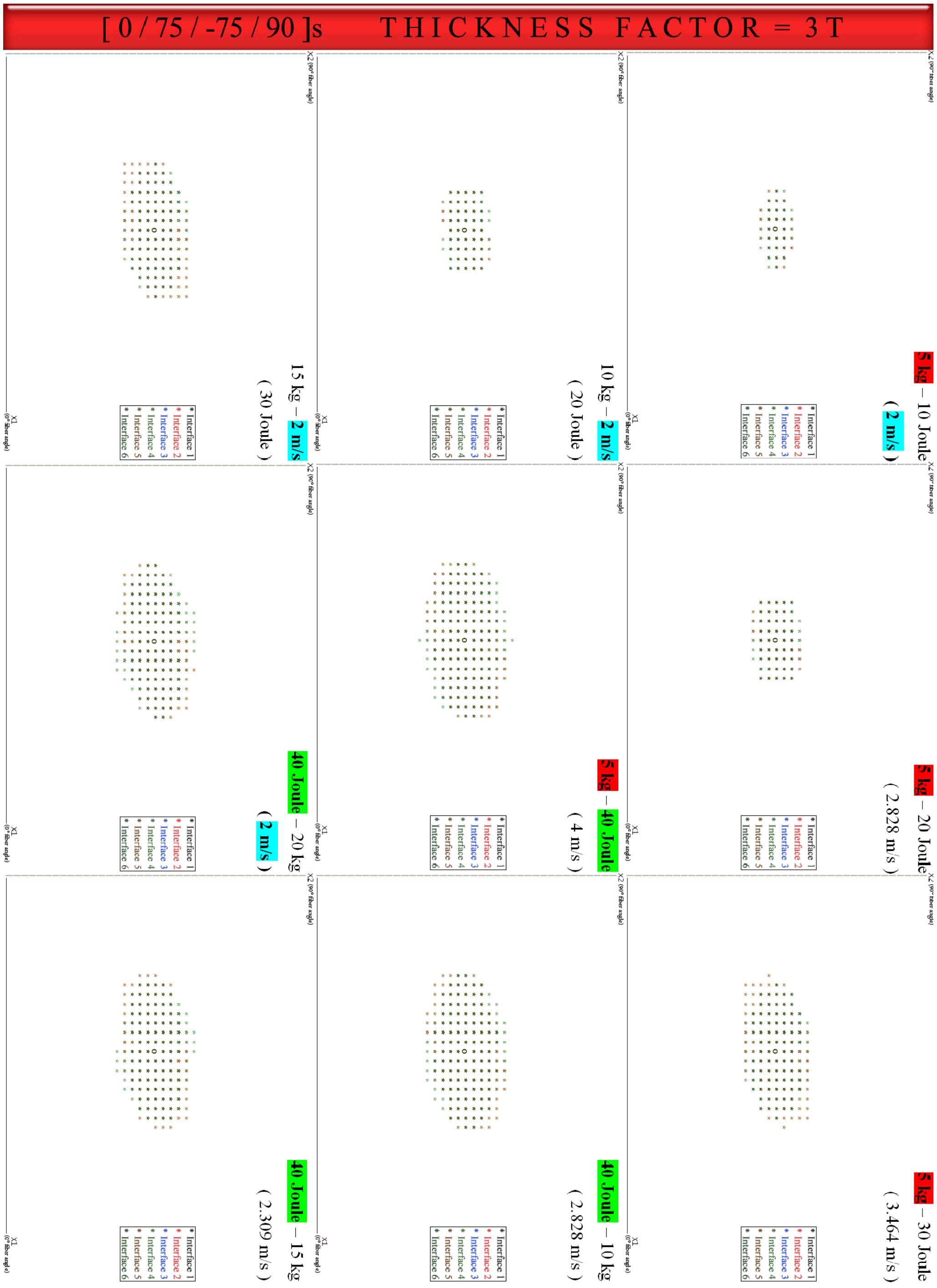

Figure 5.50 Damage areas from numerical results for [0°/75°/-75°/90°]s & thicknesses 3T.

The transparency levels of each interface layer in Figures 5.36-50 are defined precisely to give the most realistic view of damage area as possible as they can. In these figures, the decrease in delaminations from the thickness T to 3T can be seen easily. In these figures, for the thickness of T and impact energy of 40 Joule specimens are highly delaminated. In addition to this, the dimensions for the illustration frame are 76.2 mm x 76.2 mm. For this case, delaminations can be differs from the experimental results due to the boundary conditions.

The change in delamination areas are not in a regular form. It can increase by increasing the difference of the orientation angle or not. In Figure 5.43, debonding can be seen at the bottom layer for [0°/30°/-30°/90°]s with 2T laminate thickness apparently.

CHAPTER SIX

CONCLUSIONS

In this study, the impact behavior of the glass/epoxy laminated composite plates at room temperature is investigated by comparing numerical and experimental results. The following conclusions can be drawn from the results obtained:

- The contact force increases by increasing impact energy. The indention increases by increasing the impactor mass while the delamination area decreases for constant impact energy.
- The impact power obtained from dividing the absorbed energy by contact time is efficient in vibrations through the laminate. The delamination increases by increasing the impact power and the impactor velocity at constant impact energy. And the penetration increases by decreasing the impact power (and decreasing the impactor velocity).
- The maximum contact forces are obtained at [0°/75°/-75°/90°]s orientation for constant impact energy due to the higher bending stiffness.
- The damage at the impacted face is obtained as smaller than the non-impacted face. The main reason for this situation is the tensile cracks due to bending. Also, the delamination area at the non-impacted face is found to be greater because of the same reason that causes debonding.
- The damage area at the impacted face increases by increasing the impactor mass at constant impact energy and at constant impact velocity. The impact energy is not enough to increase the damage area at the impacted face on its own. The damage at the impacted face develops mostly with the impactor mass.
- The lower impactor mass results in delamination and matrix cracks rather than fiber fractures at low energy levels.

- The bottom layer delaminations seem to be greater at all impact energy levels. It results from the bending and fiber fractures. These areas obtained from numerical analysis and experiments are in good agreement.
- The numerical contact forces are greater than the experimental ones. However, the contact time values are different from each other. This leads to the close energy levels absorbed. Hence, the absorbed energy levels are approximately the same.

REFERENCES

Abrate, S. (1999). *Impact on composite structures*. Cambridge: Cambridge University Press.

Aktaş, M. (2007). *Temperature effect on impact behavior of laminated composite plates.* Phd Thesis. Dokuz Eylül University.

Aslan, Z., Karakuzu, R., Okutan, B. (2002). The response of laminated composite plates under low-velocity impact loading. *Journal of Composite Structures, 59,* 119-127.

Brazil, R. (n.d.). *Response to RECP study_tcm18-55861.pdf.* Retrieved February 7, 2008, from, http://www.rsc.org/images/Response%20to%20RECP%20Study_tcm18-5861.pdf

Cesari, F., Re, V. D., Minak, G., Zucchelli, A. (2006). Damage and residual strength of laminated carbon-epoxy composite circular plates loaded at the centre. *Journal of Composites: Part A, 38,* 1163-1173.

Chung, D. D. L. (1994). *Carbon fiber composites.* NY: Butterworth-Heinemann.

Composite material – Wikipedia, the free encyclopedia (n.d.). Retrieved February 7, 2008, from http://en.wikipedia.org/wiki/Composite_material

Coutellier, D., Walrick, J. C., Geoffroy, P. (2005). Presentation of a methodology for delamination detection within laminated structures. *Journal of Composites Science and Technology, 66,* 837-845.

Daniel, I. M., Ishai, O. (1994). *Engineering mechanics of composite materials.* Oxford: Oxford University Press.

Elder, D. J., Thomson, R. S., Nguyen, M. Q., Scott, M. L. (2004). Review of delamination predictive methods for low speed impact of composite laminates. *Journal of Composite Structures, 66,* 677-683.

Glossary – Fiberglass Warehouse. (n.d.). Retrieved February 7, 2008, from http://www.fiberglasswarehouse.com/glossary2.asp

Guinard, S., Allix, O., Guédra-Degeorges, D., Vinet, A. (2000). A 3D damage analysis of low-velocity impacts on laminated composites. *Journal of Composites Science and Technology, 62,* 585-589.

Jones, R.M. (1999). *Mechanics of composite materials* (2nd ed.). NY: Taylor & Francis.

Kaw, A.K. (2006). *Mechanics of composite materials* (2nd ed.). NY: Taylor & Francis.

Liu, D., Raju, B. B., Dang, X. (2000). Impact perforation resistance of laminated and assembled composite plates. *International Journal of Impact Engineering, 24,* 733-746.

Mallick, P.K. (2007). *Fiber re-inforced composites Materials, manufacturing, and design* (3rd ed.). NY: CRC Press.

Mazumdar, S. K. (2002). *Composites manufacturing, Materials, product, and process engineering.* NY: CRC Press.

Miracle, D.B., Donaldson, S.L. (2001), *ASM handbook volume 21 composites*, NY: ASM International.

Morozov, E. V., Sylantiev, S. A., Evseev, E. G. (2003). Impact damage tolerance of laminated composite helicopter blades. *Journal of Composite Structures, 62,* 367-371.

Peters, S. T. (ed.). (1998). *Handbook of composites* (2nd ed.), NY: Chapman & Hall.

Staab, G. H. (1999). *Laminar composites.* NY: Butterworth-Heinemann

Takeda, S., Minakuchi, S., Okabe, Y., Takeda, N. (2004). Delamination monitoring of laminated composites subjected to low-velocity impact using small-diameter FBG sensors. *Journal of Composites Part A: applied science and manufacturing, 36,* 903-908.

Tita, V., Carvalho, J., Vandepitte, D. (2007). Failure analysis of low velocity impact on thin composite laminates: Experimental and numerical approaches. *Journal of Composite Structures, 83,* 413-428.

Vasiliev, V.V., Morozov, E.V. (2007). *Advanced mechanics of composite materials* (2nd ed.). NY: Elsevier.

WordNet Search - 3.0 (n.d.). Retrieved February 7, 2008, from, http://wordnet.princeton.edu/perl/webwn?s=composite%20material

Zhang, Y., Zhu, P., Lai, X. (2004). Failure analysis of low velocity impact on thin composite laminates: Experimental and numerical approaches. *Journal of Materials and Design, 27,* 513-519.

Zheng, D., Binienda, W. K. (2007). Effect of permanent indention on the delamination threshold for small mass impact on plates. *International Journal of Solids and Structures, 44,* 8143-8158.